ORNL/SR-2017/291

FY 2017 Status Report: CIRFT Data Update and Data Analyses for Spent Nuclear Fuel Vibration Reliability Study

Fuel Cycle Research & Development

Prepared for
US Department of Energy
Used Fuel Disposition Campaign

J.-A. Wang, H. Wang
B. B. Bevard, J. M. Scaglione
Oak Ridge National Laboratory

August 8, 2017
M3SF-17OR010201026
SFWD-SFWST-2017-000030

ORNL/SR-2017/291

Materials Science and Technology Division

FY 2017 Status Report: CIRFT Data Update and Data Analyses for Spent Nuclear Fuel Vibration Reliability Study

Jy-An John Wang, Hong Wang

Program Manager
Bruce Bevard and John Scaglione

Date Published: August 8, 2017

Prepared by
OAK RIDGE NATIONAL LABORATORY
Oak Ridge, TN 37831-6283
managed by
UT-BATTELLE, LLC
for the
US DEPARTMENT OF ENERGY
under contract DE-AC05-00OR22725

This page intentionally left blank.

SUMMARY

The objective of this research is to collect experimental data on spent nuclear fuel (SNF) from pressurized water reactors (PWRs), including the H. B. Robinson Nuclear Power Station (HBR), Catawba Nuclear Station, North Anna Nuclear Power Station (NA), and the Limerick Nuclear Power Station (LMK) boiling water reactor (BWR). Data will be collected under simulated transportation environments using the cyclic integrated reversible-bending fatigue tester (CIRFT), an enabling hot-cell testing technology developed at Oak Ridge National Laboratory (ORNL). These data will be used to support ongoing SNF modeling activities and to address regulatory issues associated with SNF transport.

The first portion of this report provides an overall update on the static and dynamic test data developed by utilizing CIRFT. These data are used to evaluate the vibration integrity of SNF under normal conditions of transport (NCT). The CIRFT consists of a U-frame test setup, and it uses a real-time curvature measurement method. The three-component U-frame setup of the CIRFT has two rigid arms and linkages connecting to a universal testing machine. The curvature SNF rod bending is obtained through a three-point deflection measurement method. Three linear variable differential transformers (LVDTs) are clamped to the side connecting plates of the U-frame and used to capture deformation of the rod.

The LVDTs' sensor spacing correction is based on the developed equivalent gauge length that was used as a correction factor and implemented into this update. In addition to this correction, the LVDTs' stem dynamic correction factor was also developed and implemented into this most recent CIRFT dynamic test data update.

The correction factors based on the equivalent gauge length methodology and the LVDTs' stem vibration stability have been successfully used in CIRFT data analysis for static and dynamic tests conducted on LMK (18 tests), NA (7 tests), Catawba Nuclear Station mixed oxide (MOX) SNF samples (25 tests), and HBR (30 tests). The data sets obtained from static measurements and dynamic online monitoring were processed and analyzed, and the fatigue life of the rods was characterized in terms of moment, curvature, and equivalent stress and strain.

The second portion of this report provides the details of analyses procedures for using CIRFT test data for SNF fatigue life prediction. The modified equivalent stress-strain approach (MESA) was also developed in FY2017 to effectively translate the global CIRFT moment-curvature data into the local cladding surface stress-strain profile. This new approach was implemented into both CIRFT static test data and CIRFT dynamic test data in the FY2017.

The variations in fatigue life are provided in terms of moment, equivalent stress, curvature, and equivalent strain for the tested SNF. The equivalent stress or strain plots collapsed the data points from all the SNF samples into a single zone. A detailed examination revealed that at the same stress level, fatigue lives display a descending order, as follows: LMK, HBR, and MOX. A discontinuity or knee point for the endurance limit in the curve of moment and curvature or equivalent quantities is more clearly defined for LMK and HBR fuels.

To estimate the potential damage to SNF system vibration lifetime caused by transient shocks resulting from component contact interaction, drop impact tests were performed on the CIRFT specimen prior to the CIRFT harmonic vibration fatigue testing. The combined 12-inch drop-impact and CIRFT cyclic harmonic vibration test results show significant reduction in fatigue life.

There are two types of vibration loading modes involved in SNF transport under NCT: harmonic vibration modes and periodic transient shocks. These shocks include SNF system components' contact interactions. The associated damage mechanisms are described below.

1) In a harmonic vibration loading mode:

   - Due to maximum axial tensile stress occurring on the outer cladding wall, crack growth is likely initiated at the outer clad wall under loading.
   - Due to circumferential hydride rim reinforcement near the outer cladding wall, no obvious crack growth was observed from as-irradiated CIRFT test post irradiation examination (PIE) data.
   - The high burnup (HBU) SNF failure under harmonic vibration appears to result from spontaneous brittle fracture mode.

2) In an SNF component's contact interactions or periodic transient shocks loading mode:

   - Due to maximum axial/hoop tensile stress occurring at the cladding's inner wall, the crack growth is likely initiated at the cladding's inner wall region, and then it propagates toward the cladding's outer wall under cyclic fatigue loading.
   - The crack growth phenomenon was further confirmed by the severe reduction in flexural rigidity observed in CIRFT real-time monitoring data.

Therefore, under NCT, two failure damage mechanisms are involved in the SNF vibration stability investigation: *harmonic vibration mode* and *transient shock mode*. Apparently, the crack growth initiated at the cladding's inner wall has a much higher damage potential. With one drop from 12 inches (contact load intensity similar to that of a 20 g transient shock at the spacer grid region), a 75% fatigue life reduction was observed from CIRFT test results. Thus, based on the potential for repeated contact transient shocks, the potential for associated reduced fatigue life deserves special attention and should be included in the accumulated damage (AD) evaluation of SNF transported under NCT.

ACKNOWLEDGMENTS

This research was sponsored by the US Department of Energy (DOE) Used Fuel Disposition Campaign under DOE contract DE-AC05-00OR22725 with UT-Battelle, LLC. The authors thank ORNL program managers Bruce Bevard and John Scaglione for their support and guidance during the project, Chuck Baldwin for post-irradiation examination, Yong Yan for preparation hydride reorientation samples, Dale Caquelin and Bob Morris for logistic support, Josh Schmidlin for fuel rod cutting and dimension measurement, Bryan Woody and Scott Thurman for hot cell operation support, Brian Sparks and Randy Parten for drawing and machining support, and Lianshan Lin and Rose Raney for reviewing the report.

This page intentionally left blank.

CONTENTS

This page intentionally left blank.

LIST OF FIGURES

This page intentionally left blank.

LIST OF TABLES

This page intentionally left blank.

ACRONYMS

AD	accumulated damage
BE	bonding efficiency
BWR	boiling water reactor
CIRFT	cyclic integrated reversible-bending fatigue tester
DOE	US Department of Energy
EI	flexural rigidity
EPRI	Electric Power Research Institute
FEA	finite element analysis
FEM	finite element method
FFT	Fast Fourier Series Transformation
FY	fiscal year
HBR	H. B. Robinson Nuclear Power Station
HBU	high-burnup
HR	hydride reorientation
ID	inner diameter
LMK	Limerick Nuclear Power Station
LVDT	linear variable differential transformer
MESA	modified equivalent stress-strain approach
MOX	Catawba mixed uranium-plutonium oxide
NA	North Anna Power Station
NCT	normal conditions of transport
NRC	US Nuclear Regulatory Commission
NUREG	Nuclear Regulatory Commission technical report
NUREG/CR	NUREG contractor report
OD	outer diameter
ORNL	Oak Ridge National Laboratory
PIE	post-irradiation examination
PNNL	Pacific Northwest National Laboratory
PPI	pellet-to-pellet interface
PWR	pressurized water reactor
RHT	radial hydride treatment
SNF	spent nuclear fuel
SS	stainless steel

UFDC	Used Fuel Disposition Campaign

This page intentionally left blank.

USED FUEL DISPOSITION CAMPAIGN

FY 2017 Status Report: CIRFT Data Update and Data Analyses for Spent Nuclear Fuel Vibration Reliability Study

1. INTRODUCTION

The objective of this research is to collect experimental data on spent nuclear fuel (SNF) from pressurized water reactors (PWRs)—including the H. B. Robinson Nuclear Power Station (HBR), Catawba Nuclear Station, and North Anna Power Station (NA), and the Limerick Nuclear Power Station (LMK) boiling water reactor (BWR)—under simulated transportation environments using the cyclic integrated reversible-bending fatigue tester (CIRFT) [1–5], an enabling hot-cell testing technology developed at Oak Ridge National Laboratory (ORNL). These data will be used to support ongoing SNF modeling activities and to address regulatory issues associated with SNF transport.

Testing of SNF rods from PWRs, including HBR Zircaloy-4 cladding, NA, and Catawba M5 cladding [6–8], demonstrated that the cyclic fatigue lifetime of SNF rods generally depends on the amplitude of the applied moment when a 5 Hz waveform is used. It was also demonstrated that the lifetime of SNF is related to the degree of damage to cladding and fuel pellets resulting from irradiation after long-term service inside a reactor. SNF lifetime is also affected by the loading amplitude and loading rate of the applied moment caused by different fatigue damage mechanisms triggered by the intensity of pellet-cladding mechanical interaction. Detailed high-burnup (HBU) HBR CIRFT results are published in US Nuclear Regulatory Commission (NRC) technical report (NUREG)/CR-7198 [9]. The CIRFT program also extended the vibration data collected to include Zircaloy-2 data from a BWR environment [10]. A stress-failure frequency (S-N) trend similar to the PWR data was also observed in the BWR data. Furthermore, the accumulated damage (AD) from the combination of low-amplitude CIRFT cyclic bending plus transient shocks (high-amplitude bending load) indicates an accelerated aging effect compared with low-amplitude cyclic loading alone.

CIRFT enables examination of the underlying mechanisms of the SNF system's dynamic performance. Major findings from CIRFT evaluations on HBU SNF include:

- SNF system interface bonding plays an important role in SNF vibration performance.
- Fuel structure contributes to the SNF system's stiffness.
- There are significant variations in the stress and curvature of SNF systems during vibration cycles which result from the interaction of pellets and cladding.
- SNF failure initiates at the pellet-pellet interface (PPI) region and appears to be spontaneous.

Due to the inhomogeneous composite structure of the SNF system, finite element analysis (FEA) was needed to translate the global moment-curvature measurement into local stress-strain profiles for further investigation. Furthermore, the detailed mechanisms of the pellet-pellet and pellet-cladding interactions and the stress concentration effects at the PPI cannot be readily obtained from a CIRFT system measurement. Therefore, detailed FEA is necessary to further understand the global test response.

The theoretical basis to improve CIRFT curvature measurements was developed in fiscal year (FY) 2016, including the associated verification testing protocols needed to validate this approach. The effort was extended to cover all the dynamic CIRFT data sponsored by the US Department of Energy (DOE) excluding HBR data sponsored by the NRC [9]. The FEA protocols developed for this activity provide powerful tools to quantify the CIRFT system biases and the associated uncertainties of HBU SNF during CIRFT examinations. In FY 2016, efforts were also extended to loading intensity investigations and

evaluation with real time SNF vibration under normal condition of transport (NCT). These efforts served as additional benchmarks for quantifying and justifying the CIRFT test loading intensity ranges.

In FY 2017, the update curvature measurement procedure was also extended to all the static CIRFT tested data; the updated dynamic correction factor that considers the linear variable differential transformers' (LVDTs) stem vibration stability was also implemented into all the dynamic CIRFT test data. Furthermore, the curvature measurements of both the static and dynamic CIRFT test data for HBU HBR rods, sponsored by NRC, were also updated.

The modified equivalent stress-strain approach (MESA) was also successfully developed in FY 2017 to effectively translate the global CIRFT moment-curvature trend into local cladding surface stress-strain data. This new approach will be implemented into both static and dynamic CIRFT tests in the next report period.

1.1 Cyclic Integrated Reversible-Bending Fatigue Tester

The CIRFT, which was developed by ORNL [1–5, 10–14], consists of a U-frame (Figure 1)with two rigid arms, connecting plates, and universal testing machine links. A rod specimen is coupled to the arms with two specially designed grips. The U-frame is oriented in a horizontal plane and is driven by Bose dual linear motors that are based on electromagnetic force. With assistance from the coupling, linear motions applied at the loading points of the rigid arms are converted into bending moments. The dual linear motor (model LM2) test bench has a maximum load capacity of ±3,000 N and a maximum stroke of ±25.6 mm. Bending is imposed through the U-frame's dual driving points and a 101.60 mm loading arm. Under a pair of outward-facing forces or displacements, the rigid arms are opened, and bending moments force the rod to deflect away from the operator. The rigid arms are closed by a pair of facing forces, forcing the rod to deflect inward. The CIRFT can deliver dynamic loading to a rod specimen in the load-control mode at 5–10 Hz. The current configuration enables the system to test a rod 9.70–11.74 mm in diameter, 152.40 mm (6 in.) in length, and 50.80 mm (2 in.) in gauge section. Three LVDTs measure rod deflections at three adjacent points within the gauge section to determine rod curvature, which is then correlated to the applied moment to characterize the mechanical properties of the bending rod. Online monitoring captures the mechanical property changes during testing, revealing fatigue behavior.

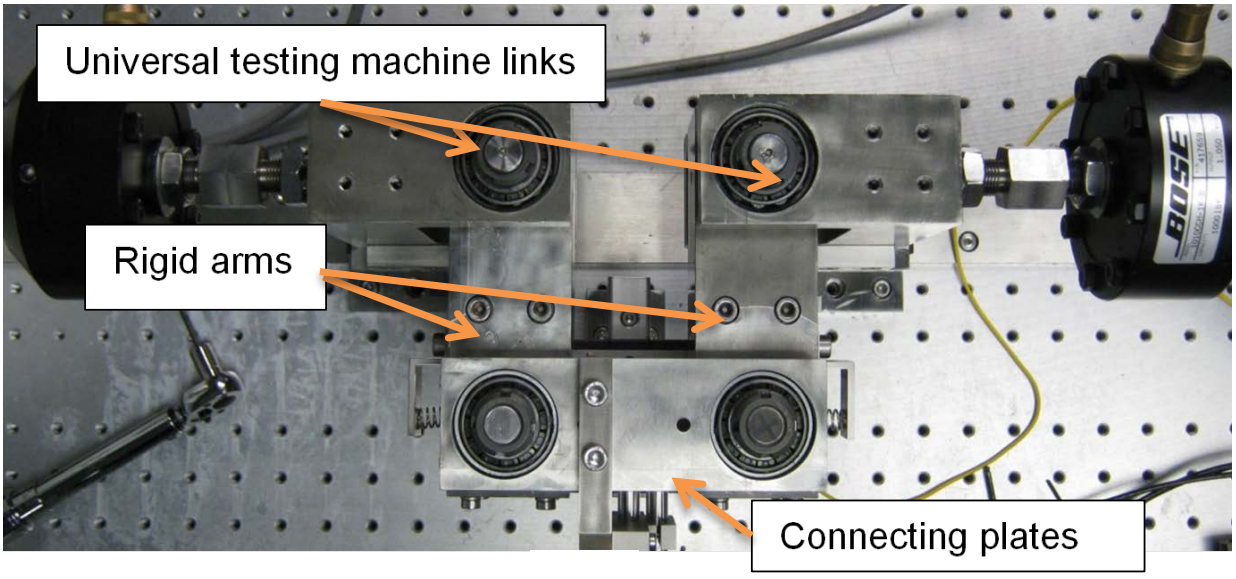

(a)

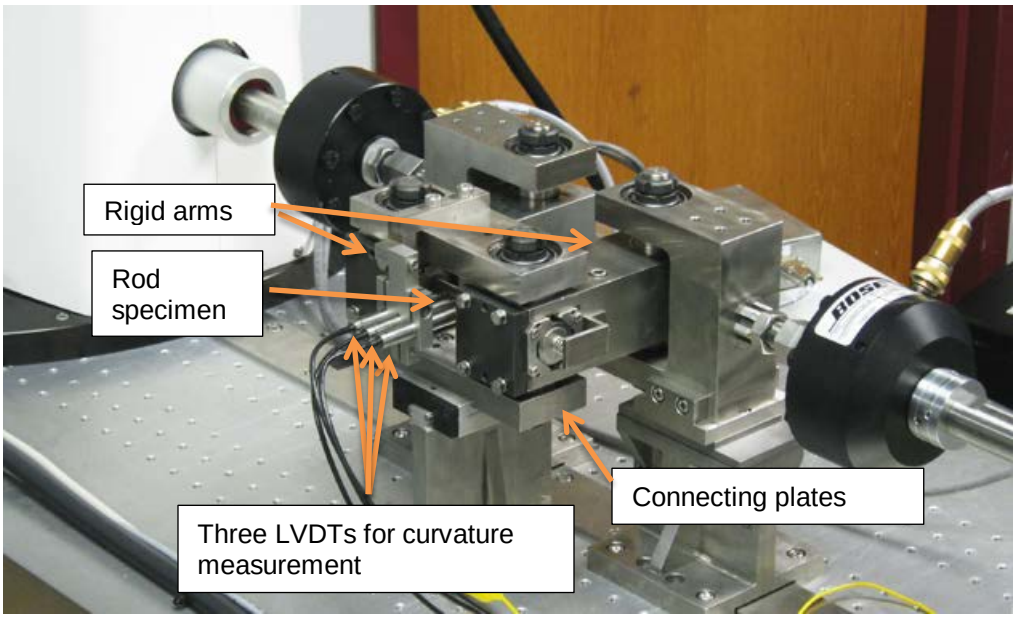

(b)

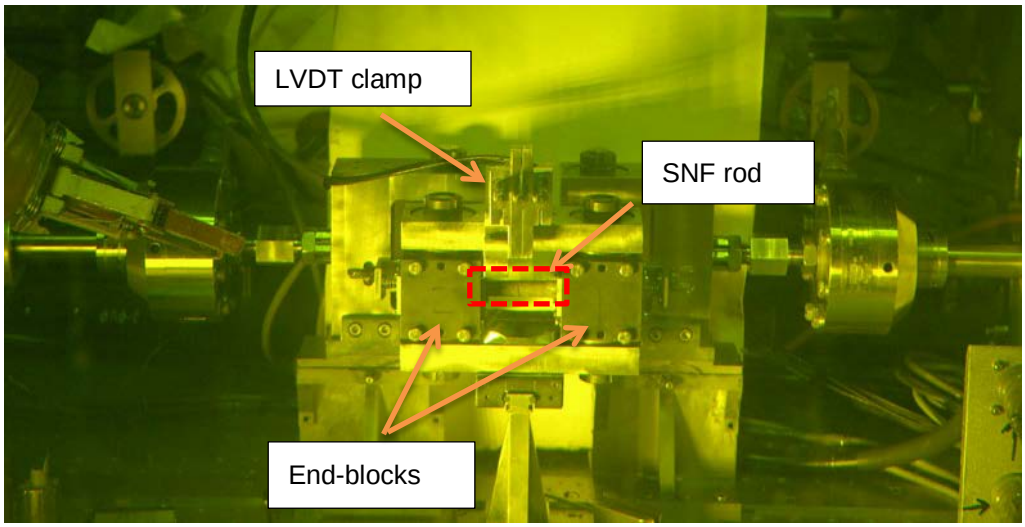

(c)

Figure 1. Three views of the ORNL CIRFT: (a) Horizontal layout of the U-frame setup, (b) a rod specimen undergoing testing with three LVDTs in place for curvature measurements (the operator is facing the LVDTs), and (c) a front view of the CIRFT installed in a hot cell.

1.2 Moment and Curvature Calculations

Measurement data are converted into the applied moment and curvature based on the load channel (load1 and load2) information, the loading arm length (101.60 mm), and LVDT data (LVDT1, 2, and 3).

The moment was estimated by

$$M = F \times L, \tag{1}$$

where F is the averaged value of applied loads (load1 and load2) from the Bose dual motors, and L is the loading arm length, 101.60 mm.

Theoretically, the bending radius and maximum strain of a rod can be estimated based on the traveling displacement at the loading points of the rigid arm. However, the measured displacement contains the contribution of the compliant layers and the level of loading.

To address this issue, direct measurements were made of specimen displacement at three adjacent points along the rod [15] to evaluate the curvature of a bending rod in this study [1,11].

Given any curve C and a point P on the curve, there is a unique circle or line that most closely approximates the curve near P, the osculating circle at P. The curvature of C at P is then defined as the curvature of that circle or line. The radius of the curvature is defined as the reciprocal of the curvature. Given the deflections from three LVDTs—d_1, d_2, and d_3 (Figure 2)—the curvature κ of the bending rod was determined using the following equation:

$$\kappa = [(x_0 - d_2)^2 + y_0^2]^{-1/2}, \tag{2}$$

where

$$x_0 = \frac{-2m_a m_b h - m_a(d_2 + d_3) + m_b(d_1 + d_2)}{2(m_b - m_a)},$$

$$y_0 = -\frac{1}{m_a}\left(x_0 - \frac{d_1 + d_2}{2}\right) - \frac{h}{2},$$

and

$$m_a = \frac{h}{d_2 - d_1},$$

$$m_b = \frac{h}{d_3 - d_2}.$$

The sensor distance is h (12 mm).

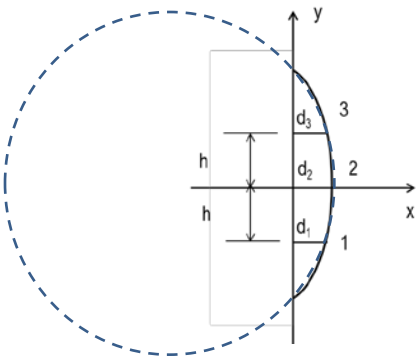

Figure 2. Determination of the bending curvature of the rod based on deflections measured at three points.

The arrangement of the three LVDTs and their position in the setup can be seen in Figure 3. An equivalent strain-stress curve as given in Eq. (3) can be obtained by assuming that the SNF rod can be idealized as a linear, elastic, homogeneous material without considering the effects of pellet-cladding interaction. The equivalent stress was calculated using

$$\sigma = M \times y_{max}/I, \tag{3}$$

and, the equivalent strain is determined using

$$\varepsilon = \kappa \times y_{max}, \tag{4}$$

where I is the moment of inertia of the composite SNF rod, and y_{max} is the maximum distance to the neutral axis of the test rod for the section and is measured by the radius of the cladding.

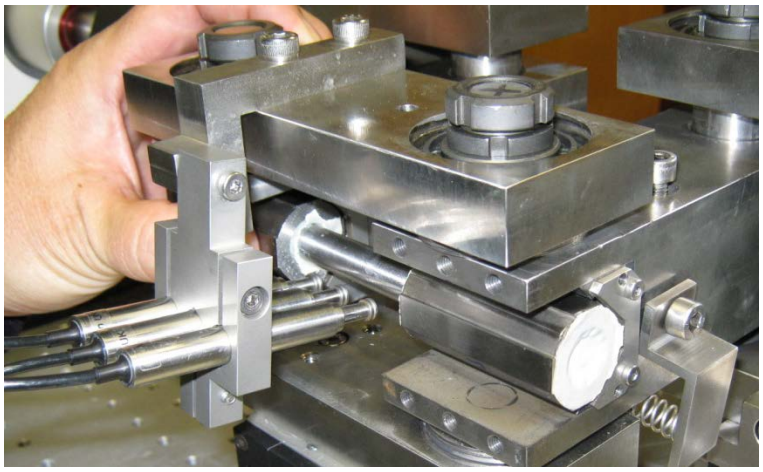

Figure 3. Grip design of CIRFT with one end-block removed.

M-κ, a first order approximation approach commonly used for an isotropic/homogeneous structure, was adopted to translate the global CIRFT M-κ data into an equivalent stress and strain of the cladding. For this approximation, the SNF rod's moment of inertia is written as

$$I = I_c + c \times I_p, \tag{5}$$

where I_c and I_p are moments of inertia of cladding and pellet, respectively, and $c = E_p/E_c$. (Because the baseline Young's modulus of the oxide fuel is twice that of the cladding, c is likely greater than 1.) In the proposed equivalent stress and strain approach, c is set to 1, which implies a 50% reduction in the pellet Young's modulus to account for operationally induced degradation of the HBU fuel pellet. This hypothesis of 50% reduction in fuel flexural rigidity was also validated and demonstrated in Jiang et al. [16]. The moment range (ΔM), curvature range ($\Delta\kappa$), and flexural rigidity EI are used to characterize the mechanical response of the fuel rod. These are defined as:

$$\begin{gathered}\Delta M = M_{max} - M_{min,} \\ \Delta\kappa = \kappa_{max} - \kappa_{min,} \text{ and} \\ EI = \Delta M / \Delta\kappa,\end{gathered} \tag{6}$$

where the subscripts *max* and *min* represent the maximum and minimum oscillation height (see Sect. 1.4.4 for more information on the flexural rigidity calculation).

These parameters were derived from the CIRFT data and test specimens and are used to examine the SNF rod fatigue performance and investigate phenomena of interest.

Two items of interest are discussed within the context of the data obtained through CIRFT testing: (1) the role of the pellet in nucleating fatigue failures (termed *pellet-cladding interaction* within this document) and (2) the extension or reduction of the fatigue lifetime resulting from mechanical[1] or chemical[2] bonding between the pellet and cladding or pellet and pellet (termed *bonding* in this document). The effects of a stress concentration at locations of pellet-cladding interaction relative to the gauge strain at pellet-to-pellet interfaces (PPIs) on the global flexural rigidity and the local plastic deformation were studied using the finite element method (FEM) [16]. The implication of the FEM numerical results on the interpretation of bending testing is discussed. It is noted that the instrumentation used on the CIRFT device measured the global rod deformation within the gauge section, or the gauge strain that covers several pellet lengths with several PPIs. The localized strain at the PPIs cannot be precisely known for these experiments, but it will be greater than the gauge strain measured in the tests.

1.3 Sensor Spacing Correction for Curvature Measurements

The contact of the LVDT probe with the rod being tested depends on the bending direction and induced curvature, especially when contact is made by a disk with a flat head. This contact caused the sensor spacing to deviate from the ideal condition (Figure 4).

For a positive curvature, when the tensile load was applied to the U-frame, actual sensor spacing h_2 is,

$$h_2 = h + \Delta h, \tag{7}$$

and for negative curvature, when the compressive load was applied to the U-frame, actual sensor spacing h_1 is

$$h_1 = h - \Delta h \tag{8}$$

[1] During reactor operation, pellet swelling and cladding creep down result in a mechanical interference fit between cladding and pellet that produces a mechanical bond through clad radial compressive residual stress. The mechanical bond is likely maintained throughout the fuel's dry storage and transport lifetime and is likely providing enhanced rod rigidity to SNF rod.

[2] There is evidence that a chemical bond between the zirconium-based fuel rod cladding and the uranium dioxide pellets can be developed at HBU, likely providing certain enhanced rod rigidity at chemically bonded locations. However, due to thermal expansion and contraction mismatch at clad-pellet interface region, during thermal cycling events of nuclear fuel operations, such a chemical bond is expected to be broken as shown from post-irradiation examination (PIE) of Catawba mixed uranium-plutonium oxide (MOX) SNF where the crack profile existed in the chemical bond region paralleled along the pellet-clad interface. Thus, the chemical bond effect on the SNF's enhanced rigidity is very limited.

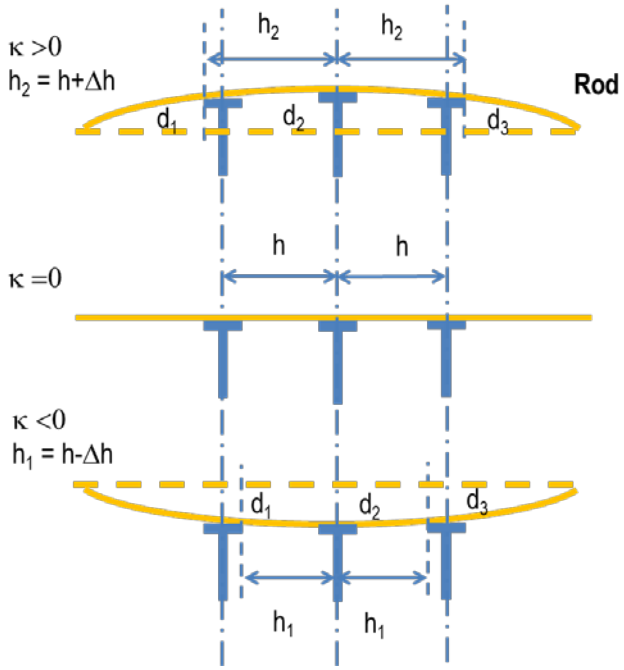

Figure 4. Deflections measured by LVDTs may be at different points from initial positions, and sensor spacing *h* needs to be corrected.

A polycarbonate rod (0.4375 in. diameter and 6 in. length), specimen PC01, was tested under -6 mm and +6 mm rigid arm end displacements with disk-head LVDTs. The curvatures in the positive and negative directions appeared to be quite different (Figure 5).

The same specimen (PC01) was tested with the same level of applied displacement, except curvatures were based on chisel-head LVDTs. The curvatures in both directions were close to 2 m^{-1}. The repeatable results indicated that PC01 behaved elastically, and the effect of chisel-head LVDTs on the curvature was negligible.

Analysis revealed the following:

- For a positive curvature induced by tension on the U-frame, a sensor adjustment of 2.90 mm is needed to have the disk-based measurement match the chisel-based measurement; this results in a 50% reduction in curvature measurement.
- For a negative curvature induced by compression on the U-frame, a sensor adjustment of 2.40 mm is needed for the disk-based measurement to match the chisel-based measurement; this results in a 40% increase in curvature measurement.

Based on the sensor spacing adjustments obtained for both conditions, a new *half gauge length* concept was developed and is discussed in next section.

1.3.1 The Half Gauge Length Approach for LVDT Sensor Spacing Adjustment

The bent rod is considered as an elastic curve that can be represented by part of a circle with radius R (**Figure 6**). The half gauge length can be expressed by arc AB, whose central angle is θ,

$$L_g / 2 = \theta \cdot R \qquad \text{(a)}$$

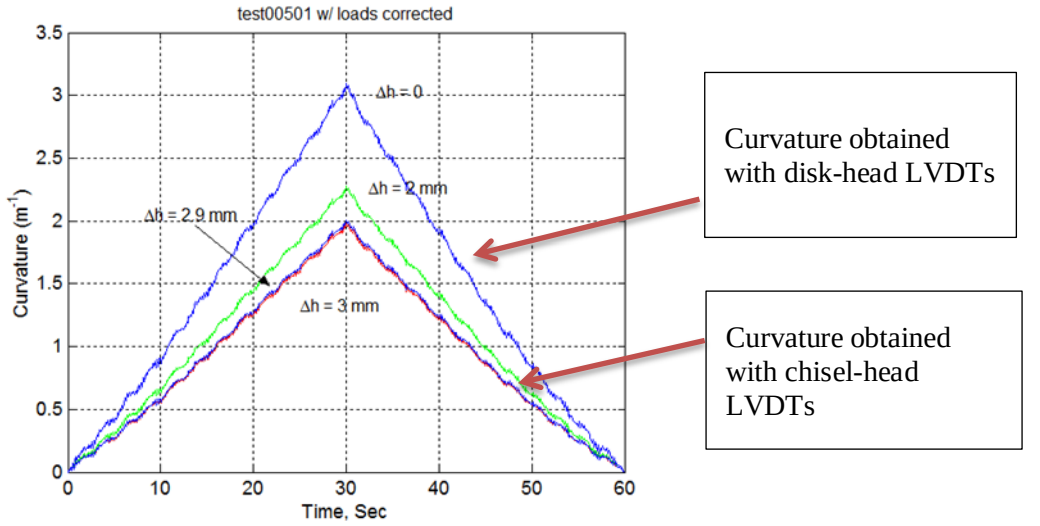

(a)

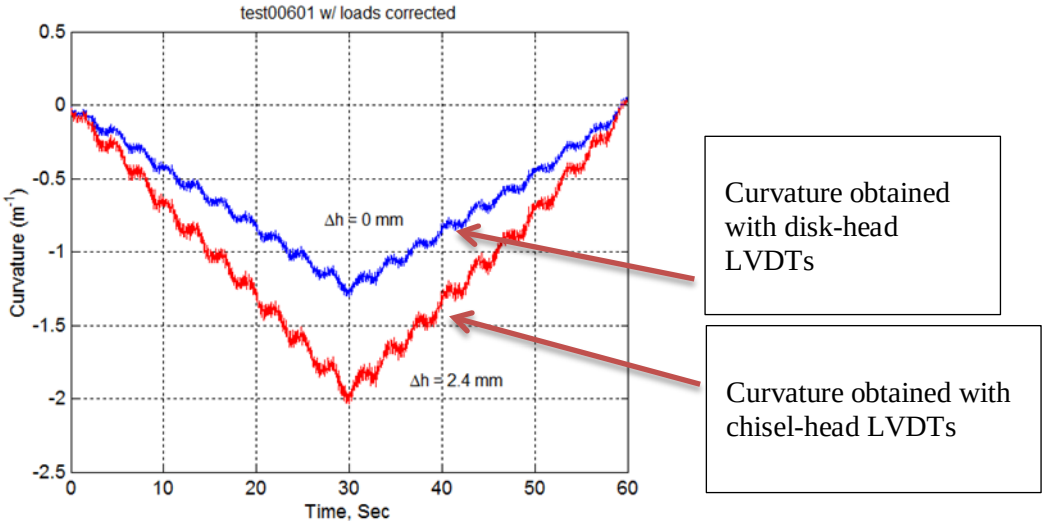

(b)

Figure 5. (a) For a positive curvature induced by tension on the U-frame, the sensor must be adjusted 2.9 mm so that the disk- and chisel-based measurements match; (b) for the negative curvature induced by compression on the U-frame, the sensor must be adjusted 2.4 mm so that the disk- and chisel-based measurements match.

The deflection BD of the bent rod at the middle LVDT is measured as d_2 and can be expressed in terms of chord AB:

$$d_2 = \overline{AB}\sin\angle BAD \text{, where } \angle BAD = \angle ABC = \theta/2.$$

$\angle ABC$ is so small that

$$\sin \angle ABC \cong \angle ABC = \theta / 2,\ \overline{AB} \cong L_g / 2.$$

So,

$$d_2 = L_g / 2 \cdot \theta / 2. \tag{b}$$

Dividing left and right sides of Eq. (a) by d_2 and $L_g/2 \cdot \theta/2$ of Eq. (b), respectively, results in

$$L_g / 2 = \sqrt{2 d_2 \cdot R}. \tag{c}$$

It is known that the R is the inverse of curvature, so

$$L_g / 2 = \sqrt{2 d_2 / \kappa}. \tag{9}$$

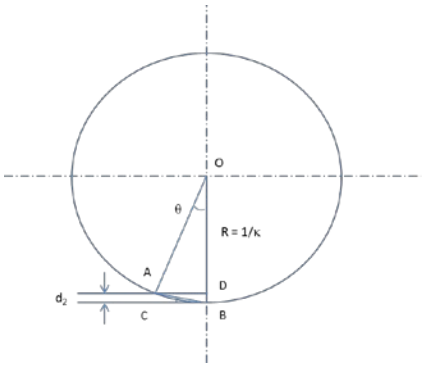

Figure 6. Diagram of circle showing quantities in calculating half gauge length of bent rod.

While the magnitude of the half gauge length bias adjustment is the same whether the rod is bent in a positive or negative direction, it must be applied appropriately according to the flexure direction. Resolving Eq. (9) to accommodate flexure direction results in the following relation:

$$d_{2p}^{+} / \kappa_p^{+} \mid_{h_2 = h + \Delta h} = d_{2p}^{-} / \kappa_p^{-} \mid_{h_1 = h - \Delta h}. \tag{10}$$

The spacing correction Δh can thus be obtained by solving Eq. (10).

Application of the bias correction was tested using a polycarbonate rod 11.11 mm in diameter and 152.40 mm long. A displacement control was used at ±6 mm at each loading point. With this input, the rod was expected to behave elastically. Note that the flexural rigidity of rod EI is 1.80 Nm^2, so the curvature of the rod can be effectively calculated when the moment M is provided, namely,

$$\kappa = M / EI. \tag{11}$$

The three LVDT-based curvature curves obtained with a disk probe are presented in Figure 7 with and without the correction applied.

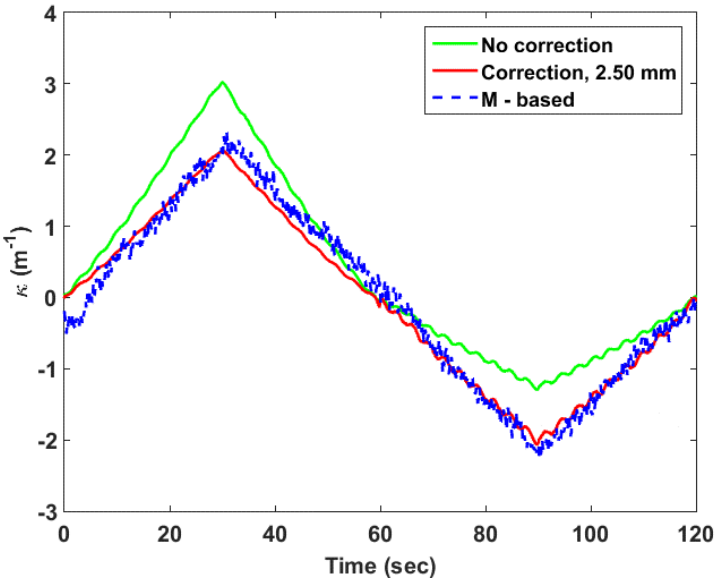

Figure 7. Curvature measurements of polycarbonate rod using the M-based estimate and the disk type probe with 2.50 mm sensor spacing correction.

Implementing the correction procedure in the polycarbonate rod example suggested that a Δh of 2.50 mm is needed. The corrected curvature showed a good correspondence with the M-based curvature according to Eq. (11). In the monotonic test, Δh = 2.50 mm obtained from the calibration can be used for spacing correction in data analysis. In the reversed cyclic bending, the Δh is applied directly using Eq. (10) because the peak and valley pair is available in the data block. This is preferred since with the same loading in both directions, the flexure/curvature of an irradiated fuel rod can be asymmetric due to local bonding and pellet-cladding interface effects.

1.3.2 Curvature Adjustment for LVDT Stem Dynamic Stability

To verify the curvatures calculated from the three LVDT readings under dynamic loading, a strain gauge was introduced as a verification method. A strain gauge was mounted on calibration rod SS30402 and tested under load control at varying frequencies. Correction was applied to the probe sensor spacing as shown in Figure 8.

Peak and valley strains based on the corrected exhibit have demonstrated a trend similar to the response of strain gauge as a function of driving frequency, as shown in Figure 8. The levels of the three-LVDT-based strains are usually higher than those of the strain gauge in both peak and valley directions, which may be induced by the dynamic response of LVDT. The overestimate is ~18% at 5Hz. Therefore, all curvatures and gauge strains reported here are reduced by 18%, in addition to the LVDT bias correction to consider the variance induced by LVDTs stem dynamic instability.

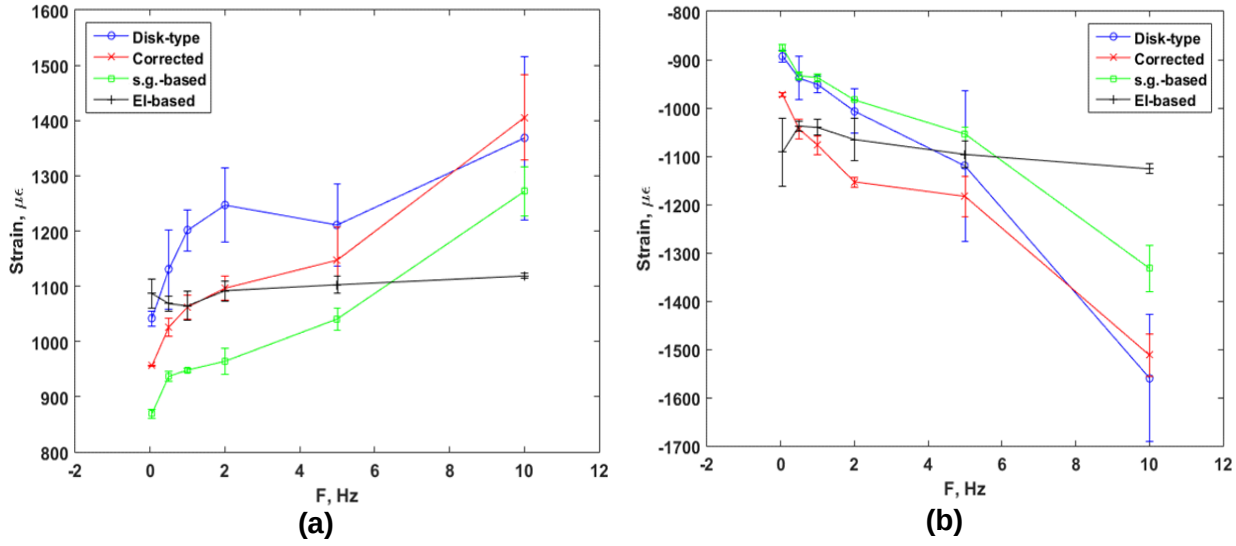

Figure 8. Variations of (a) peak strain and (b) valley strain as a function of driving frequency. At 5 Hz, the corrected strain level is about 18% higher than the strain gauge estimate for peak and valley strain plots.

1.4 CIRFT Test Protocol

The test system was calibrated under static and dynamic testing conditions using three surrogate rods consisting of stainless steel cladding and alumina pellets. The system was tuned and benchmarked by testing several specimens.

1.4.1 Static CIRFT Testing

The purpose of static testing is to estimate flexural strength and the associated flexural deformation data for the SNF rod to be tested. The static test measures the bending strength of *fueled* SNF rods so that the contribution of the fuel to the SNF rod's bending strength can be evaluated. Analysis of the static test results also provides a reference to establish the dynamic testing matrix for the rod. Static testing is carried out using displacement control. It involves ramping both loading arms of the U-frame at 0.1 mm/s up to 12 mm, where 12 mm displacement is the machine stroke capacity. The procedure below is followed.

1. Perform the standard CIRFT static bending test beyond SNF rod yielding to failure or up to device displacement or loading capacity.
2. If the machine capacity is reached before specimen failure or the specimen yield strength is reached, repeat unidirectional static testing using the same conditions for a few more loading/unloading cycles or to specimen failure, whichever comes first.
3. If the SNF rod does not fail after 3–4 static loading/unloading cycles, apply the cyclic dynamic test to fracture the test specimen to support postmortem examination. Such a cyclic test is called a *post-static dynamic test*, and it is performed to differentiate the test results from other dynamic tests since it is likely that the static test has deflected the sample beyond yield and has perhaps affected the bonding, in addition to significant residual stress generated in clad materials.
4. Collect and weigh any fuel fragments that may have dislodged during the test.

The loading processes to be used after the first loading cycle were suggested because the device may not have sufficient stroke to test these specimens to failure.

1.4.2 Dynamic CIRFT Testing

Dynamic testing consists of two major activities—dynamic real-time online monitoring and periodic quasistatic deformation measurements (see Figure 9).

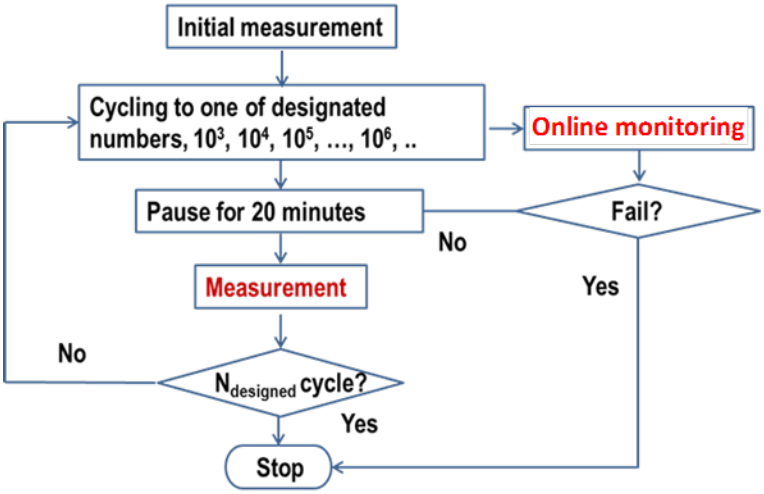

Figure 9. Flowchart for cyclic testing of SNF rod.

The procedure is as follows:

1. Perform the dynamic cyclic test under constant load control using a sine wave input in reverse bending mode.
2. Set the cycle frequency at 5 Hz and select the amplitudes for individual cycle tests considering the target cycles to be achieved with each test.
3. Monitor the SNF fatigue evolution with defined intervals, performing static measurements of (a) the rod deformation at the end of each target cycle with a frequency of 0.05 Hz and (b) reduced loading amplitude relative to the dynamic loading amplitude under displacement control.
4. Stop the dynamic test when failure/clad fracture is detected or the preselected number of cycles is reached.
5. Weigh any fuel fragments that fall out of the fracture.

1.4.3 Data Processing

Measurement data and online monitoring data are converted into the applied moment and curvature based on the load channel (load1 and load2) information, the loading arm length (101.60 mm), and LVDT data (LVDT1, 2, and 3). This information is used to generate the time series plots of moment and curvature and the moment-curvature hysteresis loops such as those illustrated in Figure 10 for D1. The data are processed using the approach defined in Section 1.2 for the applied deflection, moment, strain, and stress. The calculation of stress disregards the difference of elastic moduli between cladding and pellets. The gauge strain is then:

$$\varepsilon = \kappa \times y_{max}. \tag{12}$$

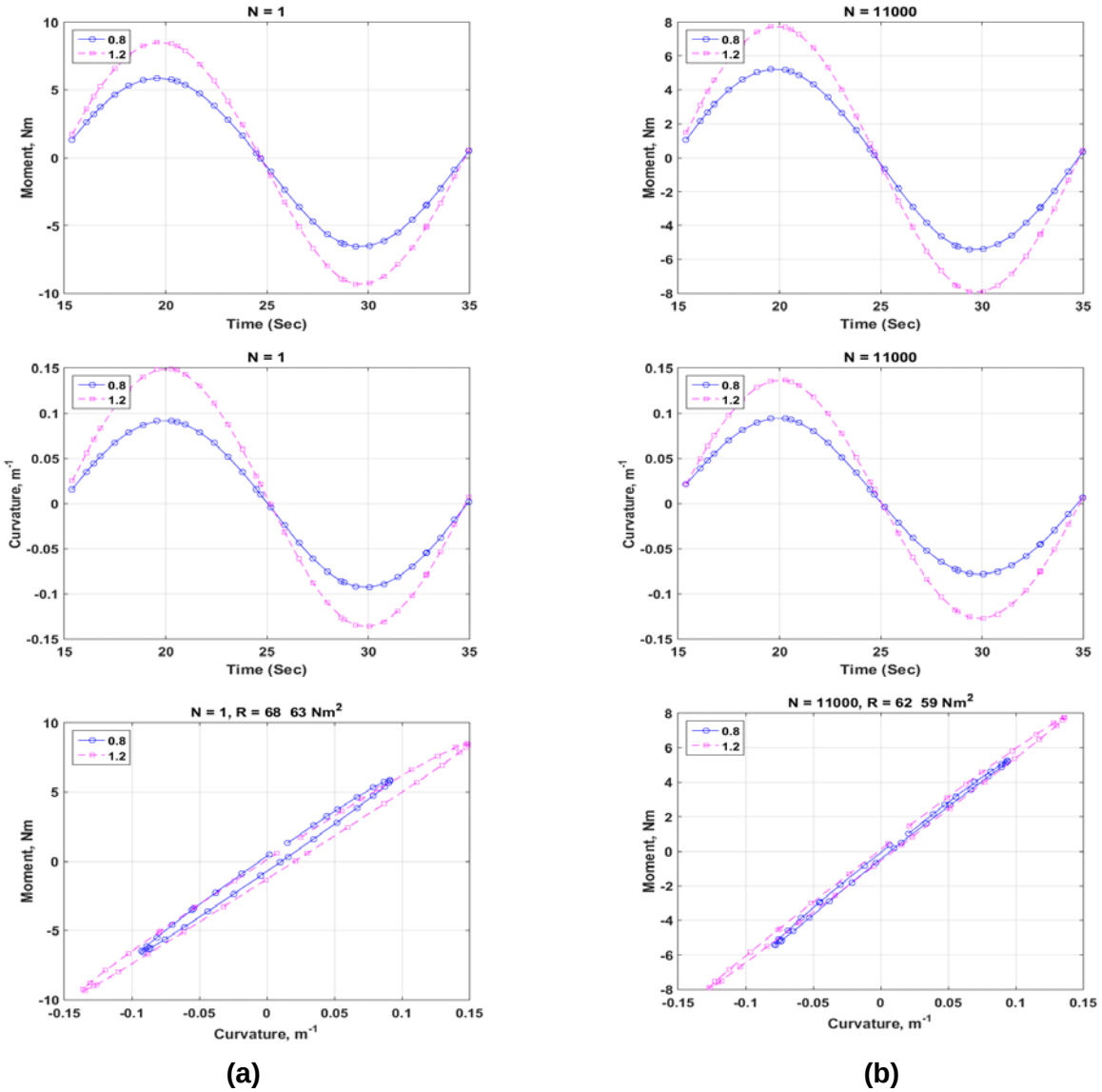

Figure 10. Moment and curvature as a function of time and moment-curvature loops based on measurements when (a) N=1 and (b) N = 111,000 cycles for D1 (607C4B). Measurements were made with 0.8 and 1.2 mm relative displacements; $N_f = 1.1 \times 10^5$ cycles under ±15.24 N·m, 5 Hz.

The relations of moment-range versus curvature-range and flexural rigidity are illustrated in Figure 11.

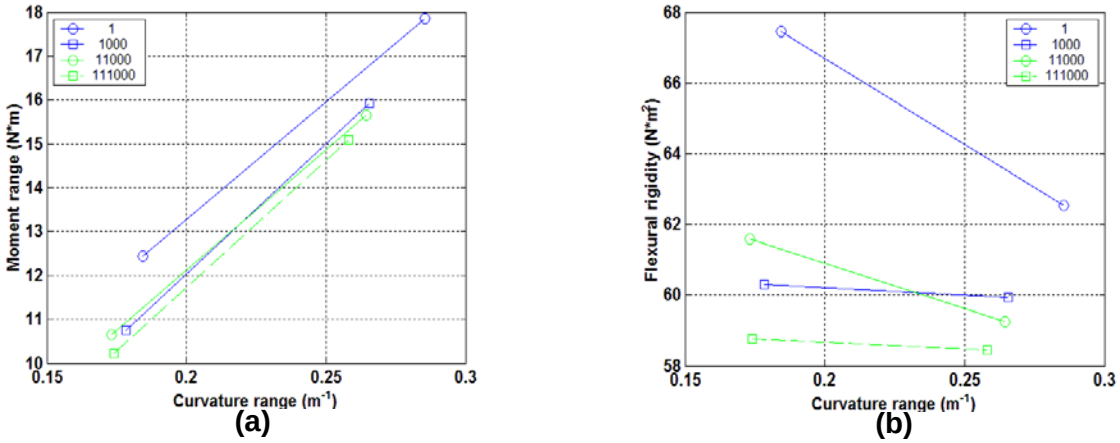

Figure 11. (a) Moment-curvature relation and (b) moment-flexural rigidity relation at various numbers of cycles for D1 (607C4B); $N_f = 1.1 \times 10^5$ cycles under ±15.24 N·m, 5 Hz.

Most of the rigidity degradation occurred in the first 1,000 cycles. Variations of these quantities as a function of the number of cycles are provided in Figure 12. The flexural rigidity of the measurements at two displacements converged before the failure and exhibited a slightly declining trend.

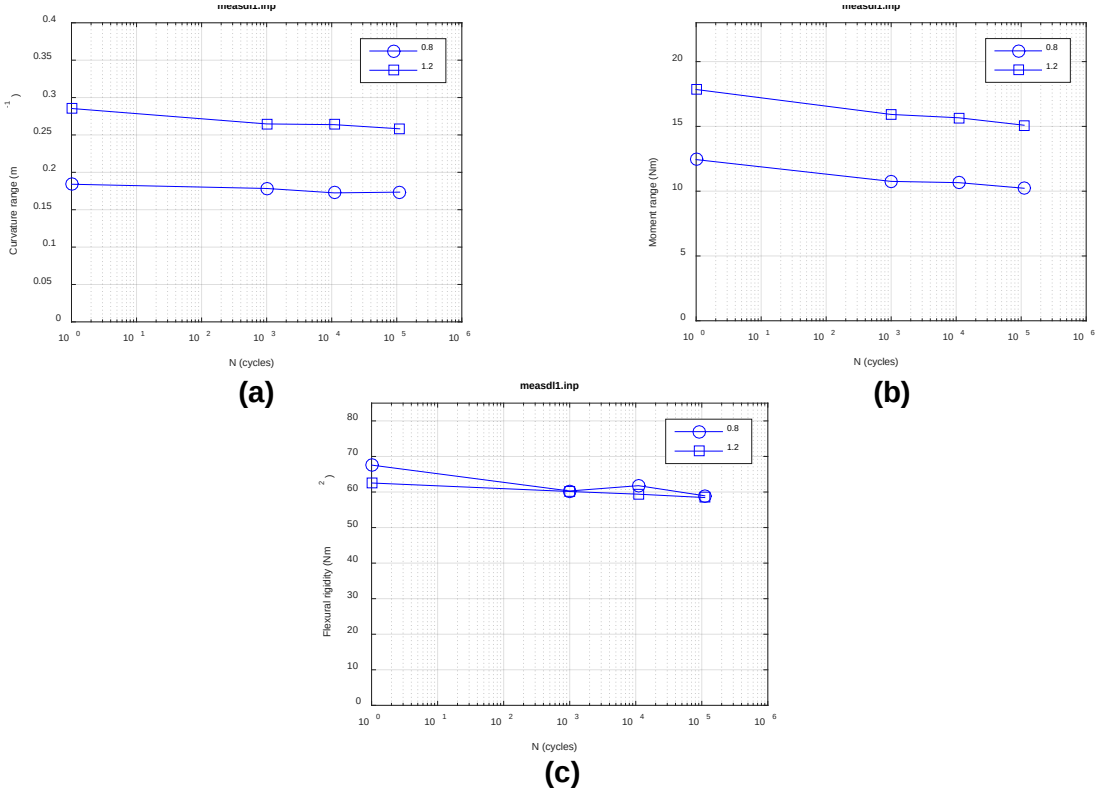

Figure 12. Variations of (a) curvature range, (b) moment range, (c) and flexural rigidity as a function of the number of cycles for D1 (607C4B); $N_f = 1.1 \times 10^5$ cycles under ±15.24 N·m, 5 Hz.

The curvature, moment, and rigidity based on online monitoring data are presented in Figure 13.

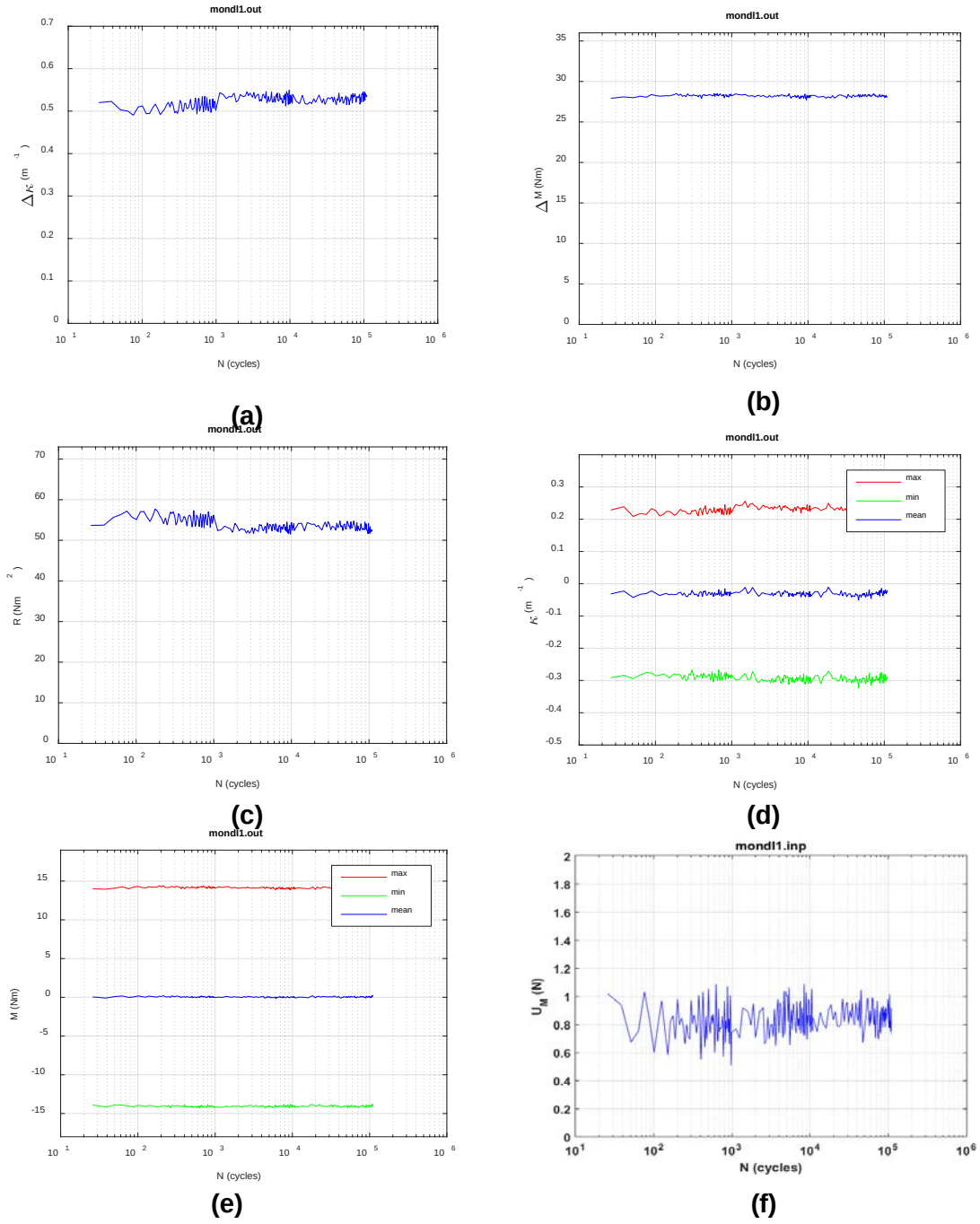

Figure 13. Variations of (a) curvature range, (b) applied moment range, (c) flexural rigidity, (d) maximum and minimum values of curvature, (e) maximum and minimum values of moment, and (f) flexural hysteresis as a function of number of cycles for D1 (607C4B); $N_f = 1.1 \times 10^5$ cycles under ±15.24 N·m, 5 Hz.

The online monitoring showed an initial flexural rigidity of about 55 N·m^2, a little lower than that observed in quasistatic measurements. This occurred because different loading conditions were used in quasistatic measurement and online measurements. A curvature range of less than 0.3 m^{-1} was used in the

quasistatic measurement, which is lower than that used in the online measurement of the cyclic test, to ensure that the measurement process did not affect the dynamic cycle data.

In general, the flexural rigidity tends to increase with decreasing curvature. This is likely due to a better interface bond at a relatively low load resulting in less stiffness reduction. Overall, a stable rod response was exhibited before the final failure. The curvature-cycle history shown in Figure 13(d), it clearly indicated a non-symmetric deformation under reversal loading, where the cladding tension site has much higher deformation (about 1.6 times) compared to that at cladding compression site. This phenomenon could be the consequence of debonding at the PPI and the stress concentration occurring at the PPI region at the tension side of the cladding, in addition to sensor probe sensitivity.

In general, flexural hysteresis, shown in Figure 13(f), remains quite uniform throughout the reversal bending test except with slight reductions at higher cycles. Similar flexural hysteresis reduction at a higher cycle was also observed from the periodic measurement data shown in Figure 10; at 1.1×10^5 cycle, the moment-curvature loading and unloading curves had a smaller loop compared to that of 26^{th} cycle. Under relatively low loading amplitude of dynamic testing, the clad or fuel pellet would be mainly under linear elastic behavior. The root cause of hysteresis energy dissipation under cyclic loading could be the system's nonlinear response associated with segment pellets induced by stress concentration at interface regions, as well as uncertainly resulting from sensor probe sensitivity.

Figure 14 shows the moment and curvature time history, which are based on online monitoring data collected during dynamic test at 26 and 1.1×10^5 cycles. The asymmetrical curvature deformation mode of the tested rod at the 26^{th} cycle and 1.1×10^5 cycle was also observed.

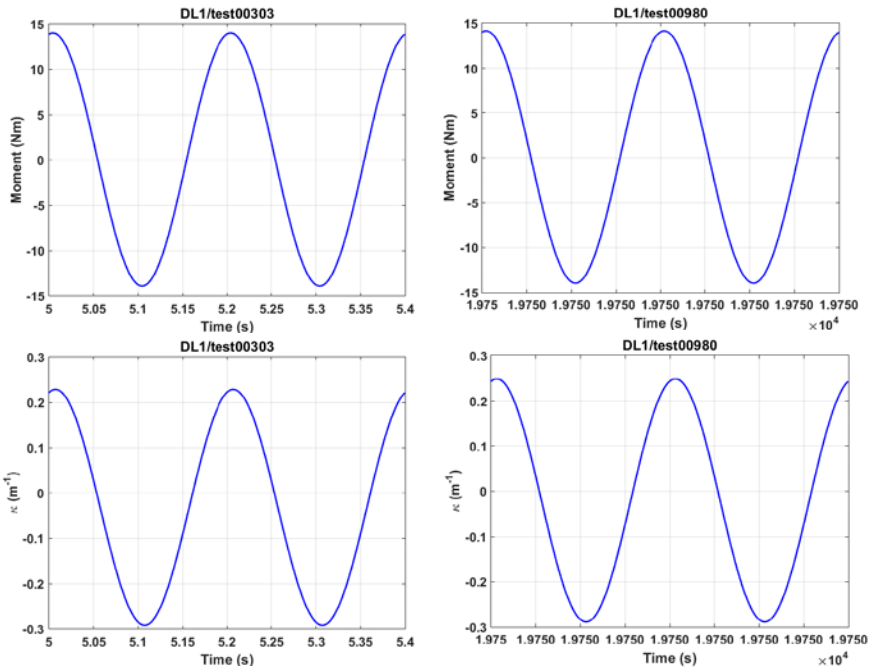

Figure 14. Moment and curvature as a function of time and moment-curvature loops at (a) 26 and (b) 1.10×10^5 cycles; results based on online monitoring. The unsymmetrical curvature deformation of the tested rod at the 26^{th} cycle and 1.1×10^5 cycle was also observed.

1.4.4 Flexural Rigidity Calculation

The SNF system contains multiphase components such as cladding, pellets, and oxide, so an SNF rod is far from being considered an ideal homogeneous material. However, if the cladding-pellet interfaces and PPIs are perfectly bonded, a homogenized rod flexural rigidity *EI* can be expressed as

$$EI = E_c I_c + E_p I_p \,, \tag{13}$$

where I_c and I_p are moments of inertia of the cladding and pellet, respectively, and the value of I_p is based on dimensions provided in Ruzauskas and Fardell's 2001 Electric Power Research Institute (EPRI) report [17]. E_c and E_p are the Young's modulus of the cladding and pellet. The associated stress and strain evaluations of Eqs. (5) and (6) can still be used. Unfortunately, because the cladding-pellet and PPIs are not perfectly bonded (either mechanically or chemically), the effective flexural rigidity is reduced by a bonding efficiency (BE) correction factor:

$$EI = E_c I_c + E_p I_p - F, \tag{14}$$

where F is the correction factor, which depends on interface *BE* and the fuel pellet and cladding aging properties, as well as cyclic loading amplitudes. This hypothesis was further validated in Wang and Jiang's "Quantification of CIRFT System Biases and Uncertainties When Testing High-Burnup Spent Nuclear Fuel" [18]. The CIRFT data are not resolved to a low enough level to specifically differentiate the *BE*. However, based on the periodic static measurements of CIRFT dynamic testing, the *EI* data trend indicates that pellet-pellet bonding is weak and likely becomes debonded after only a few CIRFT cycles. The resulting reduction of flexural rigidity is evidenced by a significant variation in LVDTs measured curvatures between the cladding tensile stress and cladding compressive stress regions shown in Figure 10. At the compressive cladding stress region, the fuel reinforcement remains intact in the form of the fuel pellet pinning effect. This results in a shift of the neutral axis in an SNF system under reversal bending.

This phenomenon was also observed from the CIRFT test online monitoring data, where the tensile cladding stress stage shows a higher curvature reading than the compressive stress stage, as shown in Figure 13(d). The *EI* values also change accordingly in each moment reversal cycle. This is shown in the moment-curvature plot of Figure 10 above, where the *EI* (the slope of moment-curvature) in the clad compression cycle is higher than that of the clad tension cycle. Furthermore, a detailed three-dimensional FEA with a 6.25 N·m uniform moment also reveals that the localized strain in the cladding at the pellet-pellet-cladding interface region is about three to four times (depending on the interface cohesive bond parameters) [18] that of the global strain for the tensile cladding stress region. The associated localized stress is about 2.6 times the average global tensile cladding stress. Another complication is that the neutral axis of the SNF rod will no longer reside in the geometric center of the SNF system, and the EI value will shift alternatively around the geometry center under cyclic loading reversals [18,19]. Therefore, the conventional approach, as stated in Eqs. (10) and (11) based on a global M-κ consideration, is no longer valid for describing the cladding failure mechanism associated with localized flexural rigidity degradation at the rod's PPI.

To generate the stress-strain relationship associated with M-κ, a first order approximation approach commonly used for an isotropic/homogeneous structure was adopted to translate the global CIRFT M-κ data into the equivalent stress and strain data of cladding. Where the SNF rod's moment of inertia is written as $I = I_c + c \times I_p$, I_c and I_p are moments of inertia of cladding and pellet, respectively, and $c = E_p/E_c$ (because the baseline Young's modulus of the oxide fuel is twice that of the cladding, c is likely greater than 1). In the proposed equivalent stress and strain approach, c is set to 1, which implies a 50% reduction in pellet Young's modulus, to consider the radiation induced degradation of the HBU fuel pellet, where the pellets are assumed to be perfectly bonded with the cladding at the PPI. Furthermore, setting c = 1 implies the same *E* properties for the fuel and the cladding, which allows Eqs. (10) and (11) to be used

under the homogenous properties hypothesis for an equivalent stress and strain evaluation. Generally, the moment range (ΔM), curvature range ($\Delta\kappa$), and flexural rigidity EI are used to characterize the mechanical properties of the fuel rod. These are defined as:

$$\begin{aligned} \Delta M &= M_{max} - M_{min,} \\ \Delta\kappa &= \kappa_{max} - \kappa_{min,} \\ EI &= \Delta M / \Delta\kappa, \end{aligned} \tag{15}$$

where the subscripts *max* and *min* represent the maximum and minimum waveforms.

Under a load-controlling mode, the curvature response of a rod is not necessarily symmetric in one cycle of loading. The offset of the M-κ loop on the κ axis with respect to the origin can be described by a mean value of curvatures, κ_m:

$$\kappa_m = 0.5 \times (\kappa_{max} + \kappa_{min}), \tag{16}$$

and the maximum of absolute curvature extremes, $|\kappa|_{max}$, is

$$|\kappa|_{max} = \max(|\kappa_{max}|, |\kappa_{min}|). \tag{17}$$

For a given specimen, the $|\kappa|_{max}$ given by Eq. (16) corresponds to the curvature that creates the maximum tensile stress in the cladding. The resistance force of the CIRFT system may be significant, depending on the amplitude of the rigid arm movement. The CIRFT system static resistance force was measured at different displacement levels without a specimen loaded. The net applied load at each displacement level was estimated by subtracting the measured resistance from the applied static test load shown in Figure 15.

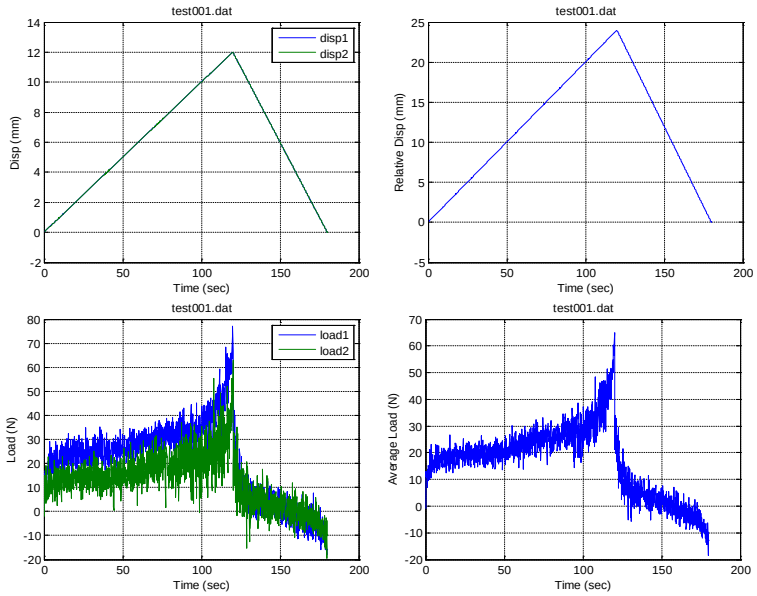

Figure 15. Empty-run conducted without specimen installed for which the load and displacement were plotted; associated with static test on D1.

The CIRFT system resistance was tested and evaluated by using empty runs in which the specimen was not loaded on the testing machine. These empty runs were conducted in the specified period or whenever the calibration is needed.

2. STATIC CIRFT TEST DATA ANALYSES

2.1 Characteristics of Moment-Curvature Curve

The CIRFT test moment-curvature responses of SNF rod specimens were similar. They are characterized by two distinct linear responses, EI1 and EI2, followed by EI3, a nonlinear response during the loading and a linear response upon unloading. It was observed that when reloaded, the rod followed the unloading curve linearly and proceeded with the nonlinear response after passing the previous maximum load. Such loading/unloading/reloading responses occur in many mechanical systems where irreversible changes take place during loading [3]. An effort was made to characterize the moment-curvature response based on characteristic points to facilitate understanding of the test results. The values for EI1, EI2, and EI3 were obtained, corresponding to the slopes of the first and second linear segments and of the unloading segment, by using curve fitting with the first order polynomial (Figure 16).

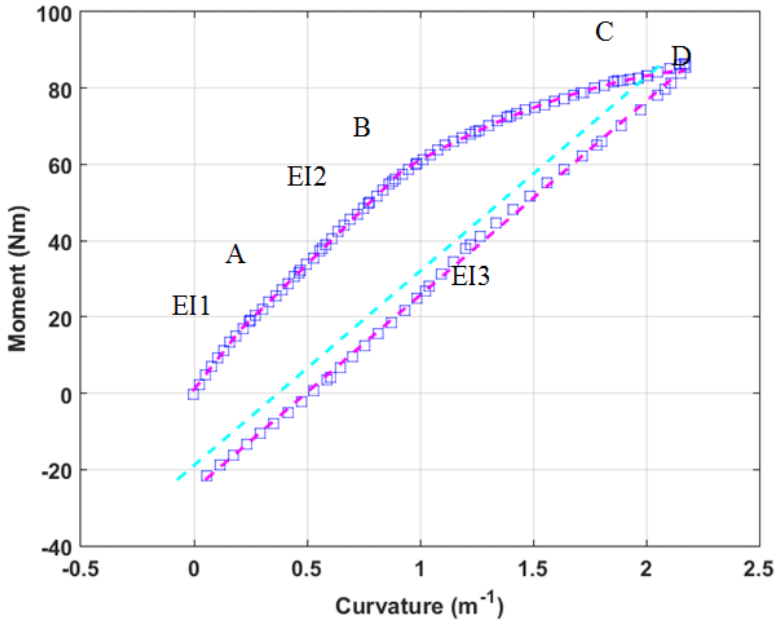

Figure 16. Characteristic points of moment-curvature curve.

The characteristic curvatures and moments at the slopes' changed points A and B were then identified. In addition, the moment at point C corresponding to a 0.37 m^{-1} irreversible curvature, or 0.2% equivalent plastic strain, was found by using a line with the same slope as that of unloading, EI3, and horizontal axis intercept 0.37 m^{-1}. The quantities corresponding to points A, B, and C are designated as κ_A, κ_B, κ_C, and M_A, M_B, and M_C. The results are summarized in Table 1. For an as-irradiated specimen, EI1, EI2, and EI3 are generally in decreasing order, with a marginal difference between EI2 and EI3. The characteristics derived from equivalent stress-strain curves are provided in Table 2. The LMK with Zry2 cladding has similar dimension as that of HBR with Zry-4 cladding, except LMK data have higher curvature than HBR data. In general, due to relatively smaller geometry of M5 cladding compared to Zry-4 cladding, the flexural rigidity of SNF with M5 cladding is lower than that of SNF with Zry-4 cladding.

Table 1. Characteristic points and quantities based on curvature-moment curves.

	Spec ID	Seg. ID	EI1	EI2	EI3	κ_A	κ_B	κ_C	κ_D	M_A	M_B	M_C	M_D
			$N{\cdot}m^2$	$N{\cdot}m^2$	$N{\cdot}m^2$	m^{-1}	m^{-1}	m^{-1}	m^{-1}	N·m	N·m	N·m	N·m
HBR	S1	606C3C	76.34	58.384	50.939	0.204	0.923	2.006	2.153	16.524	58.518	83.279	84.702
HBR	S2	605D1E	73.016	60.848	52.699	0.32	1.009	2.001	2.154	20.18	62.133	85.914	87.294
HBR	Dcal	609C5	71.517	59.369	47.101	0.311	0.933	2.149	2.308	22.338	59.288	83.728	85.235
HBR	Scal	609C6	63.117	54.849	41.704	0.503	0.862	2.329	2.507	28.54	48.244	81.656	85.02
HBR	HR2*	607D4A	62.769	41.517	55.027	0.487	1.007	1.585	2.158	30.301	51.884	66.809	79.606
LMK	LMK01	574D-A	61.984	53.636	43.217	0.425	0.761	2.208	2.756	24.462	42.468	80.293	85.343
MOX	MOX01	MOX-A-11	34.308	26.269	26.833	0.292	1.204	1.88	2.685	8.643	32.603	39.256	46.76
MOX	MOX03	MOX-A-13	34.846	24.821	28.76	0.444	0.975	1.674	2.465	12.858	26.041	36.173	47.121
NA	NA3	651D3	29.738	26.154	25.529	0.545	1.13	1.946	2.845	14.312	29.611	39.082	46.805

*Hydride reorientation (HR) test sample

Table 2. Characteristic points and quantities based on equivalent stress-strain curves.

	Spec ID	Seg. ID	E1	E2	E3	ε_A	ε_B	ε_C	ε_D	σ_A	σ_B	σ_C	σ_D
			GPa	GPa	GPa	%	%	%	%	MPa	MPa	MPa	MPa
HBR	S1	606C3C	121.648	93.035	81.172	0.11	0.497	1.079	1.158	141.663	501.674	713.954	726.149
HBR	S2	605D1E	116.704	97.255	84.23	0.172	0.542	1.075	1.157	173.206	533.284	737.397	749.247
HBR	Dcal	609C5	114.654	95.178	75.511	0.167	0.501	1.154	1.239	192.306	510.412	720.813	733.788
HBR	Scal	609C6	101.069	87.83	66.781	0.27	0.463	1.251	1.346	245.417	414.854	702.162	731.089
HBR	HR2*	607D4A	99.543	65.841	87.266	0.262	0.542	0.853	1.161	258.53	442.672	570.012	679.201
LMK	LMK01	574D-A	83.219	72.011	58.023	0.243	0.434	1.261	1.574	187.571	325.63	615.663	654.39
MOX	MOX01	MOX-A-11	88.357	67.654	69.106	0.14	0.578	0.902	1.289	106.856	403.086	485.349	578.125
MOX	MOX03	MOX-A-13	89.742	63.926	74.069	0.213	0.468	0.804	1.184	158.974	321.959	447.234	582.584
NA	NA3	651D3	76.312	67.116	65.511	0.262	0.544	0.937	1.369	176.78	365.748	482.732	578.131

*HR test sample

For HBR rods, the E1 in the initial stage of the stress-strain curve was 101–125 GPa, and the 0.2% yield strength (σ_C) was 702–737 MPa. The ranges of the elastic modulus and the 0.2% yield strength appear consistent with the range of HBU HBR cladding [20]. However, the observation should not be overemphasized, because the results observed here based on equivalent stress approach and reflect a comprehensive global response of fuel rods with both pellets and cladding included. On the other hand, linear stages of HR2 are not defined as well as those in as-irradiated specimens. For as-irradiated rods, EI1 > EI2 > EI3. However, for HR2, EI1 > EI3 > EI2. Figure 16 above shows that the unloading curve drops rapidly before transitioning to a linear unloading response (EI3). This may indicate potential flaw formation such as gaps and cracks forming in the SNF system components or debonding occurring at the pellet-clad interfaces region. Static CIRFT testing indicated that the HR treatment has changed the SNF rod system's characteristics when compared to an as-irradiated SNF rod and the associated SNF deformation response and damage mechanism under loading.

The HR2 sample had a lower flexural rigidity than the as-irradiated test segments. It would be expected that HR2 could therefore survive greater deformation before failure than the as-irradiated segments. However, due to limitations of the CIRFT test device, this could not be confirmed. Nevertheless, the flexural rigidity is consistently reduced under the similar curvature, and the maximum moment level of HR2 was reduced from 86 Nm of the as-irradiated to 80 Nm.

2.2 Comparison of Static Results with Pacific Northwest National Laboratory Zry-4 and ORNL M5 Cladding Data

To investigate the contribution of fuel pellets in the fuel rod structure, analysis was performed to compare the measured static results to predicted values considering cladding alone. The cladding properties used for this analysis were obtained from a database maintained by Pacific Northwest National Laboratory (PNNL) [21]. The database allows the user to specify the cladding type, temperature, fluence, and cold work of the cladding of interest. For this study, the following values were specified:

- Cladding – Zry-4
- Temperature – 75 °F
- Fluence – 12×10^{25} n/m^2
- Cold work – 0.5
- Cladding ID – 9.25 mm
- Cladding OD – 10.7 mm
- Cladding thickness – 0.76 mm
- Calculated cladding moment of inertia (I_c) – 2.971×10^{-10} m^4

Using these values in the PNNL database, the Young's modulus E_c was given as 9.15×10^{10} Pa, the yield stress 919 MPa, the uniform elongation 0.00393, and the ultimate tensile strength 976 MPa. From these values, the engineering stress and strain values can be calculated. The ORNL M5 data were obtained from SNF M5 cladding tubing tensile tests as reported in Morris et al., "MOX PIE Fuel and Clad Examination Final Report" [22].

The CIRFT LVDTs measured the global rod deformation within the gauge section. Thus, the stress-strain estimate is an average evaluation throughout the gauge section that covers several pellet lengths with several PPIs. For the linear response of the cladding region of the rod away from the PPI, evaluation of the stress and strain can be a straightforward composite flexural rigidity formulation due to a relatively good bond at the pellet-cladding interface. However, due to the composite structure segmented pellets, the localized stress riser or curvature magnification at the PPI region cannot be estimated directly from the equivalent stress and strain approach; instead, it must be evaluated using FEA [18,19]. To estimate the contribution of the fuel pellets to the composite bending response, the comparison based on CIRFT M-κ

data was completed as shown in Fig. **17** below.

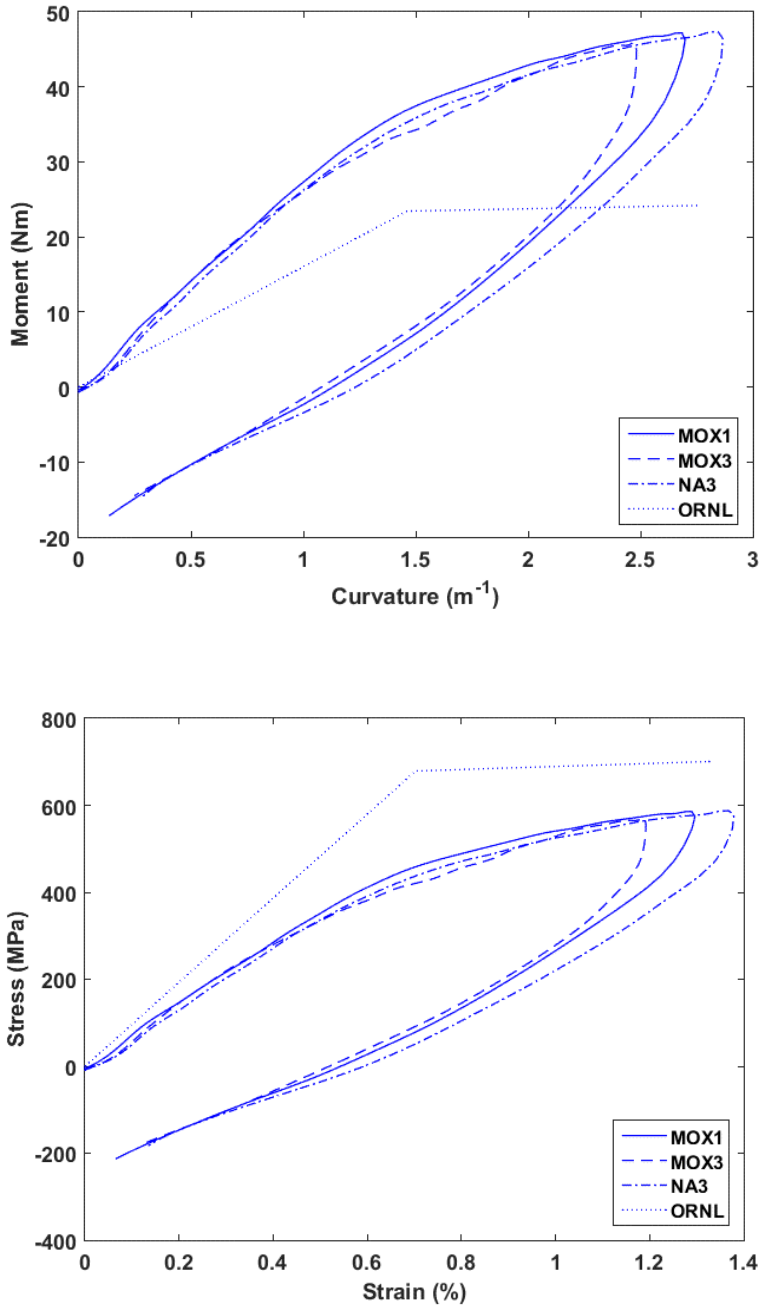

(a)

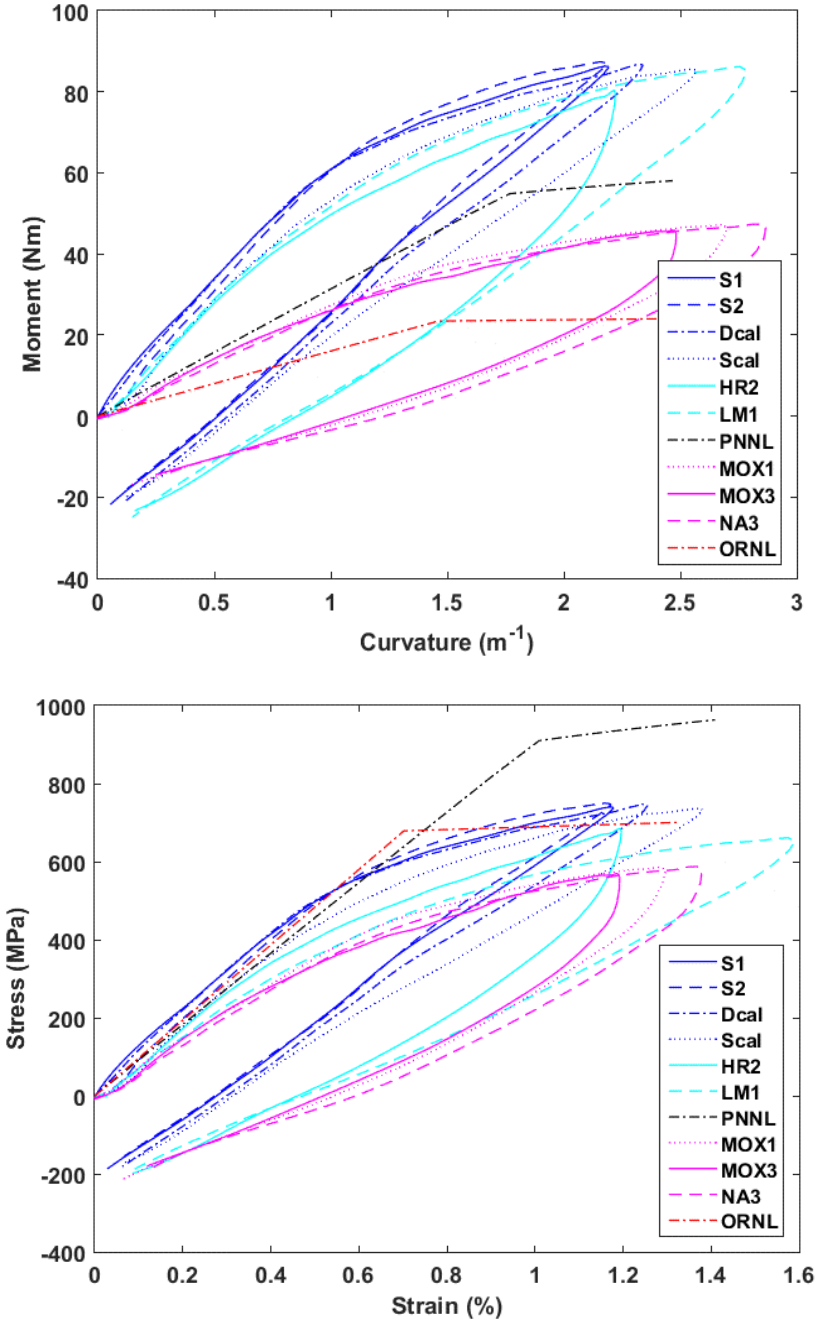

(b)

Fig. 17. (a) Comparison of static M5 CIRFT test data with theoretical ORNL moment-curvature derived from ORNL M5 cladding only stress-strain data, and (b) comparison of all static CIRFT test data with theoretical PNNL and ORNL moment-curvature derived from PNNL Zry-4 and ORNL M5 cladding only stress-strain data.

For comparison, the PNNL Zry-4 and ORNL M5 data (σ–ε curve) were converted to moment-curvature curves (shown in Fig. **17** as *PNNL* and *ORNL*) using the following equations, with the consideration of stress distribution that is appropriate for a thin-walled tube under uniform bending,

$$M = \sigma \cdot I / y_{max,} \tag{18}$$

and,

$$\kappa = \varepsilon / y_{max}, \tag{19}$$

where $I = I_c$, and other quantities have the same meanings as those in Eqs. (1–6).

The hypothetical *cladding only* moment-curvature response was plotted, together with moment-curvature response of the HBU fuel rod system as shown in Fig. 17, where data for the SNF rod show much higher flexural rigidity compared to data from PNNL and ORNL with cladding alone. From the stress vs. strain plot, it also clearly indicated that the estimate equivalence stress of a composite SNF system is lower than that of the cladding-only stress-strain data for Zry-4 and M5 cladding. A comparison of CIRFT testing results with cladding-only rigidity based on PNNL and ORNL data is given in Table 3.

Table 3. Comparison of flexural rigidity results between CIRFT testing and PNNL and ORNL data.

	EI1 (N·M²)	**EI2 (N·M²)**	**EI3 (N·M²)**
HBR (Zry)	71.576	58.099	48.133
HR2 (Zry-4)	62.769	41.517	43.333
LMK (Zry-2)	61.984	53.636	43.217
PNNL data (Zry-4)	26.933		
MOX (M5)	34.577	25.545	27.7965
NA (M5)	29.738	26.154	25.529
ORNL data (M5)	16.458		

The data comparison for Zry-4 cladding materials shows a distinct difference from that of the HBU fuel rod systems which was observed in the slope of the PNNL data. The slopes of both the as-irradiated and HR-treated HBU fuel rod systems are greater than that shown in the PNNL data. By focusing on the initial slope between 0–15 N·m, the slope (flexural rigidity) of HBU fuel rods was approximately twice that of the PNNL data for cladding alone. The similar phenomenon was also observed for SNF rods with M5 cladding materials.

The increase of SNF rod system stiffness is attributed to the fuel's mechanical properties and moment of inertia. However, the measured flexural rigidity of a fuel rod system is much less than that estimated from a direct summation of $E_cI_c + E_pI_p$, assuming a perfect mechanical bond between the fuel and the cladding, perfect bonding between the PPIs and a single pellet. However, bonding at fuel-cladding and fuel PPIs is not perfect and evolves during the test, in addition to pellets' segmentation. The initial fuel-clad gap size also influences the system's response. Furthermore, due to segmental pellet structure, numerous stress concentration sites are created within cladding at PPIs in an SNF rod. In general, the stress concentration sites cause the structure to have accelerated aging or reduced lifetime as compared to the very same system without stress concentration sites or discontinuous materials interfaces. The stress concentration effect due to an HBU rod segment structure was further validated from the dynamic testing, where the CIRFT test specimens are all failed at PPIs. Moreover, the intensity of the stress concentration or the pellet-clad interaction is strongly dependent on the loading intensity. Thus, at a low loading level, the PPI stress risers are expected to be small, so cladding alone likely dictates the SNF rod's composite flexural response.

All these factors affect the degree to which the presence of fuel results in an increase in the rod's flexural rigidity relative to cladding alone. This research effort did not attempt to account for and quantify each of these factors. Thus, the preliminary conclusion based on CIRFT SNF static bending testing is that flexural rigidity was approximately twice what would be obtained if cladding properties alone were used to predict behavior.

2.3 The Equivalence Stress Approach Verification and Benchmark

2.3.1 Equivalent Stress-Strain Approach Methodology

The equivalent stress-strain methodology proposed in Section 1 is described below.

The equivalent stress was calculated using

$$\sigma = M \times y_{max}/I, \tag{3}$$

and, the equivalent strain is determined using

$$\varepsilon = \kappa \times y_{max}. \tag{4}$$

where, I is the moment of inertia of the composite SNF rod, and y_{max} is the maximum distance to the neutral axis of the test rod for the section and is measured by the radius of the cladding.

M-κ, which is a first order approximation approach commonly used for an isotropic/homogeneous structure, was adopted to translate the global CIRFT M-κ data into an equivalent stress and strain of the cladding. For this approximation, the SNF rod's moment of inertia is written as

$$I = I_c + c \times I_p, \tag{5}$$

where, I_c and I_p are moments of inertia of the cladding and pellet, respectively, and $c = E_p/E_c$. (Because the baseline Young's modulus of the oxide fuel is twice that of the cladding, c is likely greater than 1.) In the proposed equivalent stress and strain approach, c is set to 1, which implies a 50% reduction in the pellet Young's modulus to account for operationally induced degradation of the HBU fuel pellet.

The overall flexural rigidity is as follows, including the consideration of BE

$$EI = E_c I_c + c \times E_c I_p, \tag{20}$$

As shown in Fig. **17**, the *EI* (flexural rigidity) values decrease accordingly with increase of the curvature. The hypothesis of the equivalent stress-strain concept used in this report for different curvature ranges is examined herein.

Based on the HBR ***EI1*** data of 71.6 Nm² in Table 3, representing the flexural rigidity in the initial stage of bending loading, the associated c value evaluation is described below.

- E_c is the cladding Young's modulus of 91.5 GPa for HBU Zry-4 cladding. The outer diameter (OD) of the HBR cladding is 10.76 mm, and the inner diameter (ID) is 9.26 mm. The associated fuel pellet dimension is assigned as 9.26 mm in diameter.
- The estimated I_p is equal to 3.609×10^{-10} m^4, and the estimate I_c,is equal to 2.971×10^{-10} m^4. Substituting I_c, and I_p into Eq. 5, with $c = 1$, the estimated flexural rigidity based on the equivalent stress concept is 60.2 Nm², which is less than measurement *EI* data of 71.6 Nm². The estimated E_cI_c for cladding only is 27.18 Nm².
- By substituting measurement *EI*, E_C, I_c, and I_p into Eq. (20) one can solve $c = 1.345$. This is larger than 1, which is the equivalent stress approach's c value.

Based on HBR ***EI2*** data of 58.1 Nm², representing the middle stage of loading shown in Figure 16, the estimated *c* value is equal to 0.936. This is less than 1 of the equivalent stress-strain method.

At 78 Nm load, the higher end portion of the moment-curvature curve, the estimate HBR *EI* shown on Fig. **17**(b) is 44.88 Nm². The associated *c* value is estimated as 0.536, which indicates that the significant system property changes already occurred within the SNF composite system. However, since *c* is greater than zero, this implies that fuel pellet is still providing support to the SNF composite system at such a loading level. The estimated stress on the cladding surface is 855 MPa, which is lower than the yield stress of 919 MPa shown in Fig. **17**(b) from PNNL data.

The study described above it shows that the *c* factor chosen in the equivalent stress approach as a constant is not correct or self-consistent. It also shows that the *c* factor is strongly dependent on the localized moment-curvature profile. Thus, a variable or localized *EI derived from* the secant line of the moment-curvature trend curve, d*M*/dκ, is preferred at the target loading and deformation level. Based on this methodology, a modified equivalent stress-strain approach was developed accordingly and described below.

2.3.2 The Development of Modified Equivalent Stress-Strain Methodology

The CIRFT static test HBR Dscal data were used to illustrate the modified equivalent approach developed to translate the global moment-curvature measurement data into localized stress-strain profile data on the cladding surface. The moment-curvature plot and the associated equivalent stress-strain data of HBR Dscal, including PNNL data, are shown in Fig. **18**.

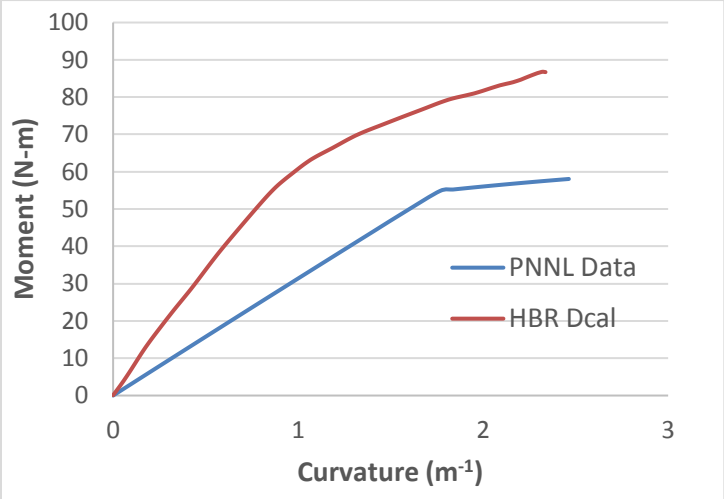

(a)

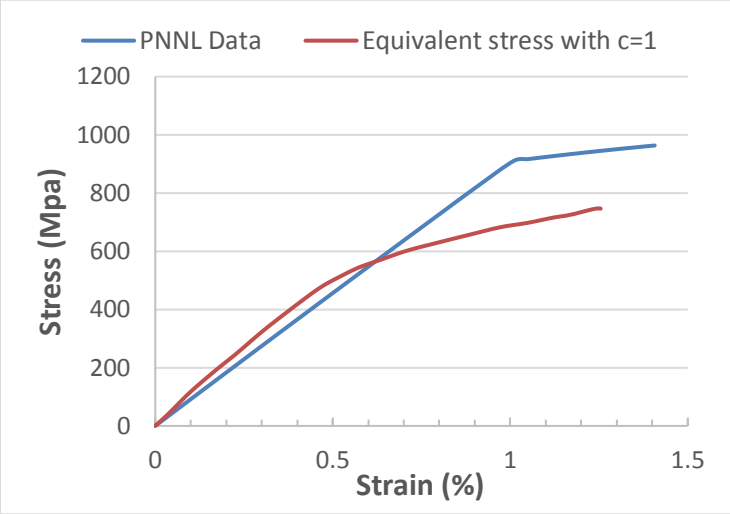

(b)

Fig. 18. (a) HBR Dcal *M*-κ trend curve, and (b) HBR Dcal equivalent stress-strain curve.

Fig. **18**(b) indicates a large discrepancy in the stress-strain profile between PNNL data and CIRFT test data than using equivalent stress approach, where a constant *c* value of 1 was used to estimate the moment inertia of the SNF composite system.

In general, the moment of inertia of a SNF rod can be estimated using Eq. (5), and *c* value provided in a modified equivalent stress approach is a variable that can be estimated locally from the secant line on a moment-curvature trend curve. In the static CIRFT testing on an SNF rod system, the postmortem examination normally revealed severe oxide spallations on the cladding surface; this is primarily due to weak interface shear strength at the zirconium-oxide layer and the 4Zry-4 cladding matrix interface under the flexural deformation. Thus, the oxide layer must be deducted from cladding radius for cladding surface stress evaluation.

In the modified equivalent stress approach, the localized *EI* can be obtained by dividing the moment *M* with the corresponding curvature κ, as shown in Fig. **18**(a), and the localized *I* value of Eq. (5) can then be estimated by dividing *EI* with E_c. Substituting *I* values into Eq. (3), the stress-strain profile on the cladding surface can be estimated accordingly, as illustrated in Figure 19. The y_{max} in Eq. (3) is equal to fuel cladding outer radius minus the surface oxide thickness. The oxide thickness of Dcal is 70–100 μm, so the mean value of 85μm was used as oxide thickness.

Figure 19 shows a significant improvement up to the Zry-4 yield strain level on the stress-strain curve evaluation from the modified equivalent approach compared to that of the equivalent stress approach, where PNNL data and the modified equivalent stress-strain profile have good agreement except at stress beyond the Zry-4 yield strain level. This is because there is a significant reduction in flexural rigidity *EI* beyond the cladding yield strain level. Therefore, the yield region's Young's modulus must be considered in addition to the initial linear-elastic Young's modulus of Zry-4 cladding material for estimating the *EI* using the modified equivalent stress approach. Development of the modified equivalent stress approach that covers the cladding strain level beyond the yield strain is discussed further in Section 2.3.3.

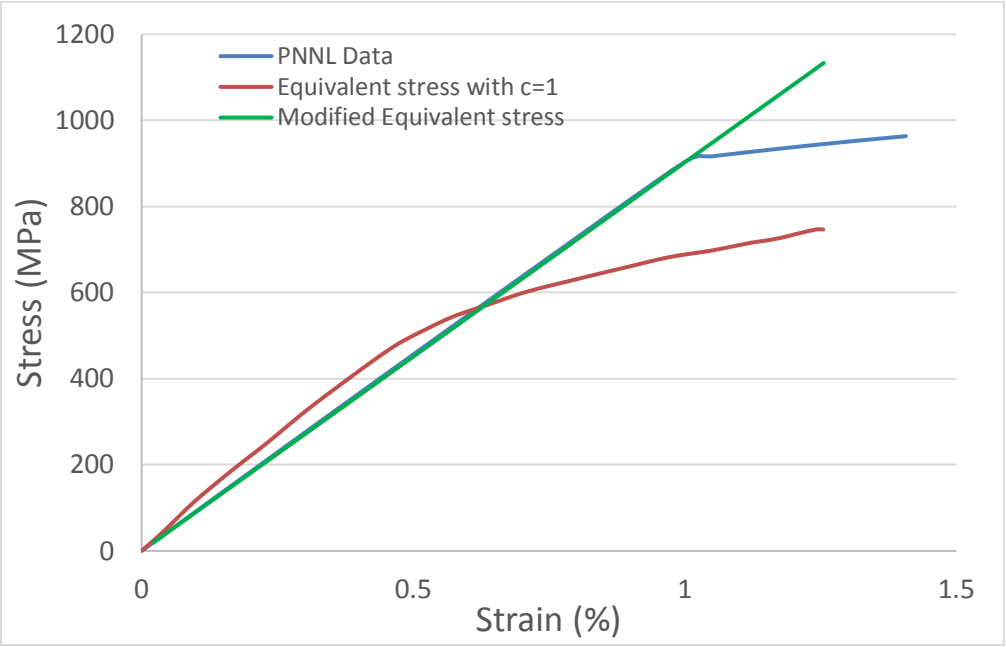

Figure 19. Comparison of stress-strain curves from PNNL data, equivalent stress with c=1, and modified equivalent stress approach for HBR Dcal CIRFT test data.

2.3.3 The Development of Modified Equivalent Stress Approach (MESA) for Strain Level beyond Yield Strain

Based on the bilinear model of PNNL Zry-4 cladding data shown in Fig. **18**(b), the cladding has a yield stress, σ_y, of 919.49 MPa; a yield strain, ε_y, of 1% strain; and two Young's modules, 91.5 GPa and 13.31 GPa, for linear-elastic and material hardening regions, respectively. From HBR Dcal data, at 1% yield cladding strain level, the associated cladding yield moment is at 79.97 Nm, and the corresponding curvature, κ_y, is 1.863 m^{-1}. The methodology developed for estimating the modified equivalent stress profile at the cladding surface beyond yield is described below. The stress level above the yield can be written as

$$\sigma = \sigma_y + \Delta\sigma, \qquad \Delta\sigma = \Delta M \times y_{max}/I, \tag{21}$$

where $\Delta M = M - M_{yield} = M - 79.97\ Nm$, and the associated moment inertia I can be written as shown below:

$$I = (\Delta M/\Delta\kappa)/E_2 = (\Delta M/\Delta\kappa)/(13.31\ GPa)\ ,$$

where $\Delta\kappa = \kappa - \kappa_y = \kappa - 1.863 m^{-1}$.

Based on Eq. (21), the stress level beyond yield was calculated accordingly. For the Dcal CIRFT test, the final estimated modified equivalent stress-strain curve on the cladding surface is very close to that of PNNL data as shown in Figure 20. The details of the Dscal-MESA data are provided in Table 4, which shows significant reduction in the flexural rigidity and the moment of inertia at higher bending loading level.

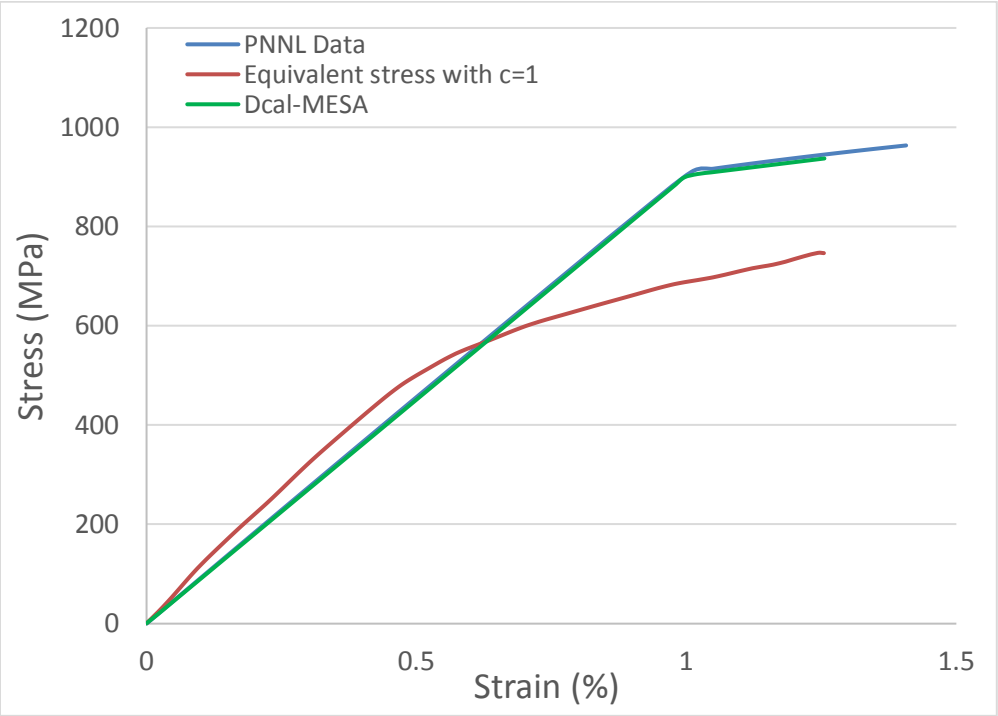

Figure 20. The comparison of stress-strain curves from PNNL data, equivalent stress with c=1, and modified equivalent stress approach with oxide thickness correction factor applied and yield zone modulus update for HBR Dcal CIRFT test data. The ORNL CIRFT stress-strain curve data match that of PNNL data.

The investigation described above indicated that MESA can effectively translate the global M-k response obtained from a CIRFT test to a local stress-strain curve on the SNF rod's cladding surface. Such an approach will be applied to CIRFT static test data as presented in the next section, and the same methodology will be applied to all the CIRFT dynamic data in the next report period.

Table 4. Detailed Dcal CIRFT static test results and the associated MESA stress.

Curvature	Moment	Strain	Flexural rigidity	Moment of inertia	Stress
m^{-1}	N-m	%	$N\text{-}m^2$	m^4	MPa
0.0000	0.09	0.0000			0.00
0.0390	2.68	0.0209	68.87	7.5269E-10	18.87
0.0719	5.04	0.0386	70.06	7.6570E-10	34.84
0.1006	7.21	0.0540	71.65	7.8303E-10	48.73
0.1266	9.24	0.0680	72.94	7.9714E-10	61.35
0.1518	11.18	0.0815	73.66	8.0504E-10	73.54
0.1729	12.74	0.0928	73.71	8.0558E-10	83.75
0.1729	12.74	0.0928	73.71	8.0558E-10	83.75
0.1777	13.09	0.0954	73.65	8.0492E-10	86.10
0.2054	14.99	0.1102	73.00	7.9780E-10	99.50
0.2340	16.88	0.1256	72.13	7.8831E-10	113.36
0.2532	18.12	0.1359	71.57	7.8221E-10	122.67
0.2532	18.12	0.1359	71.57	7.8221E-10	122.67
0.2625	18.72	0.1409	71.33	7.7952E-10	127.18
0.2905	20.53	0.1560	70.65	7.7214E-10	140.76
0.3185	22.30	0.1710	70.01	7.6511E-10	154.30

Curvature	Moment	Strain	Flexural rigidity	Moment of inertia	Stress
m^{-1}	N-m	%	$N-m^2$	m^4	MPa
0.3333	23.22	0.1789	69.66	7.6127E-10	161.47
0.3333	23.22	0.1789	69.66	7.6127E-10	161.47
0.3468	24.04	0.1862	69.33	7.5765E-10	168.04
0.3755	25.78	0.2016	68.65	7.5026E-10	181.93
0.4038	27.50	0.2168	68.10	7.4423E-10	195.62
0.4142	28.14	0.2223	67.94	7.4251E-10	200.67
0.4142	28.14	0.2223	67.94	7.4251E-10	200.67
0.4309	29.19	0.2313	67.75	7.4044E-10	208.76
0.4569	30.88	0.2453	67.57	7.3852E-10	221.38
0.4826	32.57	0.2591	67.48	7.3749E-10	233.84
0.4886	32.96	0.2623	67.46	7.3730E-10	236.74
0.4886	32.96	0.2623	67.46	7.3730E-10	236.74
0.5086	34.28	0.2730	67.40	7.3661E-10	246.43
0.5350	36.00	0.2872	67.29	7.3540E-10	259.18
0.5614	37.68	0.3014	67.12	7.3354E-10	272.01
0.5637	37.82	0.3026	67.10	7.3335E-10	273.11
0.5637	37.82	0.3026	67.10	7.3335E-10	273.11
0.5880	39.32	0.3156	66.87	7.3087E-10	284.86
0.6149	40.94	0.3301	66.58	7.2760E-10	297.93
0.6411	42.49	0.3442	66.27	7.2425E-10	310.62
0.6411	42.49	0.3442	66.27	7.2425E-10	310.62
0.6429	42.59	0.3451	66.25	7.2403E-10	311.47
0.6721	44.30	0.3608	65.92	7.2043E-10	325.61
0.7015	46.02	0.3766	65.60	7.1696E-10	339.86
0.7242	47.34	0.3888	65.37	7.1439E-10	350.87
0.7242	47.34	0.3888	65.37	7.1439E-10	350.87
0.7300	47.67	0.3919	65.31	7.1375E-10	353.67
0.7571	49.24	0.4064	65.04	7.1078E-10	366.79
0.7837	50.76	0.4207	64.77	7.0783E-10	379.68
0.8012	51.74	0.4301	64.59	7.0585E-10	388.17
0.8012	51.74	0.4301	64.59	7.0585E-10	388.17
0.8110	52.30	0.4354	64.48	7.0472E-10	392.94
0.8398	53.87	0.4508	64.15	7.0105E-10	406.85
0.8697	55.40	0.4669	63.70	6.9618E-10	421.35
0.8850	56.13	0.4751	63.42	6.9311E-10	428.77
0.8850	56.13	0.4751	63.42	6.9311E-10	428.77
0.9006	56.82	0.4834	63.09	6.8955E-10	436.32
0.9322	58.13	0.5004	62.36	6.8149E-10	451.62
0.9642	59.38	0.5176	61.59	6.7306E-10	467.14
0.9755	59.82	0.5237	61.32	6.7018E-10	472.63
0.9755	59.82	0.5237	61.32	6.7018E-10	472.63
0.9964	60.64	0.5349	60.86	6.6510E-10	482.75
1.0294	61.89	0.5526	60.13	6.5713E-10	498.73
1.0642	63.09	0.5713	59.29	6.4796E-10	515.60
1.0717	63.33	0.5753	59.09	6.4582E-10	519.23
1.0717	63.33	0.5753	59.09	6.4582E-10	519.23
1.1018	64.20	0.5915	58.26	6.3677E-10	533.82
1.1418	65.24	0.6129	57.14	6.2447E-10	553.19
1.1831	66.30	0.6351	56.04	6.1247E-10	573.22
1.1856	66.37	0.6365	55.98	6.1180E-10	574.42

Curvature	Moment	Strain	Flexural rigidity	Moment of inertia	Stress
m^{-1}	N-m	%	$N\text{-}m^2$	m^4	MPa
1.1856	66.37	0.6365	55.98	6.1180E-10	574.42
1.2250	67.44	0.6576	55.06	6.0171E-10	593.50
1.2673	68.60	0.6803	54.13	5.9160E-10	614.01
1.3065	69.60	0.7014	53.27	5.8221E-10	632.99
1.3065	69.60	0.7014	53.27	5.8221E-10	632.99
1.3103	69.69	0.7034	53.19	5.8128E-10	634.82
1.3540	70.65	0.7269	52.18	5.7027E-10	655.99
1.3984	71.53	0.7507	51.15	5.5901E-10	677.53
1.4330	72.19	0.7693	50.38	5.5056E-10	694.26
1.4330	72.19	0.7693	50.38	5.5056E-10	694.26
1.4436	72.39	0.7750	50.15	5.4804E-10	699.41
1.4893	73.27	0.7995	49.20	5.3768E-10	721.55
1.5352	74.16	0.8242	48.30	5.2790E-10	743.81
1.5637	74.70	0.8394	47.77	5.2210E-10	757.58
1.5637	74.70	0.8394	47.77	5.2210E-10	757.58
1.5811	75.03	0.8488	47.45	5.1863E-10	766.01
1.6267	75.88	0.8732	46.65	5.0983E-10	788.11
1.6724	76.74	0.8978	45.89	5.0151E-10	810.26
1.6950	77.18	0.9099	45.53	4.9761E-10	821.21
1.6950	77.18	0.9099	45.53	4.9761E-10	821.21
1.7185	77.63	0.9225	45.17	4.9369E-10	832.60
1.7649	78.51	0.9474	44.48	4.8617E-10	855.06
1.8107	79.29	0.9721	43.79	4.7857E-10	877.29
1.8264	79.52	0.9804	43.54	4.7586E-10	884.85
1.8264	79.52	0.9804	43.54	4.7586E-10	884.85
1.8556	79.90	0.9962	43.06	4.7057E-10	899.04
1.9004	80.39	1.0202	42.30	4.6233E-10	905.15
1.9469	80.94	1.0451	41.57	4.5435E-10	908.43
1.9565	81.07	1.0503	41.43	4.5284E-10	909.10
1.9565	81.07	1.0503	41.43	4.5284E-10	909.10
1.9964	81.66	1.0717	40.91	4.4706E-10	911.91
2.0458	82.47	1.0983	40.31	4.4057E-10	915.40
2.0902	83.16	1.1221	39.78	4.3480E-10	918.52
2.0922	83.18	1.1232	39.76	4.3451E-10	918.67
2.0922	83.18	1.1232	39.76	4.3451E-10	918.67
2.1266	83.59	1.1416	39.31	4.2959E-10	921.09
2.1622	84.01	1.1607	38.85	4.2462E-10	923.60
2.2023	84.66	1.1822	38.44	4.2012E-10	926.42
2.2023	84.66	1.1822	38.44	4.2012E-10	926.42
2.2072	84.75	1.1849	38.40	4.1964E-10	926.77
2.2646	85.90	1.2157	37.93	4.1455E-10	930.82
2.3160	86.76	1.2433	37.46	4.0942E-10	934.44
2.3372	86.70	1.2547	37.10	4.0545E-10	935.93
2.3372	86.70	1.2547	37.10	4.0545E-10	935.93

2.3.4 Applying Modified Equivalent Stress-Strain Approach to CIRFT Static Test Data

The developed MESA was applied to all the CIRFT static testing data. The required info to project global moment-curvature CIRFT data into local cladding surface stress-strain profile are listed in Table 5. The MESA results for HBR rods and LMK rod are shown in Figure 21 and for MOX and NA rods are shown in Figure 22, which show MRESA CIRFT test results has excellent agreement with that of PNNL and ORNL data obtained from tubing tensile test results.

Table 5. The yield strains and Young's modulus from PNNL Zry-4 and ORNL M5 cladding materials and the corresponding yield properties obtained from CIRFT testing data.

	Spec ID	Seg. ID	ε_y*	E_{C1}*/E_{C2}*	M_y	κ_y	σ_y	Oxide	Clad OD
			%	GPa	N·m	m^{-1}	MPa	μm	mm
HBR	S1	606C3C	1.0	91.50/13.31	81.59	1.860	900.5	70–100	10.76
HBR	S2	605D1E	1.0	91.50/13.31	84.08	1.860	906.7	40–70	10.76
HBR	Dcal	609C5	1.0	91.50/13.31	79.97	1.863	902.5	70–100	10.76
HBR	Scal	609C6	1.0	91.50/13.31	79.80	1.862	902.2	70–100	10.76
HBR	HR2	607D4A	1.0	91.50/13.31	71.84	1.857	907.2	40–44	10.76
LMK	LMK01	574D-A	1.0	91.50/13.31	73.96	1.751	914.0	<10	11.43
MOX	MOX01	MOX-A-11	0.70	96.65/3.479	36.92	1.461	676.6	<10	9.60
MOX	MOX03	MOX-A-13	0.70	96.65/3.479	33.87	1.461	676.7	<10	9.60
NA	NA3	651D3	0.70	96.65/3.479	35.25	1.459	676.0	<20	9.626

*Based on PNNL Zry-4 [21] and ORNL M5 [22] cladding tensile data.

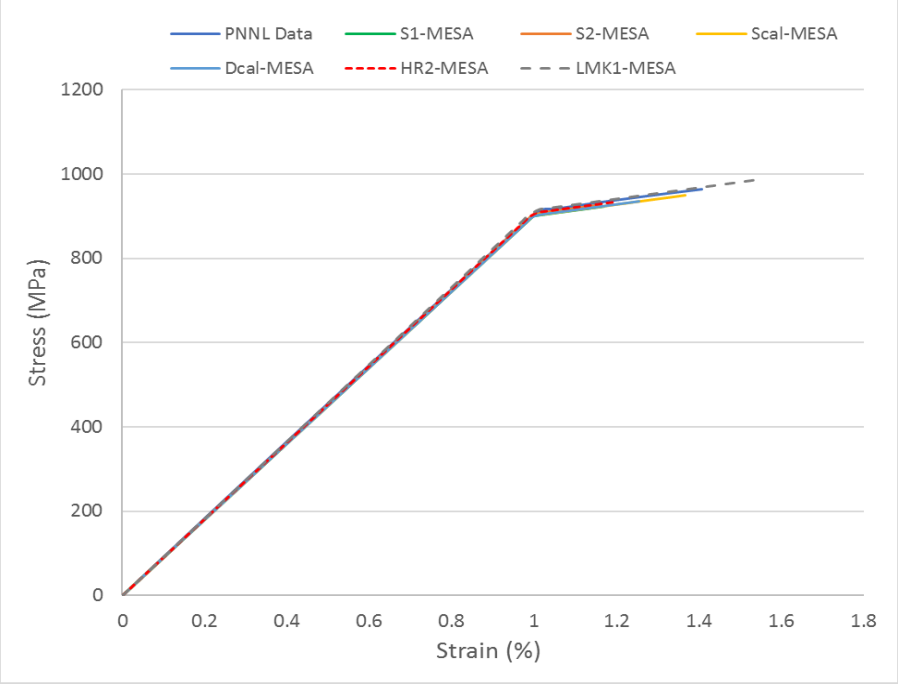

Figure 21. The comparison between PNNL Zry-4 data and cladding surface stress-strain profiles obtained from CIRFT static tests for HBR rods, incluidng HRT sample of HR2 data.

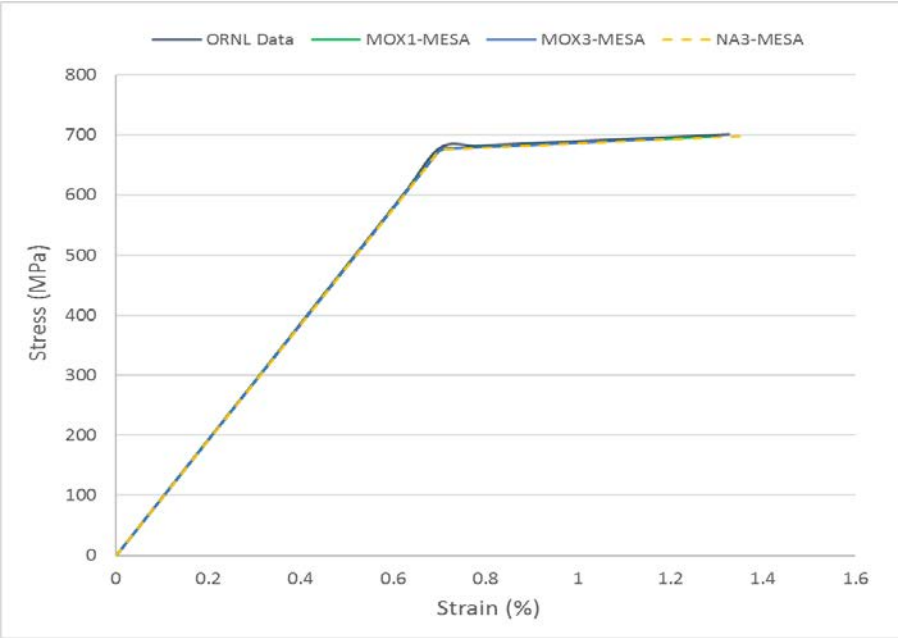

Figure 22. The comparison between ORNL M5 data and cladding surface stress-strain profiles obtained from CIRFT static tests for MOX and NA rods.

3. DYNAMIC CIRFT TEST DATA ANALYSIS

All the dynamic CIRFT test data were updated in this report period based on the correction factors developed for LVDTs' spacing adjustment and LVDTs' stem dynamic stability considerations; the newly developed MESA was also integrated into dynamic CIRFT test data for dynamic stress evaluations.

3.1 Data Analysis Results for Dynamic Tests

The data sets for each of the dynamic tests, including periodic quasistatic measurement data and online dynamic real-time monitoring data, were processed following the procedure described in Section 1.

For each test,

1) The variations of curvature range, moment range, flexural rigidity, curvature peak/valley, and moment peak/valley are presented whenever they are available.
2) The curvature and moment plots are given for the beginning data block of a test session when the load reaches the designated level. The results for two test sessions are presented: the first (tested to 1,000 cycles) and last sessions.
3) Finally, the data based on online monitoring are presented, including the variations of curvature range, moment range, flexural rigidity, curvature peak/valley, and moment peak/valley as a function of number of cycles or the cycles to failure.

For each cyclic test, several sets of measurements were obtained between test sessions. These measurements were made with small displacement amplitudes at 0.05 Hz. With this input, both moment and curvature varied or decreased with the accumulated number of cycles. The obtained rigidities were generally higher than those from monitoring data, and the degree of change was similar to the monitoring data.

The corrected curvature depends on the spacing correction applied. Generally, the correction observed for the curvature is not significant because of the small input. However, the signal-to-noise ratio is reduced at lower input levels. The amplitude of de-noised curvature was lower compared with the original noisy data. The summary table of dynamic data is self-explanatory and includes the following columns:

1) TN: test number
2) Spec: Specimen ID
3) ID: inner diameter of cladding
4) OD: outer diameter of cladding
5) Dia: diameter of pellet
6) Load: load amplitude at the loading point of U-frame
7) N: number of cycles accumulated or the cycles to failure
8) Fail: 1 as failure, and 0 as no failure
9) ma: mean of moment amplitude ($\Delta M/2$) based on de-noised monitoring data
10) ma_std: standard deviation of moment amplitude (4 in. or 101.60 mm loading arm) based on de-noised monitoring data
11) ka: mean of curvature amplitude ($\Delta\kappa/2$) based on corrected and de-noised monitoring data
12) ka_std: standard deviation of curvature amplitude based on corrected and de-noised monitoring data
13) km: mean of curvature extreme values based on corrected and de-noised monitoring data, $km = \max\{|\kappa_p|,|\kappa_v|\}$, where κ_p and κ_v are peak/valley values

14) km_std: standard deviation of curvature extremes based on corrected and de-noised monitoring data
15) R: mean of flexural rigidity
16) R_std: standard deviation of flexural rigidity
17) sa—: mean of equivalent stress amplitude ($\Delta\sigma/2$) based on de-noised monitoring data
18) sa_st: d – standard deviation of equivalent stress amplitude based on de-noised monitoring data
19) ea: mean of equivalent strain amplitude ($\Delta\varepsilon/2$) based on corrected and de-noised monitoring data
20) ea_std: standard deviation of equivalent strain amplitude based on corrected and de-noised monitoring data
21) em: mean of strain extreme values based on corrected and de-noised monitoring data, em = $\max\{|\varepsilon_p|,|\varepsilon_v|\}$, where ε_p and ε_v are peak/valley values
22) em_std: standard deviation of strain extremes based on corrected and de-noised monitoring data
23) Lg2: mean of half gauge length, Lg/2
24) Lg2_std: standard deviation of half gauge length
25) dh: mean of sensor spacing correction, Δh
26) dh_std: standard deviation of sensor spacing correction

3.2 CIRFT Evaluations of LMK Fuel Rods

A total of 16 specimens—LM1–LM3 and LM5–LM17—were tested in a hot cell. LM1 was used in the tuning and static test. The remaining 15 specimens were used in dynamic tests. The dynamic tests were conducted with a range of moment amplitudes from 7.11–30.48 Nm. A total of 13 specimens failed with fatigue lives from 10^4 to 4.7×10^6 cycles. LM12 and LM17 were cycled to more than 3.4×10^6 cycles without failure. LM12 was stopped at 7.6×10^6 cycles. LM17 was tested continuously at an increased amplitude of 30.48 Nm and failed at 1.3×10^4 cycles. Major results for the dynamic tests are summarized in Table 6.

The plots based on the mean values of major quantities can be found in Figure 23(a–d), where the circles represent the tests with failure, and the circles with arrows designate the tests with no failure. The results obtained from the follow-up tests for LM1 and LM17 are also included.

As expected, the fatigue life increased with decreasing amplitude, but the variation was not continuous. A discontinuity, or *knee point*, was observed near 7 Nm and 0.2 m^{-1} in the moment–N and curvature–N curves. For this SNF, these parameters correspond to 50 MPa of equivalent stress and 0.1% of equivalent strain. At the same time, curvature extreme values were generally higher than curvature amplitudes as expected, but the difference was small.

The flexural rigidity was mostly shown to be either quite flat or featuring a decreasing trend with the number of cycles. Several tests also suggested a tendency to increase with number of cycles, including LMK2, 8, and 14. Overall, the degree of variation of rigidity is limited. Meanwhile, no relation of rigidity to the number of cycles to failure can be seen.

The effective half gauge length was found to be limited with a range between 38–50 mm and to increase with increased amplitude of moment. On the other hand, the sensor spacing correction did not suggest any relation to the moment amplitude.

Table 6a. Dynamic test results for LMK SNF rods.

TN	Spec	Load N	N cycles	Fail	ma Nm	ma_std Nm	ka m^1	ka_std m^−1	km m^−1	km_std m^−1
1	LM1	250.000	9.40E + 03	Y	23.426	0.087	0.739	0.027	0.826	0.027
2	LM2	125.000	1.71E + 05	Y	11.468	0.090	0.218	0.006	0.226	0.008
3	LM3	100.000	4.92E + 05	Y	9.016	0.081	0.199	0.008	0.212	0.011
5	LM5	85.000	2.49E + 05	Y	7.570	0.074	0.135	0.008	0.168	0.013
6	LM6	75.000	1.79E + 06	Y	6.488	0.071	0.126	0.008	0.165	0.008
7	LM7	150.000	1.22E + 05	Y	13.930	0.085	0.285	0.005	0.297	0.009
8	LM8	75.000	4.70E + 06	Y	6.601	0.077	0.105	0.007	0.157	0.007
9	LM9	100.000	7.31E + 05	Y	9.058	0.077	0.177	0.004	0.185	0.007
10	LM10	200.000	5.20E + 04	Y	18.903	0.089	0.402	0.004	0.407	0.005
11	LM11	85.000	3.55E + 05	Y	7.657	0.111	0.133	0.007	0.159	0.010
12	LM12	70.000	7.58E + 06	N	6.141	0.087	0.169	0.014	0.185	0.021
13	LM13	250.000	2.10E + 04	Y	21.396	2.415	0.437	0.071	0.453	0.073
14	LM14	100.000	3.90E + 05	Y	9.048	0.082	0.162	0.008	0.187	0.010
15	LM15	100.000	4.41E + 05	Y	8.997	0.073	0.185	0.007	0.189	0.007
16	LM16	300.000	1.36E + 04	Y	28.560	0.168	0.536	0.008	0.557	0.014
17	LM17	85.000	3.37E + 06	N	7.459	0.374	0.167	0.011	0.174	0.013
18	LM17	300.000	1.31E + 04	Y	28.063	0.131	0.699	0.006	0.708	0.011

Table 6b. Dynamic test results for LMK SNF rods

TN	Spec	R Nm^2	R_std Nm^2	sa MPa	sa_std MPa	ea %	ea_std %	em %	em_std %	Lg2 mm	Lg2_std mm	dh mm	dh_std mm
1	LM1	31.73	0.809	385.67	0.667	0.422	0.015	0.472	0.015	43.766	0.767	0.279	0.182
2	LM2	52.59	0.891	113.86	0.691	0.124	0.004	0.128	0.005	44.250	0.634	−0.084	0.347
3	LM3	45.35	1.025	104.02	0.623	0.113	0.004	0.121	0.007	44.455	0.738	0.325	0.298
5	LM5	56.03	2.117	70.63	0.566	0.077	0.005	0.096	0.007	41.932	0.756	−1.436	0.577
6	LM6	51.50	2.287	65.92	0.548	0.072	0.005	0.093	0.005	40.157	0.749	−1.723	0.312
7	LM7	49.00	0.586	148.53	0.656	0.162	0.003	0.169	0.005	45.455	0.565	−0.426	0.190
8	LM8	62.89	2.504	54.79	0.590	0.060	0.004	0.089	0.004	42.342	0.890	2.568	0.338
9	LM9	51.07	0.736	92.46	0.590	0.101	0.003	0.106	0.004	43.120	0.698	0.206	0.215
10	LM10	47.03	0.336	209.74	0.684	0.229	0.002	0.231	0.003	46.986	0.528	0.355	0.173
11	LM11	57.85	2.009	69.34	0.856	0.075	0.004	0.090	0.006	41.396	0.757	−1.864	0.362
12	LM12	36.44	1.859	88.18	0.665	0.096	0.008	0.106	0.012	38.475	0.965	0.732	0.683
13	LM13	49.05	0.903	228.15	18.563	0.248	0.040	0.258	0.042	47.411	0.705	−0.138	0.143
14	LM14	55.68	1.768	84.75	0.632	0.093	0.005	0.107	0.006	44.092	0.781	−1.307	0.387
15	LM15	48.79	1.219	96.31	0.561	0.105	0.004	0.107	0.004	44.196	0.698	−0.148	0.585
16	LM16	53.26	0.480	279.94	1.295	0.305	0.005	0.317	0.008	50.296	0.440	−0.435	0.153
17	LM17	44.67	1.138	87.32	2.872	0.095	0.006	0.099	0.007	44.656	0.919	−0.849	0.338
18	LM17	40.14	0.252	365.12	1.004	0.398	0.003	0.403	0.006	47.420	0.331	1.211	0.092

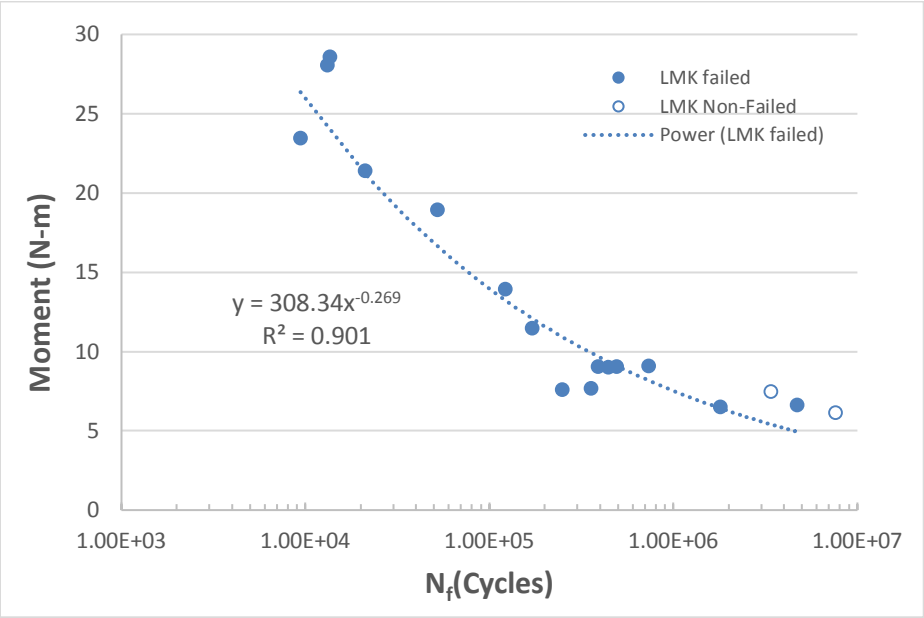
30
25
20
15
10
5
0
Moment (N-m)
LMK failed
LMK Non-Failed
Power (LMK failed)
y = 308.34x-0.269
R² = 0.901
1.00E+03
1.00E+04
1.00E+05
1.00E+06
1.00E+07
Nf(Cycles)

(a)

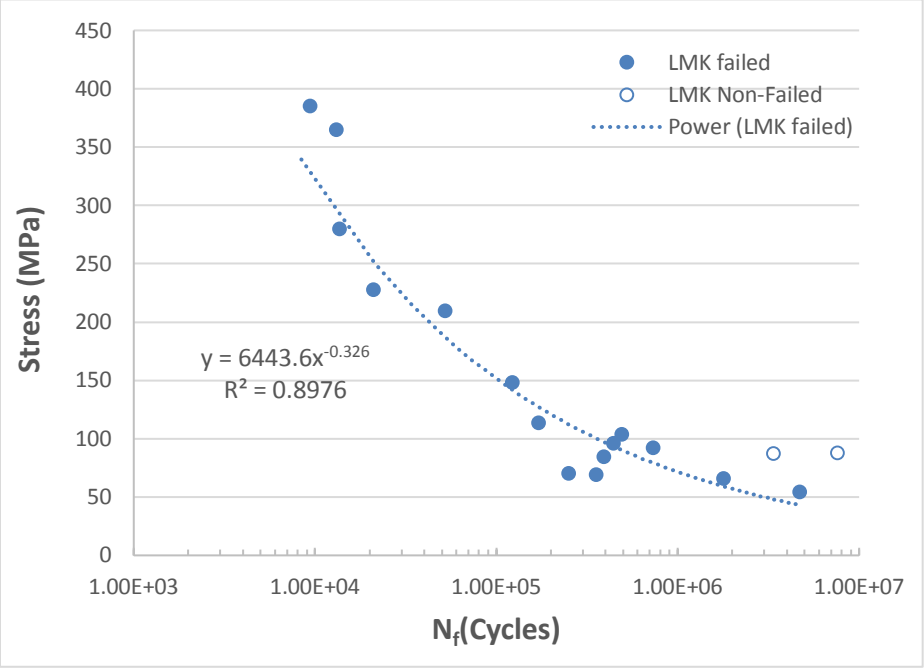
450
400
350
300
250
200
150
100
50
0
Stress (MPa)
LMK failed
LMK Non-Failed
Power (LMK failed)
y = 6443.6x-0.326
R² = 0.8976
1.00E+03
1.00E+04
1.00E+05
1.00E+06
1.00E+07
Nf(Cycles)

(b)

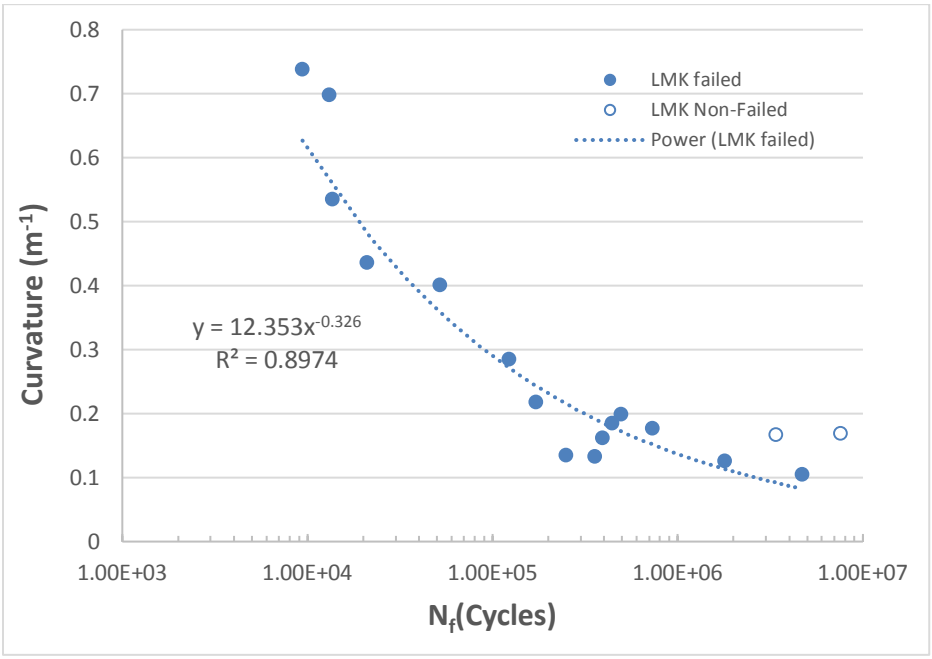

(c)

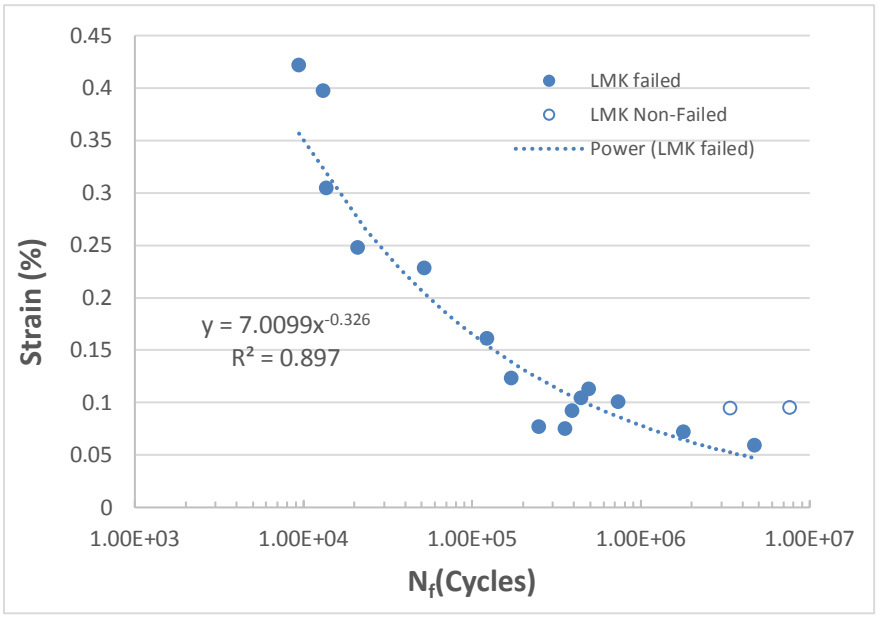

(d)

Figure 23. (a) Moment amplitude, (b) stress amplitude, (c) curvature amplitude/ maximum, and (d) strain amplitude/maximum as a function of cycles or cycles to failure.

3.3 CIRFT Evaluations of NA Fuel Rods

Six dynamic tests were conducted with applied amplitudes from 5.08 to 15.24 Nm; five specimens failed, and the fatigue life ranged from 1.26×10^4 to 4.27×10^5 cycles. One specimen (NA5) was cycled to 5.11×10^6 cycles without failure and stopped.

For each test, plots like those of LMK fuels are presented for NA fuel, including variations for curvature range, moment range, flexural rigidity, curvature peak/valley, and moment peak/valley values.

The results of the dynamic tests are summarized in Table 7. The column headings are the same as those specified in Section 3.1.

The plots based on the mean values of quantities can be found in Figure 24(a–d). There are knee points near 4 Nm and 0.05 m^{-1} in the moment–N_f, and curvature–N_f curve. However, the knee was not well defined because of the limited data points.

The rigidity variation was generally limited for a specified cyclic test, but abrupt variations were observed in several tests. However, the effective half gauge length was limited to a range between 40–49 mm, increasing with the amplitude of moment.

Table 7a. Dynamic test results for NA SNF rods.

TN	Spec	Load N	N cycles	Fail	ma Nm	ma_std Nm	ka m^1	ka_std m^−1	km m^−1	km_std m^−1
1	NA1	125.000	1.57E + 04	Y	11.001	0.053	0.420	0.007	0.440	0.013
2	NA2	100.000	2.20E + 04	Y	8.802	0.082	0.321	0.013	0.338	0.017
4	NA4	75.000	6.10E + 04	Y	6.331	0.083	0.181	0.009	0.209	0.010
5	NA5	50.000	5.11E + 06	N	3.982	0.068	0.117	0.014	0.132	0.014
6	NA6	50.000	4.27E + 05	Y	3.986	0.090	0.099	0.010	0.134	0.009
7	NA7	150.000	1.26E + 04	Y	13.540	0.542	0.500	0.039	0.516	0.026

Table 7b. Dynamic test results for NA SNF rods.

TN	Spec	R Nm^2	R_std Nm^2	sa Mpa	sa_std MPa	ea %	ea_std %	em %	em_std %	Lg2 mm	Lg2_std mm	dh mm	dh_std mm
1	NA1	26.20	0.268	194.49	0.650	0.202	0.003	0.212	0.006	46.055	0.469	−0.359	0.247
2	NA2	27.45	0.695	148.53	1.017	0.153	0.006	0.162	0.008	45.473	0.670	1.271	0.371
4	NA4	34.94	0.888	83.95	1.023	0.087	0.004	0.101	0.005	45.209	0.775	1.248	0.353
5	NA5	33.96	2.764	54.32	0.842	0.057	0.007	0.064	0.007	40.101	1.533	−0.148	0.770
6	NA6	40.17	2.801	45.96	1.113	0.048	0.005	0.064	0.004	43.153	0.968	1.745	0.404
7	NA7	27.07	1.174	231.71	6.690	0.242	0.019	0.248	0.013	49.444	1.317	0.163	0.345

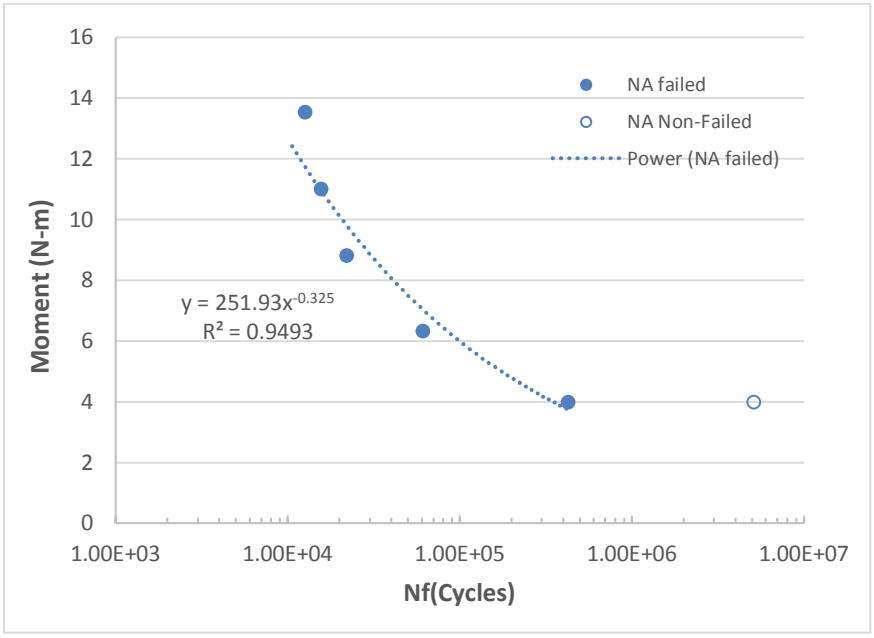
16
14
12
10
8
6
4
2
0
Moment (N-m)
1.00E+03
1.00E+04
1.00E+05
1.00E+06
1.00E+07
Nf(Cycles)
NA failed
NA Non-Failed
Power (NA failed)
y = 251.93x-0.325
R² = 0.9493

(a)

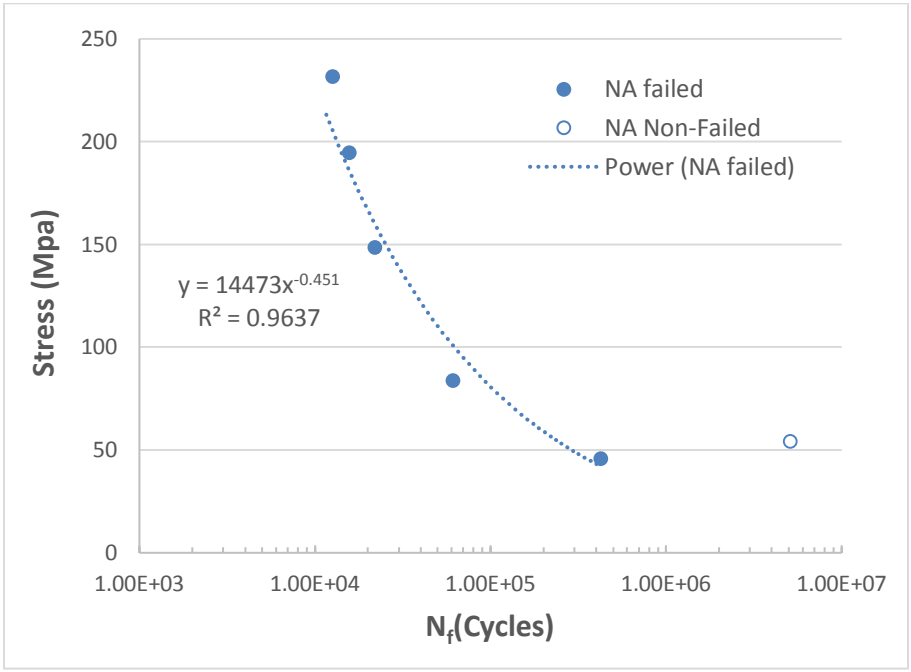
250
200
150
100
50
0
Stress (Mpa)
1.00E+03
1.00E+04
1.00E+05
1.00E+06
1.00E+07
Nf(Cycles)
NA failed
NA Non-Failed
Power (NA failed)
y = 14473x-0.451
R² = 0.9637

(b)

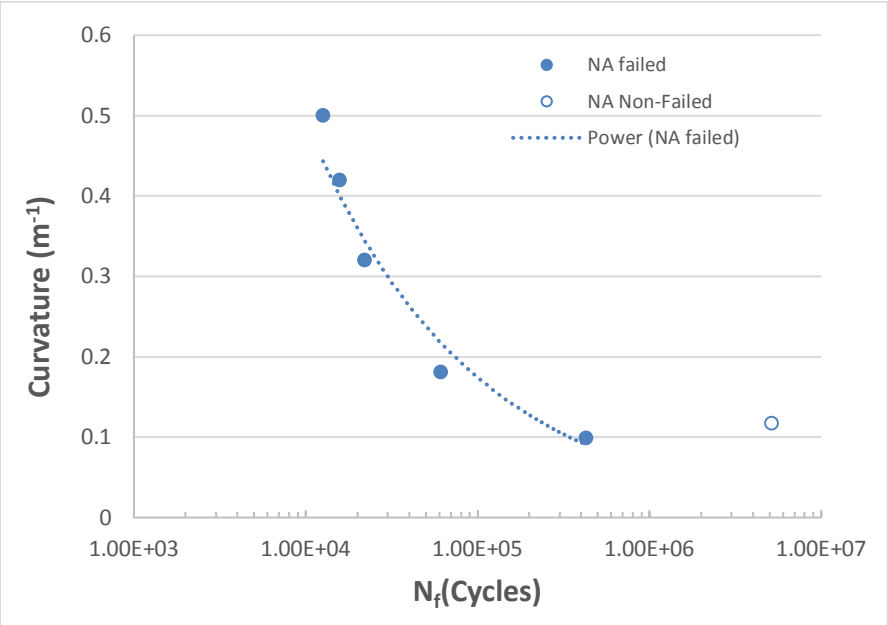

(c)

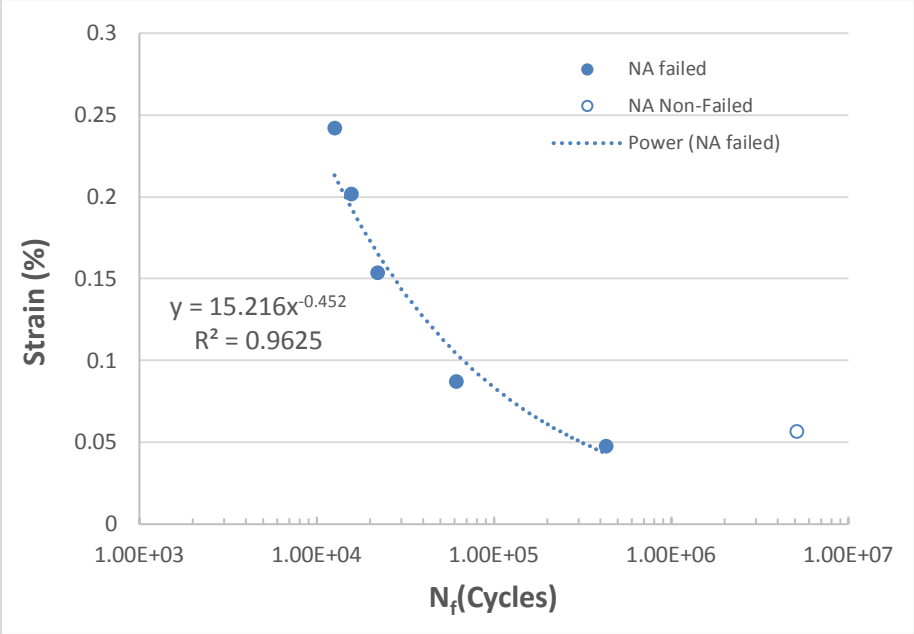

(d)

Figure 24. (a) Moment amplitude, (b) stress amplitude, (c) curvature amplitude/maximum, and (d) strain amplitude/maximum as a function of cycles or cycles to failure.

3.4 CIRFT Evaluations of MOX Fuel Rods

Twenty-three dynamic tests were completed with the applied amplitudes from 5.08–15.24 Nm, and all specimens failed. The fatigue life ranged from 3.66×10^3 to 2.51×10^6 cycles. Six tests were conducted on the specimens that had been pretreated by dropping them from a height of 12 in. with specimen laid horizontally, and the remaining seven tests used specimens that had been subjected to two cycles of thermal treatment for 10 h at 400°C.

The results for the dynamic tests of MOX fuel are summarized in Table 8. The column headings are the same as those specified in Sect. 3.1. The plots are based on the mean values of quantities and can be found in Figure 25 (a–d). In the moment–N_f curve, there is knee point near 4 Nm. However, the variation of fatigue life in curvature–N appeared to be continuous within the tested amplitude range.

The fatigue rigidity response depended on the moment amplitudes applied. At high levels (e.g., >10.2 Nm), the rigidity was either relatively stable, or it decreased with the accumulated number of cycles. At low levels, the rigidity increased during cyclic tests, but the fatigue life of MOX fuel increased with the increasing initial rigidity.

Conversely, the effective half gauge length limited to a range between 40–52 mm, increasing with increased amplitude of moment.

Table 8a. Dynamic test results for MOX SNF rods.

TN	Spec	Type	Load N	N cycles	Fail	ma Nm	ma_std Nm	ka m^1	ka_std m^-1	km m^-1	km_std m^-1
2	MOX2	A	100	3.70E + 04	Y	8.480	0.103	0.349	0.010	0.358	0.012
4	MOX4	A	50	2.15E + 06	Y	3.900	0.075	0.108	0.016	0.121	0.017
5	MOX5	A	60	4.49E + 05	Y	4.794	0.061	0.147	0.009	0.153	0.010
6	MOX6	A	50	5.42E + 05	Y	3.830	0.054	0.139	0.008	0.143	0.010
7	MOX7	A	150	1.55E + 04	Y	13.857	0.127	0.516	0.008	0.525	0.009
8	MOX8	A	125	1.29E + 04	Y	11.036	0.104	0.444	0.009	0.481	0.013
9	MOX9	A	75	8.98E + 04	Y	6.294	0.084	0.262	0.009	0.289	0.015
10	MOX10	A	100	3.85E + 04	Y	8.729	0.068	0.310	0.016	0.326	0.017
11	MOX11	A	100	4.23E + 04	Y	8.662	0.047	0.308	0.008	0.340	0.011
12	MOX12	A	100	4.23E + 04	Y	8.711	0.067	0.340	0.005	0.360	0.010
13	MOX13	D	100	2.70E + 04	Y	8.725	0.059	0.369	0.007	0.382	0.011
14	MOX14	D	75	8.72E + 04	Y	6.190	0.091	0.548	0.172	1.194	1.160
15	MOX15	D	50	4.65E + 06	N	3.842	0.074	0.151	0.028	0.177	0.011
16	MOX16	D	150	3.66E + 03	Y	13.209	1.656	0.809	0.273	0.826	0.345
17	MOX17	D	125	1.16E + 04	Y	11.104	0.951	0.574	0.663	0.630	0.960
18	MOX15	D	100	1.95E + 04	Y	8.474	0.065	0.360	0.005	0.365	0.008
19	TH1	H	100	5.70E + 04	Y	8.770	0.065	0.441	0.007	0.462	0.009
20	TH2	H	75	3.75E + 06	N	6.234	0.107	0.289	0.009	0.312	0.013
21	TH3	H	125	1.51E + 04	Y	10.573	0.289	0.571	0.029	0.600	0.033
22	TH4	H	75	2.51E + 06	Y	6.284	0.150	0.327	0.025	0.359	0.027
23	TH5	H	125	2.76E + 04	Y	11.190	0.069	0.673	0.008	0.680	0.011
24	TH6	H	150	1.25E + 04	Y	13.391	0.157	0.666	0.014	0.682	0.018
25	TH2	H	125	5.73E + 04	Y	11.029	0.135	0.550	0.012	0.556	0.013

A= as-received sample
D = sample with 12-in. drop
H = sample subjected to two cycles of thermal treatment for 10 h at 400°C

Table 8b. Dynamic test results for MOX SNF rods.

TN	Spec	R	R_std	sa	sa_std	ea	ea_std	em	em_std	Lg2	Lg2_std	dh	dh_std
		Nm^2	Nm^2	Mpa	MPa	%	%	%	%	mm	mm	mm	mm
2	MOX2	24.33	0.533	161.34	1.274	0.167	0.005	0.172	0.006	43.811	0.621	1.243	0.291
4	MOX4	36.03	3.703	50.11	0.932	0.052	0.008	0.058	0.008	40.575	2.133	−1.512	0.927
5	MOX5	32.66	1.235	67.95	0.758	0.071	0.004	0.073	0.005	43.766	1.027	−1.178	0.684
6	MOX6	27.64	1.021	64.16	0.662	0.066	0.004	0.069	0.005	43.751	0.867	0.059	0.395
7	MOX7	26.87	0.316	238.78	1.569	0.248	0.004	0.252	0.004	48.523	0.454	0.409	0.129
8	MOX8	24.83	0.282	205.76	1.282	0.213	0.004	0.231	0.006	49.223	0.484	0.441	0.144
9	MOX9	24.06	0.470	121.10	1.041	0.125	0.004	0.139	0.007	45.835	0.536	−0.505	0.190
10	MOX10	28.16	0.855	143.50	0.840	0.148	0.008	0.156	0.008	49.626	1.075	−0.428	0.276
11	MOX11	28.17	0.534	142.36	0.585	0.148	0.004	0.163	0.005	52.390	0.622	−1.036	0.260
12	MOX12	25.60	0.242	157.54	0.825	0.163	0.002	0.173	0.005	48.820	0.550	−0.678	0.182
13	MOX13	23.64	0.268	170.83	0.734	0.177	0.003	0.184	0.005	47.339	0.524	−0.040	0.190
14	MOX14	11.30	2.432	253.59	1.122	0.263	0.083	0.573	0.557	27.459	7.996	1.240	2.671
15	MOX15	25.46	3.764	69.85	0.917	0.072	0.013	0.085	0.005	43.138	3.120	0.741	1.512
15	MOX15	22.66	0.547	78.48	0.999	0.080	0.004	0.084	0.006	41.513	0.755	0.275	0.315
16	MOX16	16.34	1.700	374.31	20.479	0.388	0.131	0.396	0.165	48.167	0.841	0.188	0.275
17	MOX17	19.34	2.371	265.74	11.752	0.276	0.318	0.303	0.461	46.586	2.074	0.081	0.390
18	MOX15	23.54	0.165	166.65	0.804	0.173	0.002	0.175	0.004	47.594	0.516	0.170	0.192
19	TH1	19.88	0.186	204.24	0.800	0.212	0.004	0.222	0.004	49.023	0.443	0.738	0.145
20	TH2	21.54	0.350	134.01	1.322	0.139	0.004	0.149	0.006	48.349	0.802	−0.743	0.224
21	TH3	18.53	0.713	264.22	3.569	0.274	0.014	0.288	0.016	47.431	0.867	0.337	0.247
22	TH4	19.21	0.862	151.47	1.856	0.157	0.012	0.172	0.013	48.093	0.793	−0.217	0.790
23	TH5	16.62	0.151	311.67	0.847	0.323	0.004	0.326	0.005	47.979	0.372	0.297	0.136
24	TH6	20.11	0.394	308.25	1.942	0.320	0.007	0.327	0.008	49.765	0.385	−0.563	0.134
25	TH2	20.04	0.137	254.73	1.674	0.264	0.006	0.267	0.006	50.304	0.464	−0.366	0.109

The flexural rigidity of the rod specimens that were either dropped or heat-treated was lower than the as-received specimens. In most cases, the online monitoring generally demonstrated a steady or continuous variation in curvature during cyclic testing, depending on the moment amplitude and material condition. MOX14 was the exception, where a discontinuous rigidity variation was observed. Such a discontinuous response was associated with the asymmetrical curvature increase of the specimen, and an abrupt increase was seen near 10^4 cycles, as the specimen was approaching failure. For MOX15, a substantial negative shift in κ and a reduction in the κ range were observed after a test restart at around 3.3×10^6 cycles.

Plots based on the mean values of quantities are given in Figure 25 (a–d), where MOX_A represents the as-received specimens, MOX_D represents those subjected to a drop from 12 inches, and MOX_H represents those that were thermal annealed. Fatigue life was shown to be affected by the condition of specimens. The 12 in. drop seemingly reduces the fatigue life of SNF rods. Conversely, heat-treated extends fatigue life, which can be seen from the two tests under 7.62 Nm (75 N load), as shown in Figure 25(a).

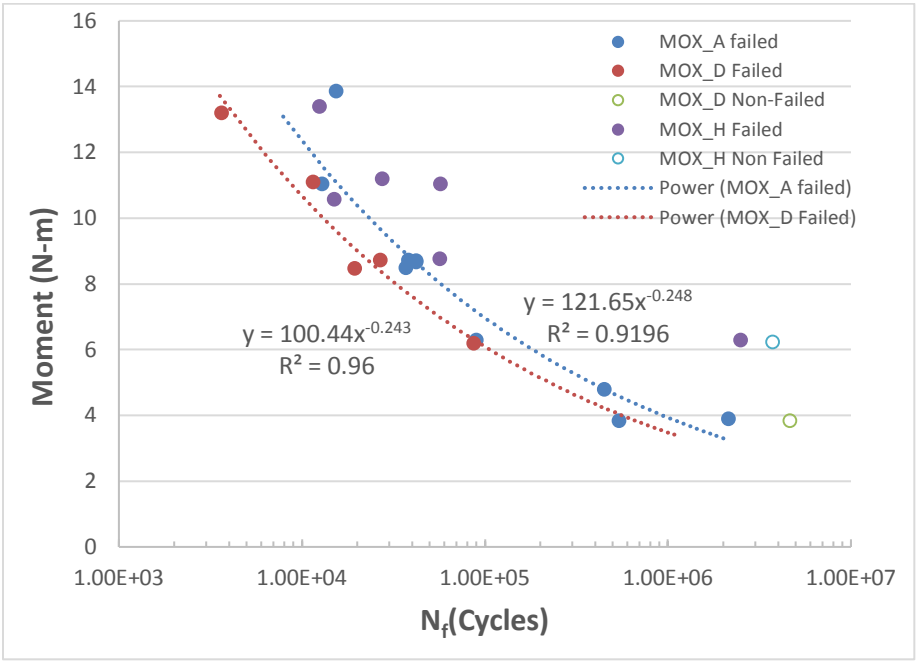
Moment (N-m)
16
14
12
10
8
6
4
2
0
1.00E+03
1.00E+04
1.00E+05
1.00E+06
1.00E+07
N_f(Cycles)
MOX_A failed
MOX_D Failed
MOX_D Non-Failed
MOX_H Failed
MOX_H Non Failed
Power (MOX_A failed)
Power (MOX_D Failed)
y = 121.65x^-0.248
R² = 0.9196
y = 100.44x^-0.243
R² = 0.96

(a)

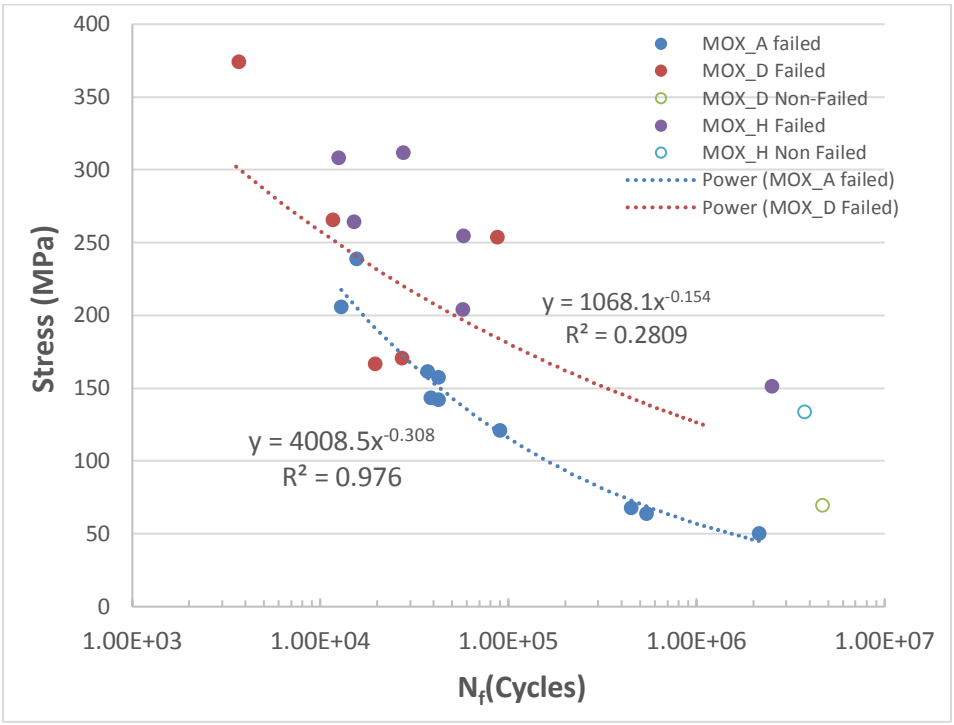
Stress (MPa)
400
350
300
250
200
150
100
50
0
1.00E+03
1.00E+04
1.00E+05
1.00E+06
1.00E+07
N_f(Cycles)
MOX_A failed
MOX_D Failed
MOX_D Non-Failed
MOX_H Failed
MOX_H Non Failed
Power (MOX_A failed)
Power (MOX_D Failed)
y = 1068.1x^-0.154
R² = 0.2809
y = 4008.5x^-0.308
R² = 0.976

(b)

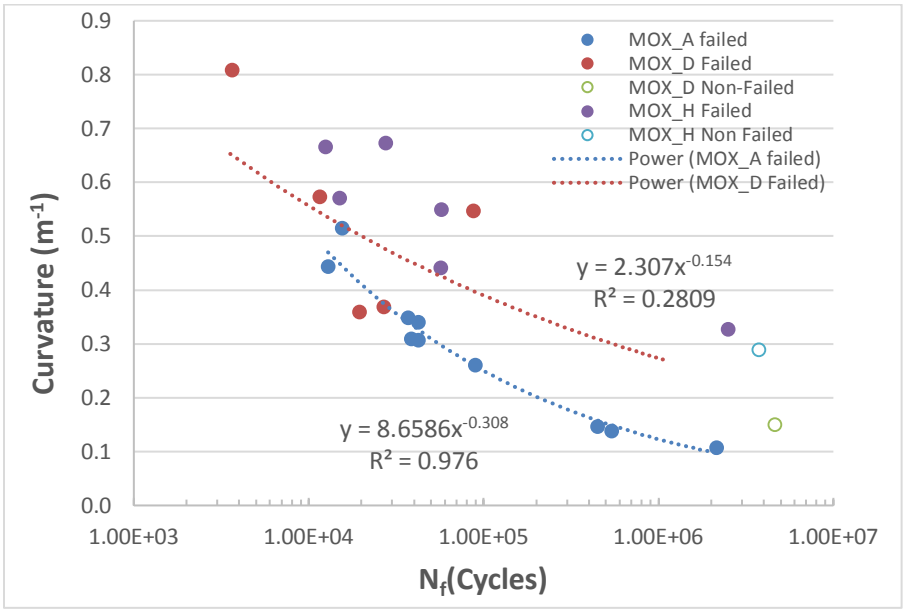

(c)

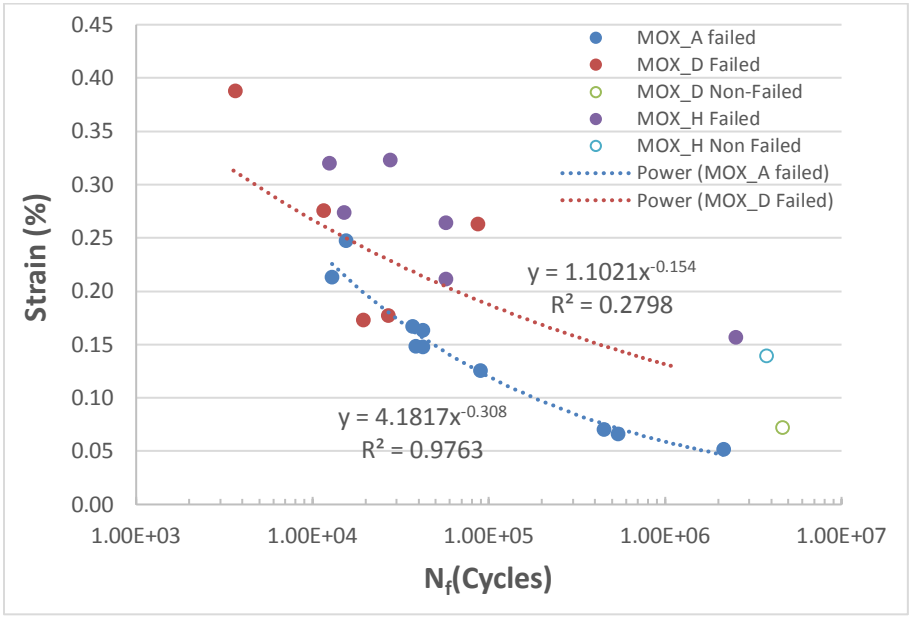

(d)

Figure 25. (a) Moment amplitude, (b) stress amplitude, (c) curvature amplitude/maximum, and (d) strain amplitude/maximum as a function of cycles or cycles to failure (MOX_A: as-received; MOX_D: 12 in. drop; MOX_H: heat treated).

3.5 CIRFT Evaluations of HBR Fuel Rods

The vibration reliability study on HBU HBR rods with Zry-4 cladding was jointly funded by US Nuclear Regulatory Commission and the DOE Used Fuel Disposition Campaign (UFDC) The study is documented in NUREG/CR-7198/R1, *Mechanical Fatigue Testing of High-Burnup Fuel for Transportation Applications*. The plots of HBR fuels are like those of LMK fuels, including the variations of curvature range, moment range, flexural rigidity, curvature peak/valley, and moment peak/valley values. The flexural rigidity of the rod specimens treated by hydride reorientation was shown to be much lower than as-received specimens under equivalent amplitude. For example, under the same loading amplitude of 100 N, the rigidity of the radial hydride treatment (RHT) specimen (HR3) was only about 57% of the as-received specimen (DL3). The variation of rigidity during a cyclic test was continuous. In HR3, a sudden drop was observed before. The dynamic testing results for as-irradiated and hydride reorientation (HR)-treated HBR rods are summarized in Table 9.

Table 9a. Dynamic test results for HBR SNF rods.

TN	Spec	Load in.	N cycles	Fail	ma Nm	ma_std Nm	ka m^1	ka_std m^−1	km m^−1	km_std m^−1
1	Demo1	300	3.96E+03	Y	28.504	0.131	0.944	0.008	1.123	0.024
2	S3	250	2.50E+04	Y	24.068	0.067	0.439	0.006	0.444	0.008
5	S1	300	4.60E+03	Y	28.493	0.087	0.674	0.008	0.730	0.017
6	S2	300	7.20E+03	Y	28.314	0.088	0.654	0.015	0.746	0.024
7	Dcal	300	9.60E+03	Y	28.579	0.098	0.754	0.026	0.862	0.041
9	DL1	150	1.10E+05	Y	14.107	0.069	0.215	0.007	0.240	0.01
10	DL2	50	6.40E+06	N	4.207	0.083	0.046	0.007	0.066	0.009
11	DL2H	350	1.80E+03	Y	34.087	0.077	0.747	0.006	0.765	0.013
12	DL3	100	1.00E+06	Y	9.17	0.085	0.125	0.012	0.171	0.012
13	DM2	90	2.30E+06	Y	8.201	0.070	0.114	0.007	0.122	0.009
14	DM1	75	1.10E+07	N	6.726	0.081	0.089	0.01	0.121	0.012
15	DH1	125	2.50E+05	Y	11.624	0.069	0.205	0.005	0.218	0.007
16	DH2	200	6.50E+04	Y	18.923	0.108	0.351	0.006	0.370	0.011
17	DM3	87.5	1.28E+07	N	7.747	0.134	0.105	0.018	0.117	0.035
18	DH3	350	7.10E+03	Y	33.666	0.127	0.581	0.182	0.636	0.233
19	S5	125	1.80E+05	Y	11.552	0.090	0.174	0.019	0.213	0.02
20	R1	300	5.50E+03	Y	29.021	0.074	0.469	0.043	0.563	0.035
21	R2	110	3.86E+05	Y	9.986	0.078	0.144	0.012	0.171	0.012
22	R3	135	1.29E+05	Y	12.551	0.072	0.152	0.007	0.199	0.008
23	R4	87.5	2.74E+05	Y	7.842	0.076	0.112	0.01	0.135	0.012
24	R5	75	2.24E+07	N	6.639	0.087	0.087	0.02	0.125	0.021
25	HR1[a]	150	4.19E + 04	Y	15.152	0.549	0.517	0.016	0.527	0.019
26	HR2[a]	160	9.47E + 03	Y	14.702	0.806	0.478	0.121	0.511	0.205
27	HR3[a]	100	2.44E + 05	Y	8.982	0.066	0.267	0.005	0.291	0.009
28	HR4[b]	160	5.47E + 04	Y	14.759	0.089	0.394	0.008	0.421	0.009

[a] = HR- treated sample with 5 cycles of 400°C holding for 3 hours per cycle and 140MPa hoop stress pressurization
[b] = thermal treatment sample with 400°C

Table 9b. Dynamic test results for HBR SNF rods.

TN	Spec	R Nm^2	R_std Nm^2	Sa MPa	sa_std MPa	ea %	ea_std %	em %	em_std %	Lg2 mm	Lg2_std mm	dh mm	dh_std mm
1	Demo1	30.20	0.159	455.55	1.117	0.508	0.004	0.605	0.013	44.461	0.287	0.637	0.094
2	S3	54.86	0.47	213.75	0.576	0.235	0.003	0.239	0.005	48.761	0.498	0.276	0.335
5	S1	42.27	0.369	326.57	0.745	0.362	0.004	0.392	0.009	50.152	0.413	0.017	0.128
6	S2	43.32	0.647	318.43	0.751	0.351	0.008	0.401	0.013	50.027	0.443	0.042	0.176
7	Dcal	37.88	0.81	365.50	0.836	0.405	0.014	0.463	0.022	48.211	0.532	0.46	0.146
9	DL1	65.66	1.388	104.09	0.574	0.116	0.004	0.130	0.005	45.929	0.678	−0.443	0.693
10	DL2	91.62	10.039	22.25	0.702	0.025	0.004	0.036	0.005	34.776	2.113	−0.007	1.723
11	DL2H	45.63	0.23	361.93	0.65	0.403	0.003	0.412	0.007	46.213	0.343	0.906	0.118
12	DL3	73.57	5.173	60.39	0.725	0.067	0.007	0.092	0.007	41.048	1.048	−1.573	0.847
13	DM2	71.95	3.149	55.54	0.595	0.062	0.004	0.066	0.005	41.18	0.834	−0.736	0.461
14	DM1	75.25	6.197	43.55	0.696	0.048	0.005	0.065	0.007	39.505	0.965	−0.506	1.255
15	DH1	56.70	0.843	99.32	0.593	0.110	0.003	0.117	0.004	43.153	0.679	0.272	0.315
16	DH2	53.92	0.718	170.04	0.917	0.189	0.003	0.199	0.006	46.474	0.507	−0.285	0.196
17	DM3	73.81	9.551	50.85	1.151	0.057	0.009	0.063	0.019	43.127	2.378	0.762	1.254
18	DH3	57.91	12.993	281.67	1.087	0.312	0.098	0.342	0.125	47.827	3.03	2.341	0.865
19	S5	66.45	5.258	84.22	0.767	0.093	0.01	0.115	0.011	44.982	1.264	1.97	0.431
20	R1	61.87	4.029	227.25	0.618	0.254	0.023	0.306	0.019	51.603	1.61	2.242	0.723
21	R2	69.19	4.15	69.92	0.652	0.078	0.007	0.093	0.007	43.13	0.99	−1.099	0.451
22	R3	82.74	2.609	73.22	0.611	0.081	0.004	0.107	0.004	47.963	1.003	2.524	0.305
23	R4	69.81	4.492	54.22	0.648	0.061	0.006	0.073	0.006	40.344	0.962	−1.434	0.537
24	R5	76.38	10.704	41.95	0.735	0.047	0.011	0.067	0.011	38.842	1.821	1.01	1.402
25	HR1	29.329	0.775	207.06	4.666	0.278	0.009	0.284	0.010	44.733	0.565	1.329	0.197
26	HR2	31.567	3.256	191.44	6.848	0.257	0.065	0.275	0.110	50.657	1.593	−0.174	0.372
27	HR3	33.659	0.602	106.94	0.560	0.144	0.003	0.157	0.005	43.368	0.643	−1.649	0.252
28	HR4	37.497	0.593	157.80	0.755	0.212	0.004	0.227	0.005	45.977	0.578	1.206	0.201

The plots based on the mean values of quantities are given in Figure 26(a–d), where HBR represents the as-received specimen, and HBR_HR represents the specimen after RHT. It has been shown that the RHT reduces the fatigue life of SNF rods, which can be seen from the tests around 15 Nm. A fatigue life reduction was also observed for HR2, as indicated by the arrow. Such reduction obviously resulted from the large-deformation static loading before the dynamic cyclic loading.

Optical microscopy was conducted on the fracture surfaces of the selected test specimens. Among the seven specimens examined, at least five failures were determined to be dominated by the PPIs. Most of the SNF rod failures initiated and propagated through the pellet-pellet clad interface region in a typical tensile failure mode except for the HR1 tested sample. The HR1 fractured sample showed crack initiated at the PPI, but the crack propagation was in a mixed-mode (tensile + shear) failure mechanism. The postmortem examination of the HR1 fractured sample also indicated that a large area of the pellet-cladding bond was disrupted, as shown in Figure 27.

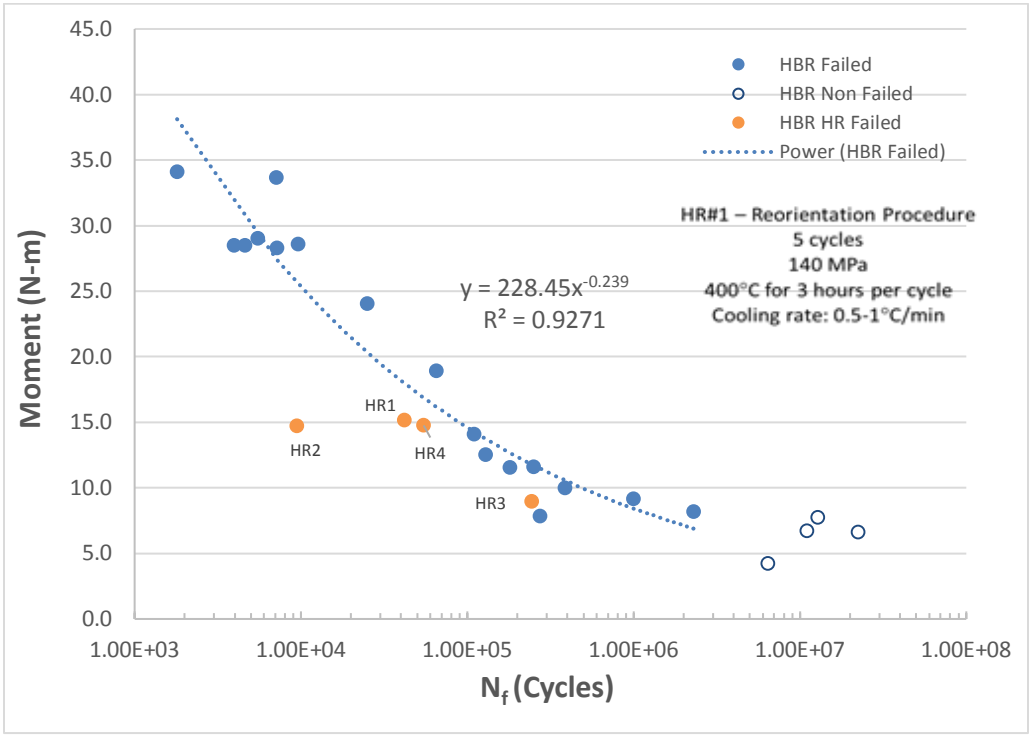
Moment (N-m)
45.0
40.0
35.0
30.0
25.0
20.0
15.0
10.0
5.0
0.0
1.00E+03
1.00E+04
1.00E+05
1.00E+06
1.00E+07
1.00E+08
N_f (Cycles)
HBR Failed
HBR Non Failed
HBR HR Failed
Power (HBR Failed)
HR#1 – Reorientation Procedure
5 cycles
140 MPa
400°C for 3 hours per cycle
Cooling rate: 0.5-1°C/min
$y = 228.45x^{-0.239}$
$R^2 = 0.9271$
HR1
HR2
HR3
HR4

(a)

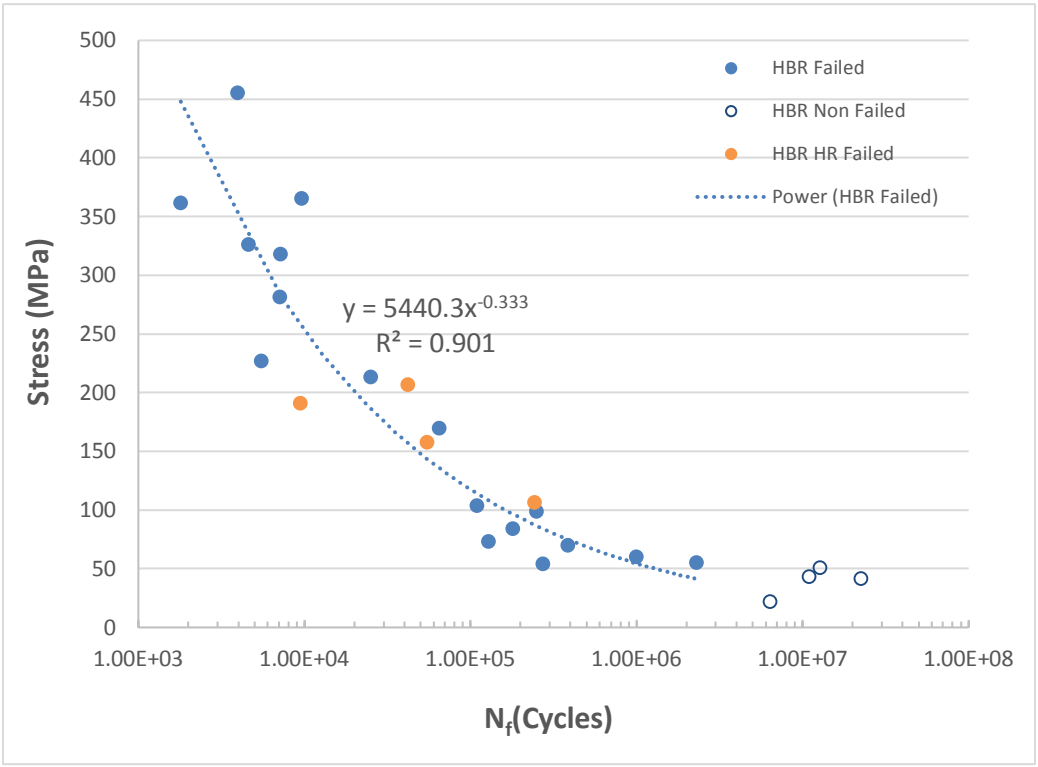
Stress (MPa)
500
450
400
350
300
250
200
150
100
50
0
1.00E+03
1.00E+04
1.00E+05
1.00E+06
1.00E+07
1.00E+08
N_f(Cycles)
HBR Failed
HBR Non Failed
HBR HR Failed
Power (HBR Failed)
$y = 5440.3x^{-0.333}$
$R^2 = 0.901$

(b)

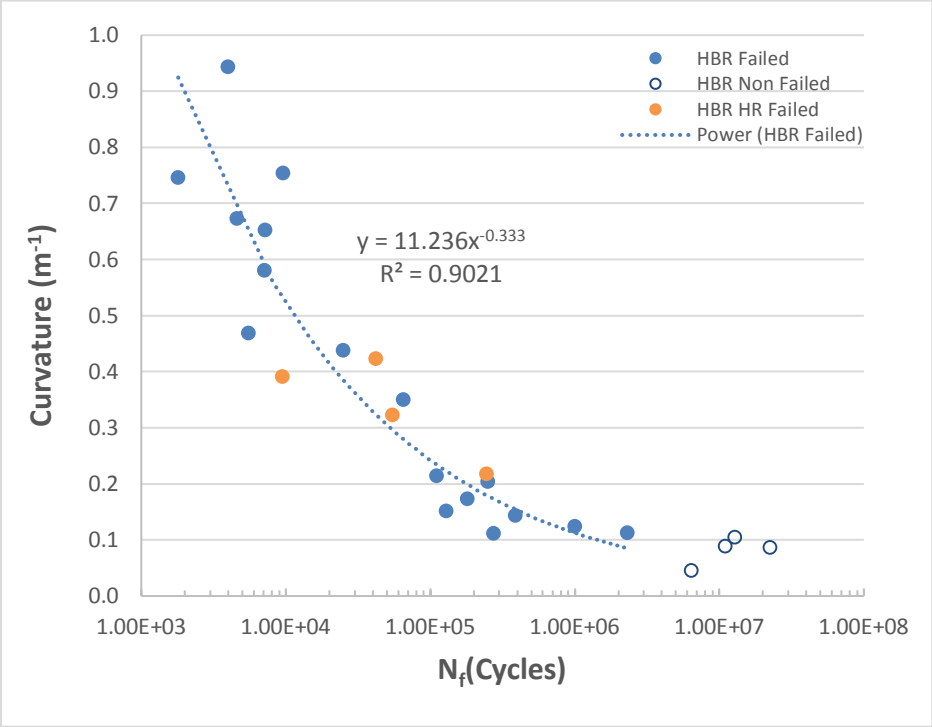

(c)

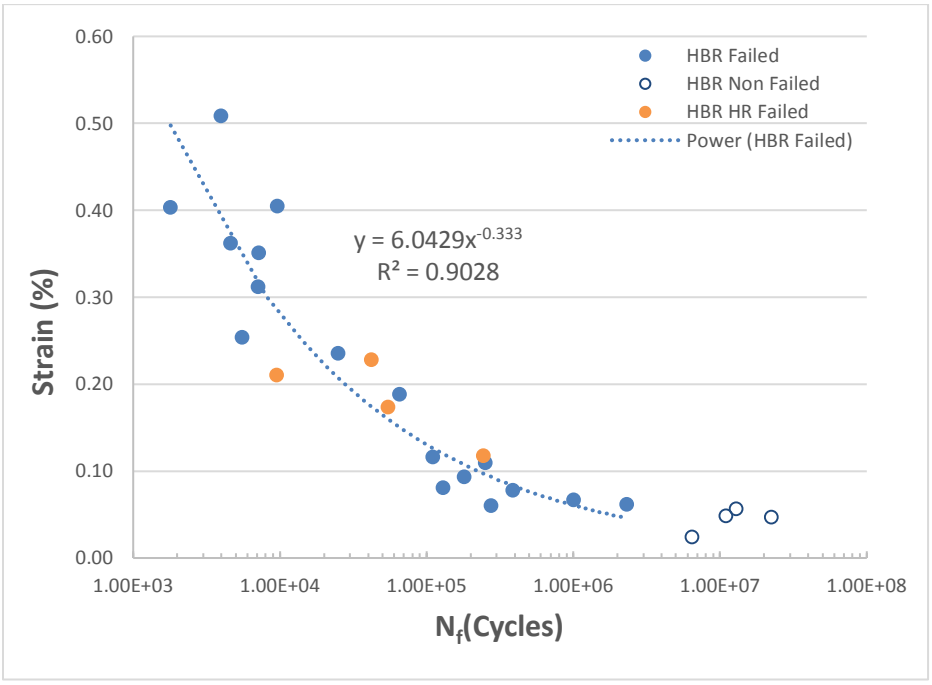

(d)

Figure 26. (a) Moment amplitude, (b) stress amplitude, (c) curvature amplitude, and (d) strain amplitude rigidity as a function of cycles or cycles to failure.

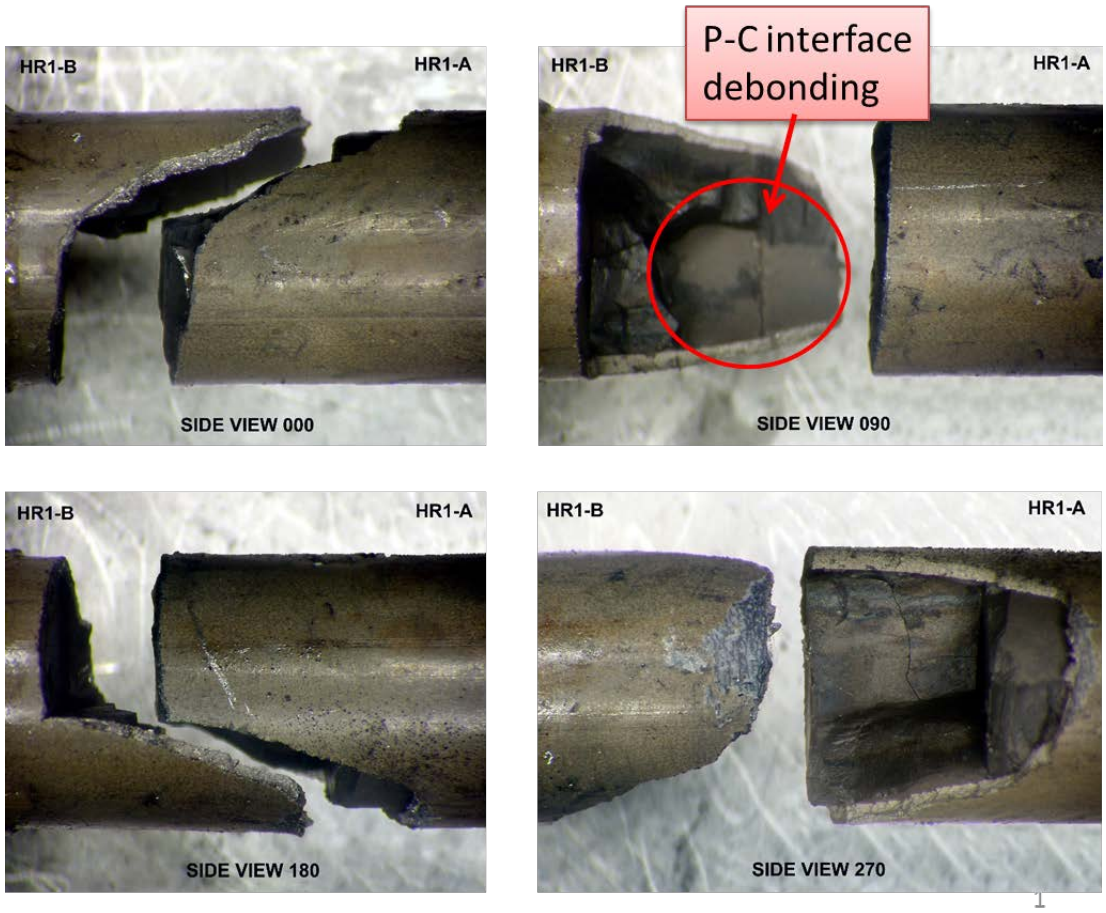

Figure 27. HR fractured sample HR1 revealed mixed-mode failure mechanisms [23].

3.5.1 Cladding Oxide Effect Study

HBR CIRFT test data and the associated oxide thickness are shown in Table 10.

Table 10. HBR SNF CIRFT data with the associated tested rod's oxide thickness.

Spec label ID	Moment amplitude	Number of cycles	Flexural rigidity	κ_a	s_a	ε_a	Oxide thickness [1]	Hydrogen of span [20,21]
Unit	**N·m**	**#**	**N-m²**	**m^{-1}**	**MPa**	**%**	**µm**	**wppm**
As-irradiated CIRFT data								
DM3	7.74	>1.28E+07	72.3	0.107	50.85	0.057	70–100	550–750
R4	7.84	2.74E+05	70.0	0.112	54.22	0.06	100–110	750–800
DM2	8.20	2.30E+06	71.9	0.114	55.54	0.061	40–70	360–550
DL3	9.17	1.00E+06	73.4	0.125	60.39	0.067	70–100	550–750
R2	9.99	3.86E+05	69.4	0.144	69.92	0.078	70–100	550–750
S5	11.55	1.80E+05	66.4	0.174	84.22	0.094	70–100	550–750
DH1	11.62	2.50E+05	56.7	0.205	99.32	0.11	70–100	550–750
R3	12.55	1.29E+05	83.1	0.151	73.22	0.081	100–110	750–800
DL1	14.11	1.10E+05	65.6	0.215	104.09	0.117	70–100	550–750
DH2	18.92	6.50E+04	53.9	0.351	170.04	0.189	70–100	550–750
S3	24.07	2.50E+04	54.8	0.439	213.75	0.236	40–70	360–550
R1	29.02	5.50E+03	61.9	0.469	227.25	0.254	70–100	550–750
DH3	33.67	7.10E+03	58.5	0.576	281.67	0.31	70–100	550–750
HR CIRFT data								
HR1	15.15	4.19E+04	35.7	0.424	207.06	0.228	40–44	360–400
HR3	8.98	2.44E+05	41.0	0.219	106.94	0.118	40–44	360–400
HR4	14.76	5.47E+04	45.7	0.323	157.80	0.174	40–44	360–400

With the similar loading amplitude, analysis of the CIRFT data with high oxide thickness suggests reduced fatigue life compared to CIRFT data with lower oxide thickness. For instance, the D8 sample with 70–100 µm oxide thickness and the D14 sample with 100–110 µm oxide thickness had similar loading amplitudes; the D8 sample had a much longer fatigue life at >12M cycles compared to the D14 sample at 2.74E5 cycles. The CIRFT data are shown with distinct labels for four oxide thickness ranges in Figure 28(a-d). Two trend curves shown in Figure 28(a) and (d) indicate that SNF rods with higher oxide thickness or higher hydrogen contents had lower fatigue life.

The plots of as-irradiated baseline data for moment amplitude and strain amplitude input from HBR baseline data show a self-consistent trend: as-irradiated CIRFT data with higher oxide thickness showed less fatigue life, while for HR data, a different trend was observed from moment amplitude and strain amplitude input plots. In the moment amplitude plot, HR data showed reduced fatigue life below the mean trend curve of 70–100 µm oxide thickness, while as in the strain amplitude, plot HR data showed increased fatigue life above the mean trend curve. The HR samples had the lowest oxide thickness, as well as the lowest flexural rigidity, as shown in Figure 28(c–d). Thus, HR data would be expected to trend above the mean fatigue strength trend curve of 70–100 µm oxide thickness in the plots. Apparently, this is the case for the strain vs. failure cycles trend, but not for the moment vs. failure cycles trend. Furthermore, HR data have the lowest flexural rigidity, so under similar loading conditions, it would have the highest strain response compared to the as-irradiated HBR data. The low flexural rigidity is the root

cause of the HR data's self-inconsistent trend, where the flexural rigidity reduction of HR data was the result of heat treatment.

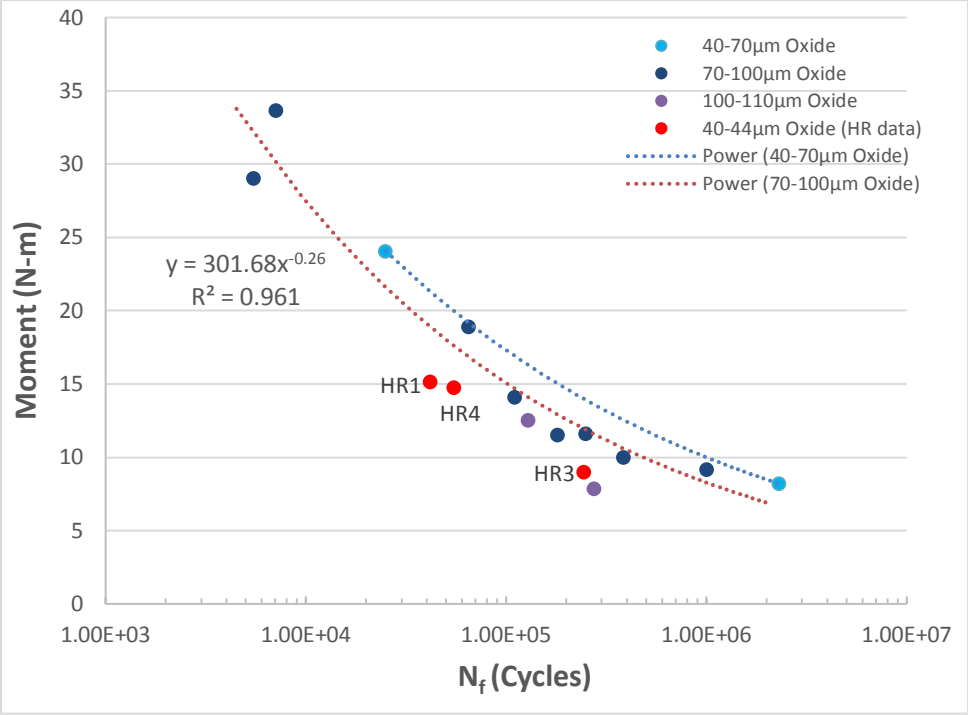

(a)

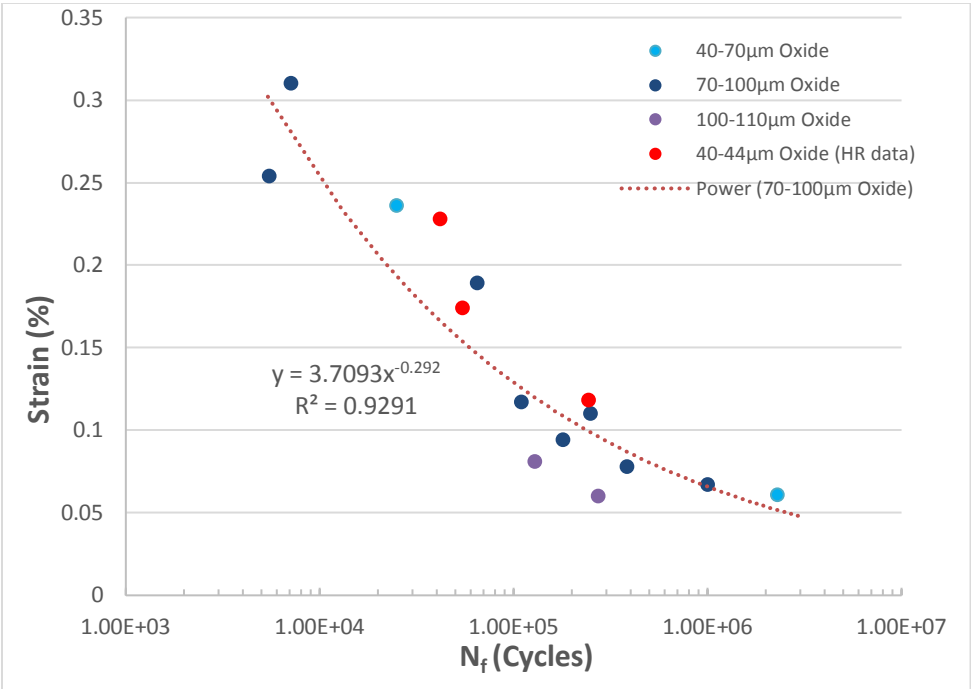

(b)

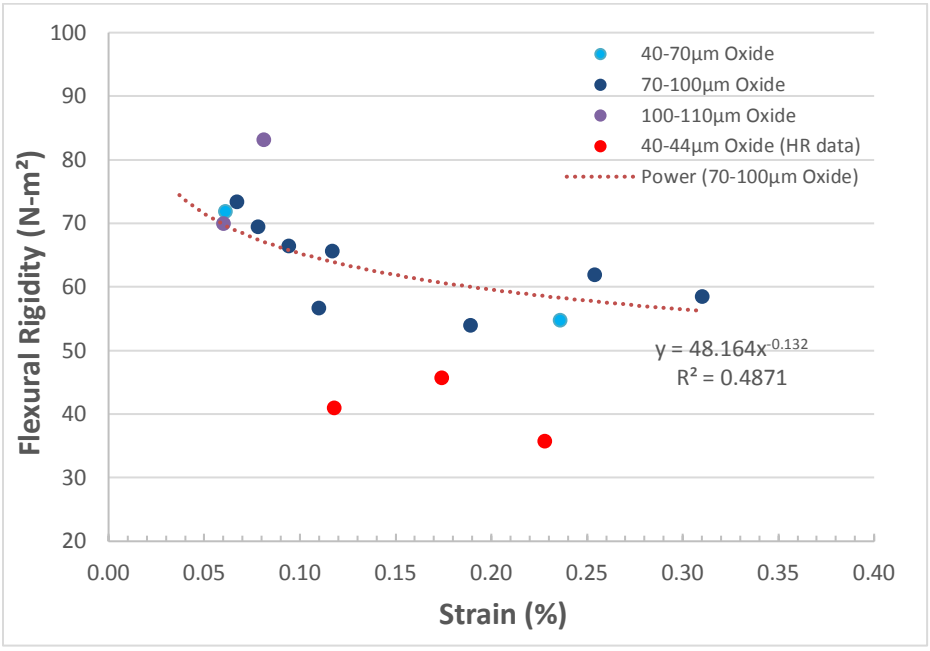

(c)

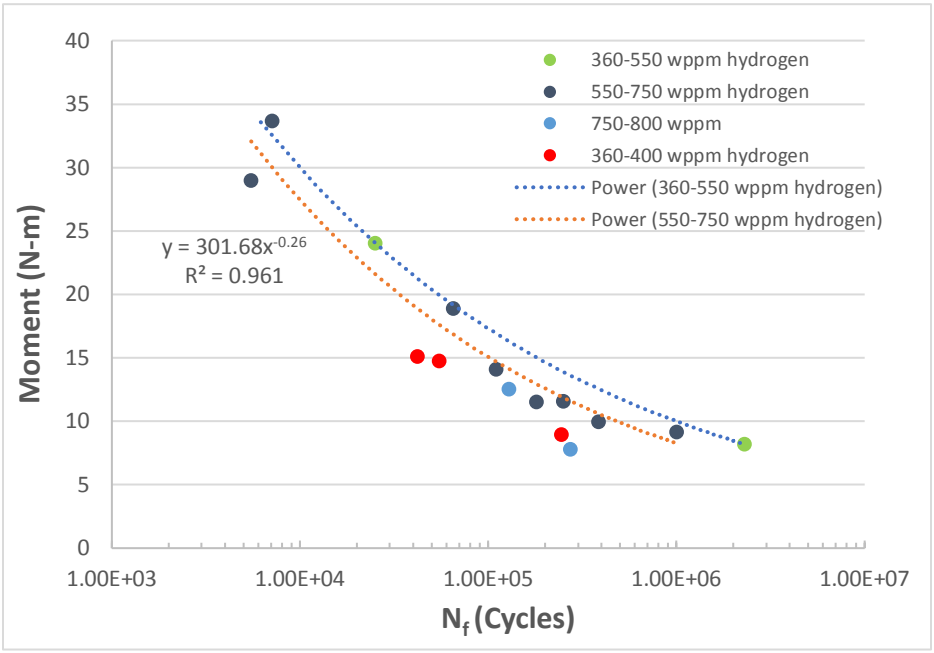

(d)

Figure 28. (a) Moment amplitude vs. number of failure cycles, (b) strain amplitude vs. number of failure cycles, (c) flexural rigidity vs. strain as function of clad oxide thickness, and (d) moment amplitude vs. number of failure cycles as function of hydrogen of span; flexural rigidity seems to be dependent on strain amplitude; HR4 has thermal heat treatment only without pressurization applied.

3.5.2 HR CIRFT Test Data Evaluation

Reoriented hydrides can change the SNF rod system's response. The procedure used to reorient the hydrides may result in other changes, including changes to pellet-cladding bonding efficiency or development of gaps at pellet-clad interface regions due to thermal treatment (400 °C) and clad tubing pressurization (140 MPa hoop stress) effect. The consequences of pellet-cladding interface bonding disruption [16] or increases in gap density at the interface are (1) reduction in the flexural rigidity and (2) increase in the contact load intensity of pellet-cladding mechanical interaction in HR samples. Table **10** shows that HR samples had low flexural rigidity compared to the as-irradiated samples. The reduced flexural rigidity resulted in an increase in clad strain amplitude of HR samples under similar loading amplitude compared to as-irradiated samples. Furthermore, significant reduction in flexural rigidity may indicate that the HR sample already evolved into a different composite system characteristic compared to the as-irradiated sample. Therefore, using the HR gauge strain amplitude vs. failure frequency trend to compare to that of as-irradiated samples can be misleading. The evidence of pellet-clad interface bonding disruption and gap formation in the HR rod system was further verified through PIE on HR1 sample, as shown in Figure 29; such gap formation was not observed in as-irradiated PIE.

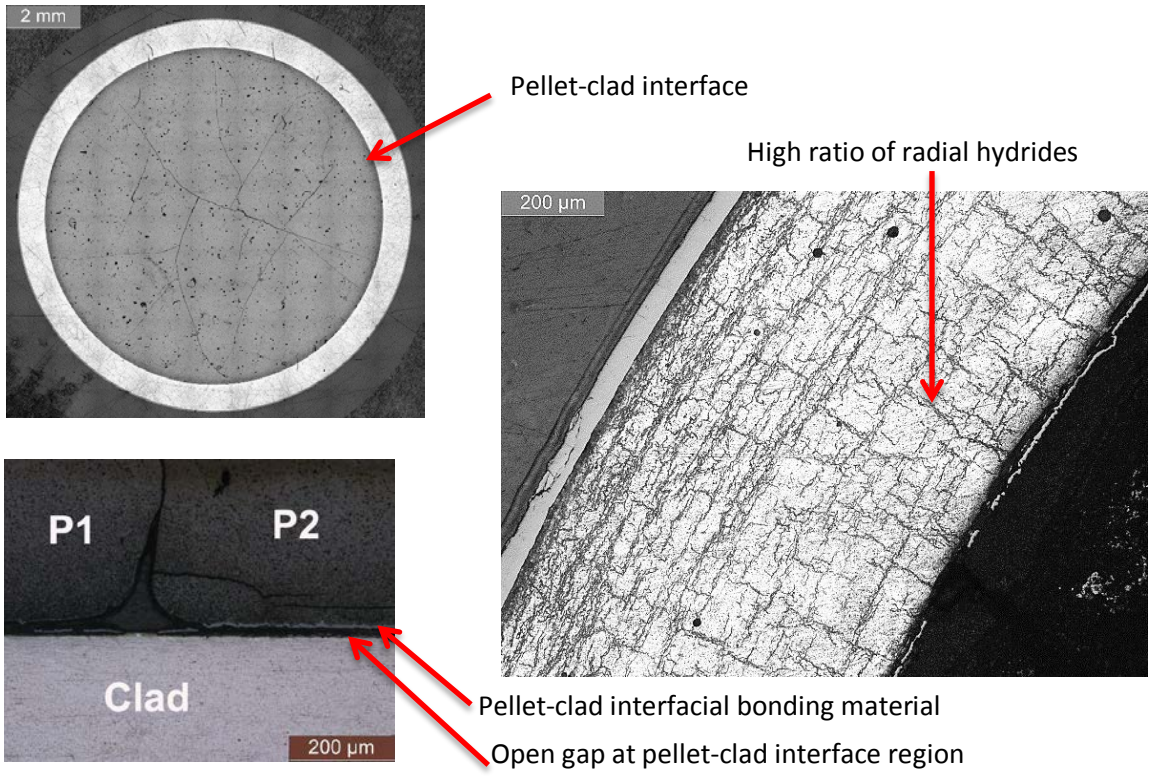

Figure 29. Metallographic examination of fuel and cladding: MET results of HR1 showing debonding phenomenon and gap formation at pellet-clad interface and high density of radial hydride formation in HR treated rod [23].

Furthermore, the HR1 sample showed significant radial hydride populations, but HR1 data only had a marginal reduction in fatigue life compared to HR4 data with thermal treatment only (see Figure 28). It is noted that HR1 and HR4 have similar oxide thicknesses as shown in Table 10. The 400 °C thermal treatment and pressurization adopted in preparing HR samples is not likely to introduce annealing recovery on the irradiated clad or to generate new flaws into the SNF system. Therefore, the flexural rigidity difference between HR1 and HR4 shown in Table 10 was primary due to the pressurization effect. The observations above may further indicate that the net effect of the radial hydride on fatigue life

reduction shown in Figure 28(a) is negligible. Furthermore, HR4 data also indicate that the adopted heat treatment of 400 °C alone had a negative effect on SNF system fatigue strength.

The rationale of the insignificant radial hydride effect on the SNF rod fatigue life is demonstrated below. The harmonic vibration load provided by CIRFT will generate the cyclic alternative principal tensile/compression stresses oriented in the rod's axial direction, which is in parallel to both radial and circumferential hydrides in the clad structure. Thus, it is expected that the effect of harmonic vibration loading applied on radial hydrides and circumferential hydrides would be very similar or no different from the principal tensile stress perspective. Therefore, HR data may support that the HR-induced radial hydride structure under the CIRFT harmonic vibration loading condition could not effectively trigger SNF clad crack initiation and growth failure mechanism.

It is noted that CIRFT data showed very limited or no flexural rigidity reduction upon the SNF rod's final fracture failure. The PIE data showed significant delamination near the clad hydride rim region, with no obvious beach marks or striations traced on the fractured surface that would typically show in the material's fatigue damage profile. A direct consequence of fatigue crack growth in the clad is the reduction of flexural rigidity. The HBU SNF failure phenomenon described herein indicates that no obvious crack growth occurred in SNF upon failure and that the SNF is in a brittle, sudden fracture failure mode. The key delamination driver is from the shear stress induced by material mismatch at the hydride and clad matrix interface under harmonic vibration loading. The major difference between the circumferential hydride and radial hydride effect under CIRFT loading is in the orientations of the resulting clad delamination profile: circumferential hydride induced delamination is in the circumferential direction, and radial hydride induced delamination is in the radial direction.

A recent study on the combined effect of harmonic vibration plus transient contact shock (simulated with a foot drop of CIRFT sample prior to CIRFT harmonic vibration loading) showed 75% fatigue life reduction compared to as-irradiated baseline data without the drop [24,25]. The detailed CIRFT real-time history monitoring data showed that the CIRFT test data with the drop event had a different damage mechanism compared to the as-irradiated baseline CIRFT test data. CIRFT drop impact data showed a significant decrease in flexural rigidity, indicating the fatigue crack growth in the SNF system. This was not observed from as-irradiated CIRFT data.

It is likely that transient contact shock can effectively trigger the crack initiation at the cladding's inner wall due to SNF rod contact impact induced maximum tensile stress or the so-called fuel cladding pinching effect. This type of failure mechanism was observed from a typical ring compression test or a rod pinch effect induced by the drop impact. This is in contrast to the axial principal tensile stress induced by the CIRFT harmonic vibration load, which will induce cracks or flaws initiated at the outer clad wall due to the maximum principal tensile stress located on the clad's outer surface.

However, due to less population in the hydride content and a lack of circumferential hydride rim reinforcement (existed near the cladding's outer surface wall of HBU SNF) in the inner wall region, the crack initiation and growth from the cladding's inner wall region would meet much less resistance compared to fatigue crack initiation and growth from the HBU SNF cladding's outer wall surface. Thus, the accelerated damage mechanism with significant reduction in fatigue life can be observed in a combined harmonic vibration loading and a contact transient shock loading mode [24,25]. With one drop from 12 inches (its contact load intensity is similar to 20 g), a 75% reduction in fatigue life was observed from CIRFT test results.

Radial hydride material demonstrated from ring compression test data that normally has low ductility and low fracture resistance for clad tubing structure [26]. This will further enhance crack initiation and crack growth in the cladding's inner wall region during the transient shock events under NCT. Therefore, when

an SNF rod has radial hydride population near the cladding's inner wall region, as shown in Figure 29, with the potential of repeated contact transient shocks, a significant reduction in fatigue life for an HR sample is expected compared to that of a baseline SNF sample. Figure 30 provides a comparison of a MOX SNF rod segment that was not impacted prior to the test (a) and a MOX SNF rod segment that received a 12-inch drop impact prior to the CIRFT test (b).

Regarding the HR effect, the potential HBU SNF accelerated aging effect of the combined harmonic vibration and transient shock loads due to SNF system contact interaction under normal conditions of SNF transport deserves special attention.

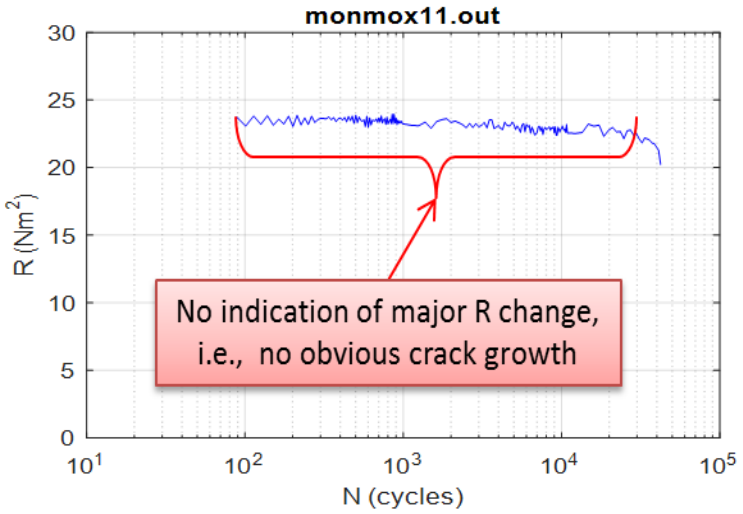

(a) CIRFT test without impact

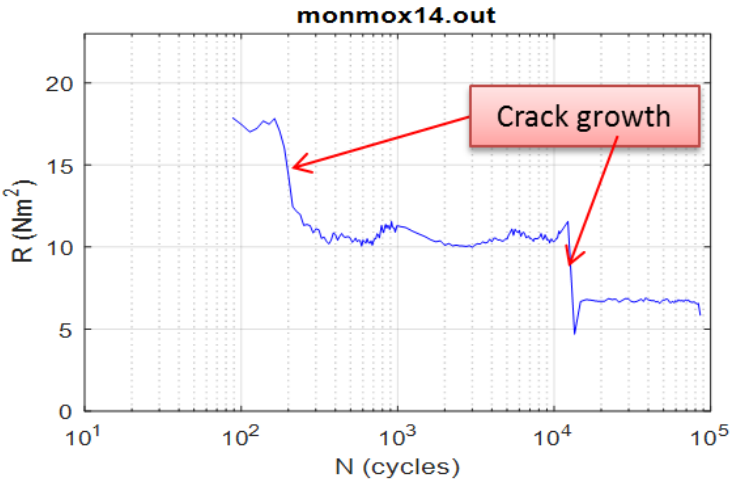

(b) CIRFT test with drop impact

Figure 30. HBU MOX rod real-time dynamic monitoring data of flexural rigidity (R) under CIRFT testing, (a) CIRFT test without drop showing no flexural rigidity reduction till failure, and (b) CIRFT test with prior 12-inch drop of CIRFT sample showing significant flexural rigidity reduction and indicating cladding crack initiation and growth in the 12-inch drop sample during CIRFT harmonic vibration testing [24].

3.6 Discussion

3.6.1 SNF Fatigue Life Comparison

The variations in fatigue life are given in Figure 31, including moment, equivalent stress, curvature, and equivalent strain for the tested SNFs. The following designations are used:

1) LMK—as-received
2) MOX_A—as-received
3) MOX_D—12 in. height drop treatment
4) MOX_H—heat treatment
5) HBR—as-received
6) HBR_HR—hydride reorientation treatment

The equivalent stress-strain collapsed the data points of all the SNFs into a single zone. A detailed examination revealed that at the same equivalent stress or strain level, fatigue lives display a descending order, as follows: LMK, HBR, and MOX.

The apparent knee point of endurance limit in the curve of moment and curvature or equivalent quantities is more clearly defined for LMK and HBR fuels.

The test results appear to indicate that impacts and RHT have a negative effect on fatigue life. The effect of heat treatment on MOX fuel rods was smaller at higher amplitudes, but it increased in intensity at lower amplitudes of moment. Thermal heat-treatment tended to extend the fatigue life of MOX fuel rod specimens. However, for HR4 testing, heat treatment had a negative effect on fatigue life compared to the HBR rod.

The heat treated MOX samples generally show a significant reduction in flexural rigidity compared to as-received MOX samples. Furthermore, some MOX fuel pellet disintegration into power form observed at the ends of sample rods under 400°C heat-treatment. The above observed phenomena are the root causes that can result in a significant reduction in the pellet-cladding interface bonding efficiency for the heat-treated MOX samples compared to that of as-received MOX samples. Thus, much less PCMI intensity from MOX_H sample is expected. This will result in a much less fatigue damage potential and longer fatigue life as indicated from MOX_H data.

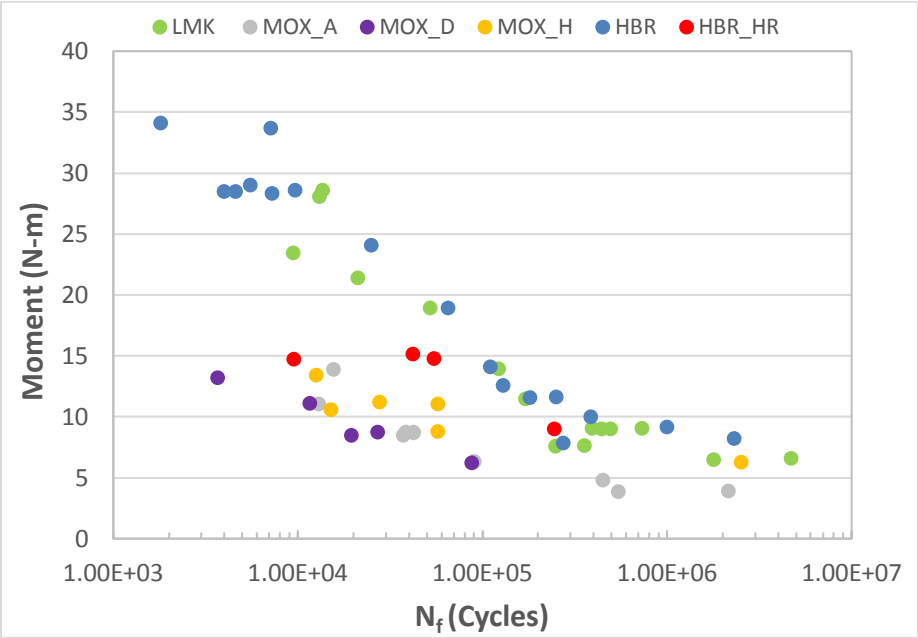
LMK
MOX_A
MOX_D
MOX_H
HBR
HBR_HR
Moment (N-m)
40
35
30
25
20
15
10
5
0
1.00E+03
1.00E+04
1.00E+05
1.00E+06
1.00E+07
Nf (Cycles)

(a)

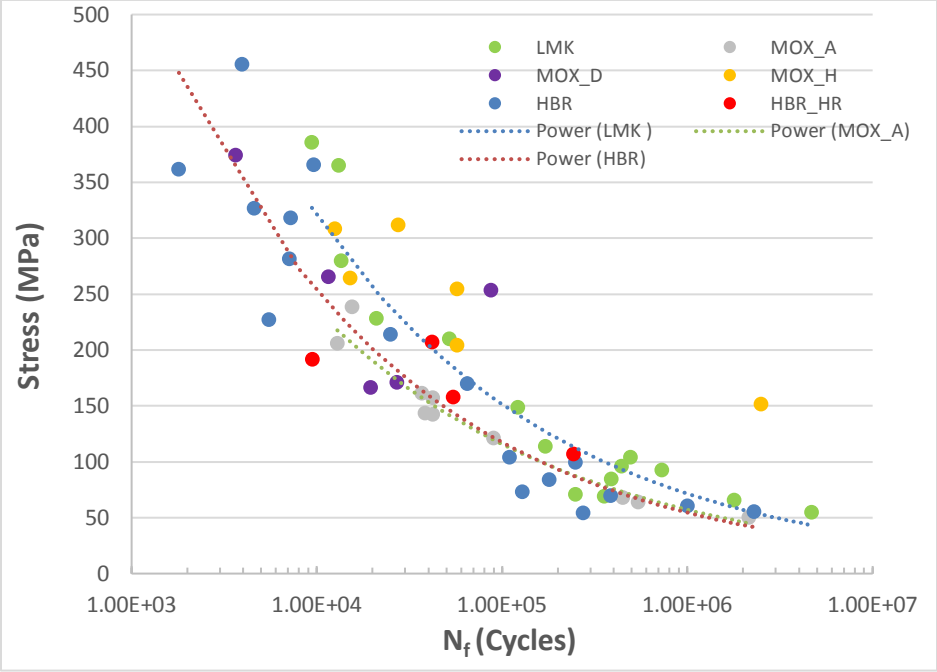
LMK
MOX_A
MOX_D
MOX_H
HBR
HBR_HR
Power (LMK)
Power (MOX_A)
Power (HBR)
Stress (MPa)
500
450
400
350
300
250
200
150
100
50
0
1.00E+03
1.00E+04
1.00E+05
1.00E+06
1.00E+07
Nf (Cycles)

(b)

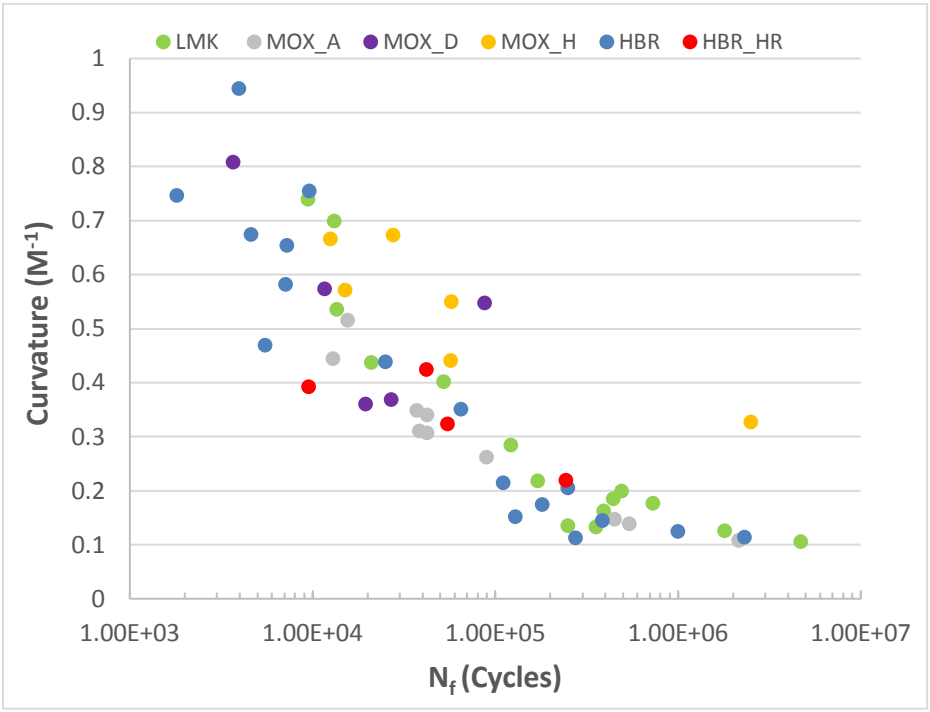

(c)

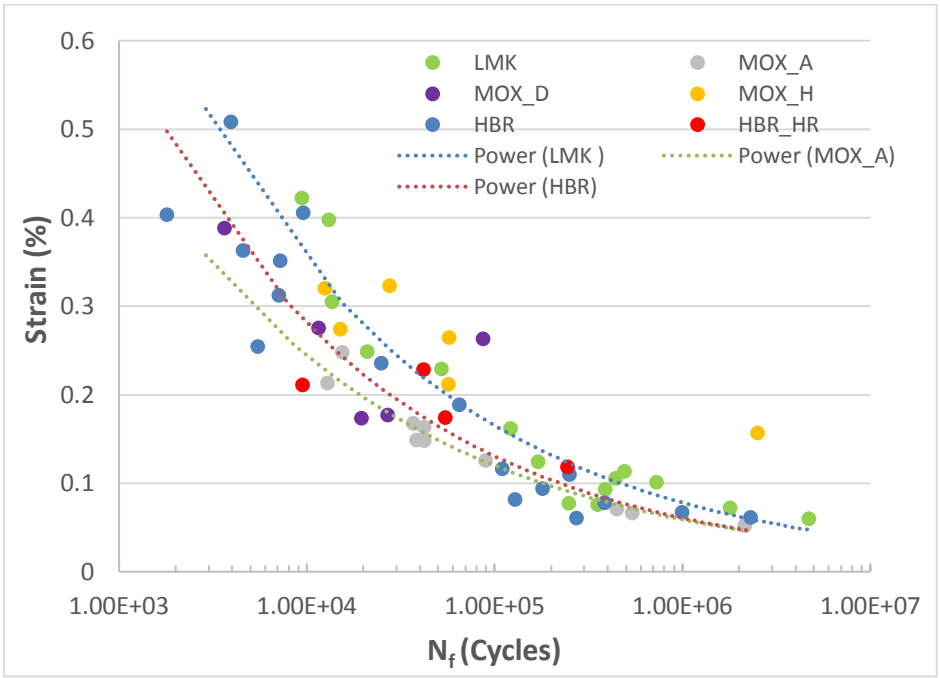

(d)

Figure 31. (a) Moment amplitude, (b) equivalent stress amplitude, (c) curvature amplitude, and (d) equivalent strain amplitude as a function of cycles to failure.

3.6.2 SNF Dynamic Deformation Simulation Assessments

In FY2016, a modal analysis was performed on the SNF assembly submodel in the frequency domainThe associated FEA model is illustrated in Figure 32 [24,25]. The results provide a better understanding of the frequency characteristics of the fuel assembly submodel. The fundamental mode of the submodel has a natural frequency of 2.44 Hz, which is also the dominant mode with the highest participation factor ratio.

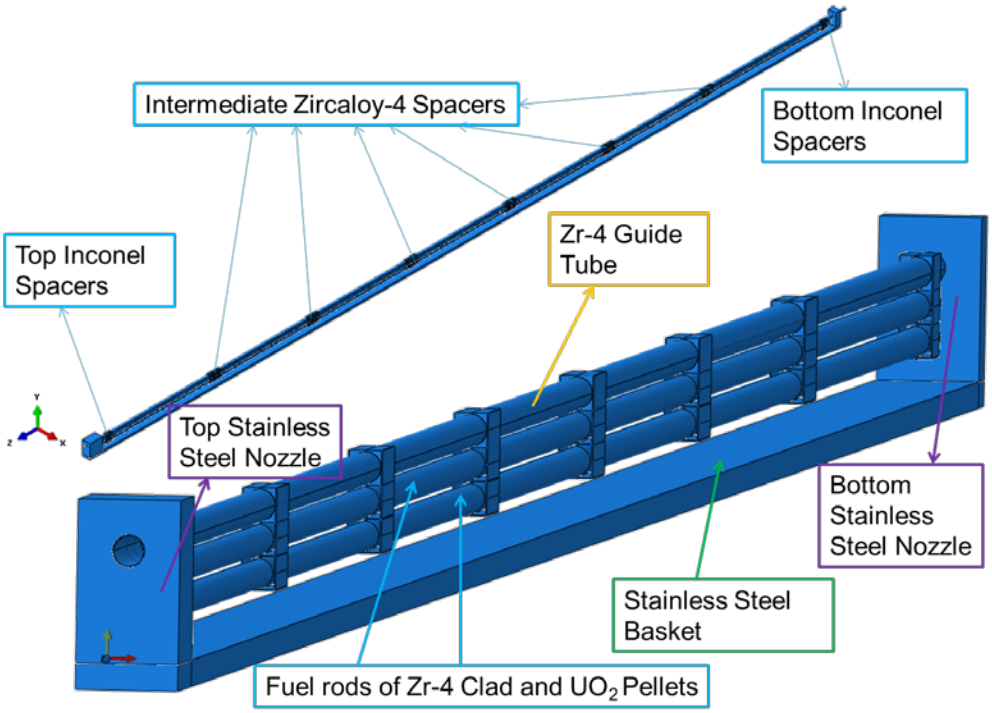

Figure 32. SNF assembly submodel for normal transportation evaluation.

In the time domain, the transient dynamic simulation consists of two stages: (1) an initialization stage to establish contact due to gravity, and (2) the second stage for transient dynamic loading. During the second stage, the acceleration as a sine waveform or impulse signal was used to represent normal transportation excitation or shock excitation for transient dynamic analysis. A 0.5 g sine wave acceleration excitation represents normal transportation vibration. The dynamic responses of the fuel assembly submodel show that the maximum stress occurs at the bottom Inconel spacer, where the material yields. The maximum stress in the guide tube also reached the yield strength. Yielding on the guide tube occurs at both top and bottom nozzle locations.

Results show that the guide tube and spacer grids are at the greatest risk of failure. Due to the horizontal orientation needed for transport, the guide tubes and spacer grids become the major gravity-bearing components supporting the dynamic loads of the fuel assembly. The integrity of the guide tube and spacer grids critically affects the vibration modes and the vibration intensity of fuel assembly during transport.

A 3 g impulse acceleration excitation represents transient shock during transportation. As in the dynamic response under 0.5 g sine wave acceleration excitation, yielding occurs at the bottom Inconel spacers [24,25]. The guide tube also yielded at the top and bottom nozzle locations during 3 g transient shock excitation. Thus, there were concerns for the integrity of the spacer grids and the guide tube under transient shock loading during NCT. The maximum stress level on the cladding was two times the level that it had been under 0.5 g sine wave acceleration excitation near yield strength. The basket, top, and bottom nozzles had reached yield strength.

To further evaluate the contact's interaction intensity between the fuel rod and the spacer grids induced by impact loading, a 3-D finite element section model of the detailed leaf spring/dimples was developed to simulate the impact between the fuel rod and the spacer grids as induced by the cask vibration during transport [24,25]. Under the assumed 20 g transient shock at the spacer grid region, the spring and dimples severely yielded, and the cladding yielded locally during the impact. The tensile yield points are on the inner surface of the cladding wall due to impact-induced tensile flexural stress there. The contact forces on the spring/dimples estimated from the FEA were high enough to cause significant plastic deformation. The bending moment estimated from the resultant stress on the cladding under 20 g transient shock can be used to define the loading in CIRFT vibration testing for the equivalent condition.

Furthermore, CIRFT test data from a 12-inch drop shows a different damage mechanism compared to harmonic vibration loads. These data show that the crack initiated from the inner cladding wall, where the highest tensile stress resided. This results in significant fatigue life reduction from CIRFT harmonic vibration tests. This observed phenomenon from CIRFT testing is consistent with that of the FEA simulation results [24,25].

3.6.3 The Impact of the SNF Skeleton Integrity to SNF Vibration Intensity

The fuel assembly skeleton, formed by guide tubes and spacer grids, is designed to constrain fuel rods in a reactor operation. In a horizontal set-up, shown in Figure 33, under SNF transport of NCT, the skeleton contains the primary load bearing members for carrying and transferring the bending vibration loads within SNF fuel assembly. The inertia-induced vibration load is carried by the skeleton throughout the SNF assembly, including contact interaction among SNF rods, spacer grids, and basket walls. Thus, the skeleton integrity can significantly affect the loading vibration intensity and frequency within an SNF system.

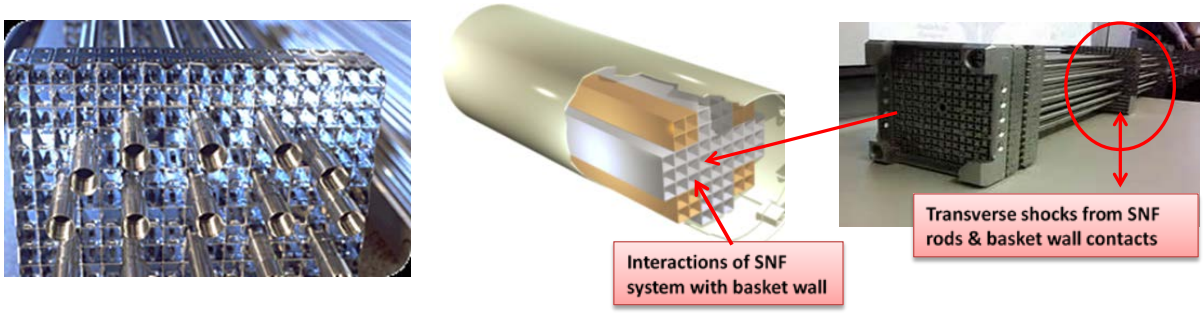

Figure 33. Typical fuel assembly skeleton at spacer grids region (left), and SNF system and canister basket walls interactions (right).

Dynamic interactions within the SNF assembly involving the skeleton, fuel rods, and canister basket wall can significantly increase impact loading intensity and frequency within the fuel assembly and the basket/canister structure. The aging or fatigued skeleton system can increase the impact loading intensity between fuel rods, and it can enhance the probability of large deformation resulting from SNF resonance vibration.

The contact interactions between the fuel rods and the basket wall can also increase the intensity and frequency of transient shock loads for the fuel rods. Proper structure reinforcement of canister design is warranted to overcome the static and dynamic vibration loads (external cask vibration and internal amplification from fuel assembly system vibration and its interaction transient shocks); mitigation includes increasing the cask system damping potential to reduce system vibration intensity.

4. Applying CIRFT Data for SNF System Vibration Reliability Study

There are four major components involved in an SNF system fatigue lifetime estimate: (1) SNF rod properties, (2) material history, (3) pellet-clad interaction, and (4) environmental loading conditions, as illustrated in Figure 34. The logistics of the typical fatigue life evaluation based on the S-N approach is illustrated in Figure 35.

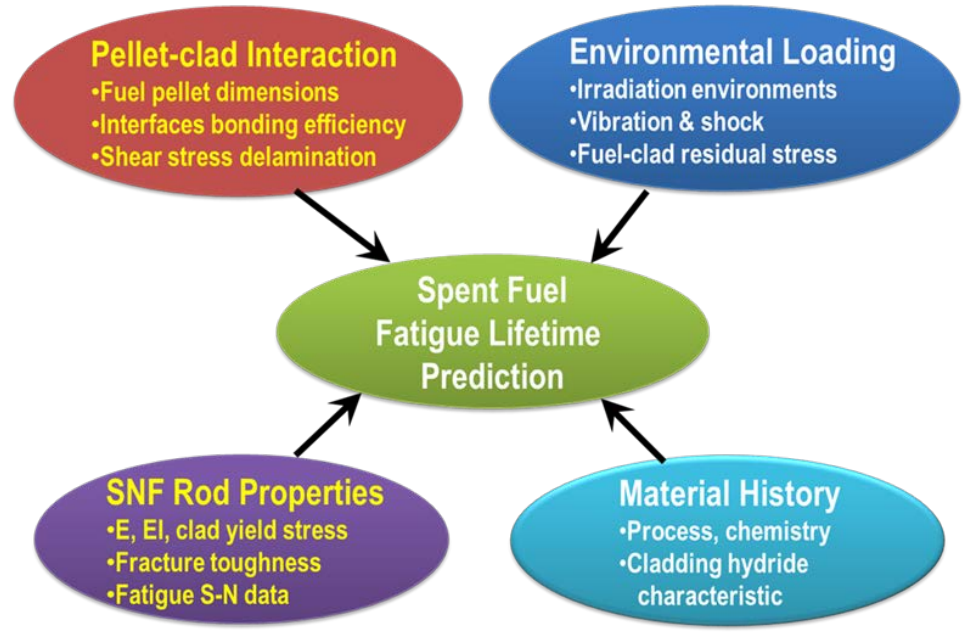

Figure 34. Components of SNF system fatigue life evaluation.

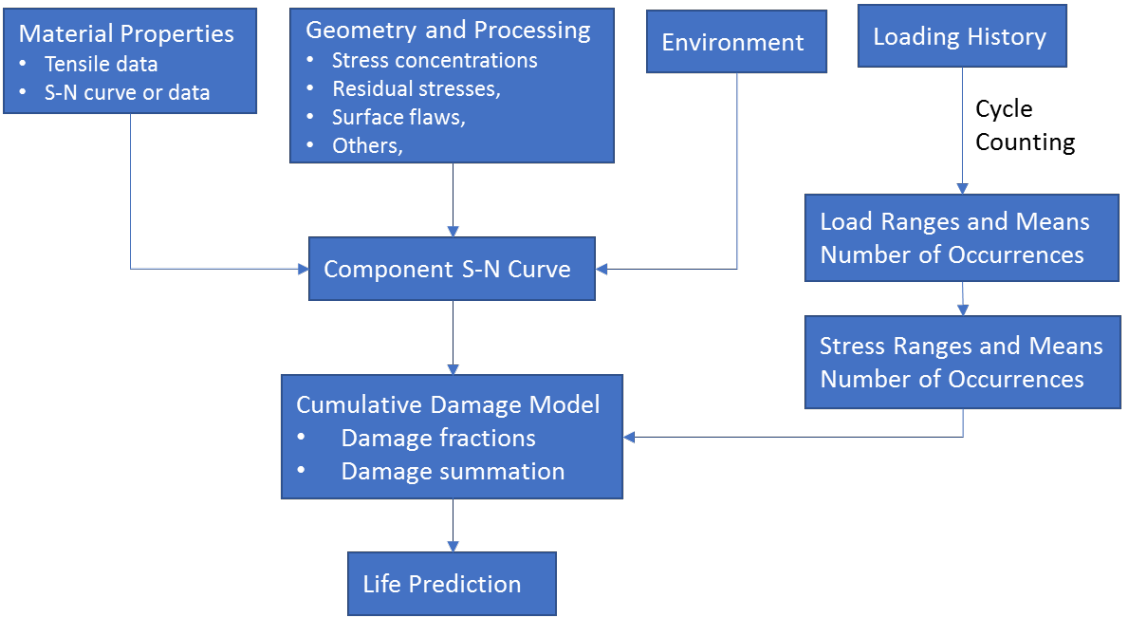

Figure 35. Typical fatigue life estimate procedures based on S-N approach.

4.1 Methodology Used for Evaluating SNF System Dynamic Stability

The three major initiatives in the DOE UFDC program developments for SNF transport reliability investigation are (1) SNF transport vehicle field vibration data collection, (2) SNF rods fatigue S-N trend development, and (3) SNF assembly dynamic response, as illustrated in Figure 36 and detailed in FCRD-UFD-2013-000325, "Used Nuclear Fuel Loading and Structural Performance Under Normal Conditions of Transport—Demonstration of Approach and Results of Used Fuel Performance Characterization." To make a realistic SNF system fatigue life prediction, the dynamic vibration intensity or deformation amplitude of the SNF system under NCT must be estimated. This can be done in two approaches: (1) using a vibrometer sensor to collect dynamic data directly on the SNF rod system insight a transport cask, i.e., vehicle field vibration data on the SNF rod level, or (2) using the fuel assembly dynamic response scheme of the FEA approach, with the cask's external vehicle vibration data as the input to estimate the vibration intensity and deformation amplitude at the SNF rod level. Due to a highly irradiated SNF assembly, the second option is more realistic and feasible, while the first option can also be applied in a vibration reliability investigation conducted outside the hot cell environment.

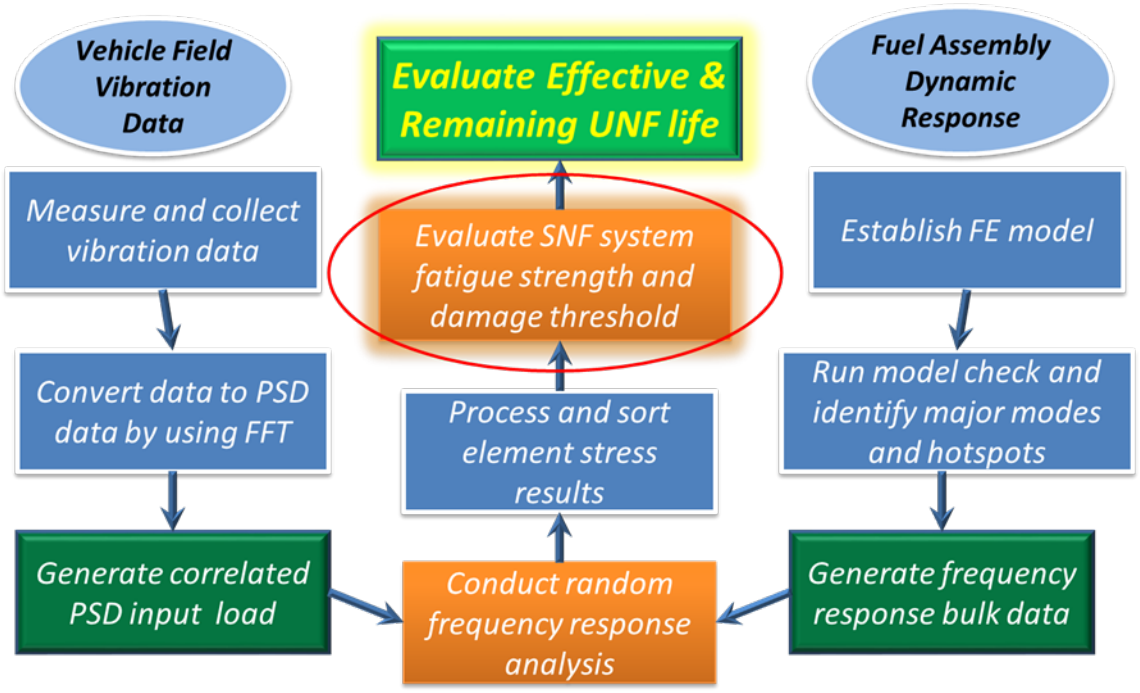

Figure 36. Core activities of DOE UFDC SNF transport vibration reliability investigation.

4.2 Using CIRFT S-N Data and SNF System Vibration Time-History Data to Determine SNF System AD

4.2.1 CIRFT Load Determination from Random Vibration Histogram

The typical random vibration history in the time domain can be transformed into the frequency domain using the Fast Fourier Series Transformation (FFT) scheme, as illustrated in Figure 37 for a vibration time-history available at the local fuel rod level. A more complex routine would be followed if only cask external vibration data are provided and if SNF system structural dynamic analyses are needed to develop localized SNF rod vibration spectrum, as illustrated in Figure 38.

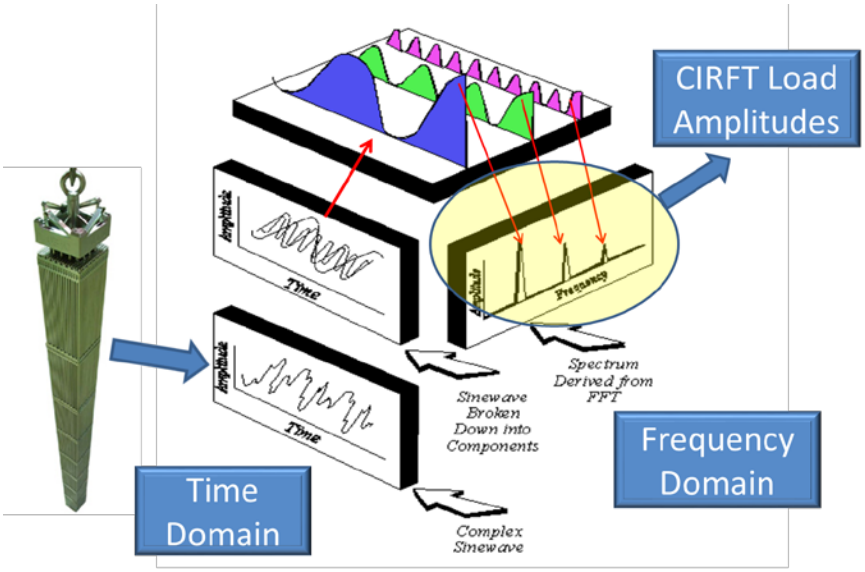

Figure 37. Vibration amplitude in frequency domain chosen for CIRFT testing.

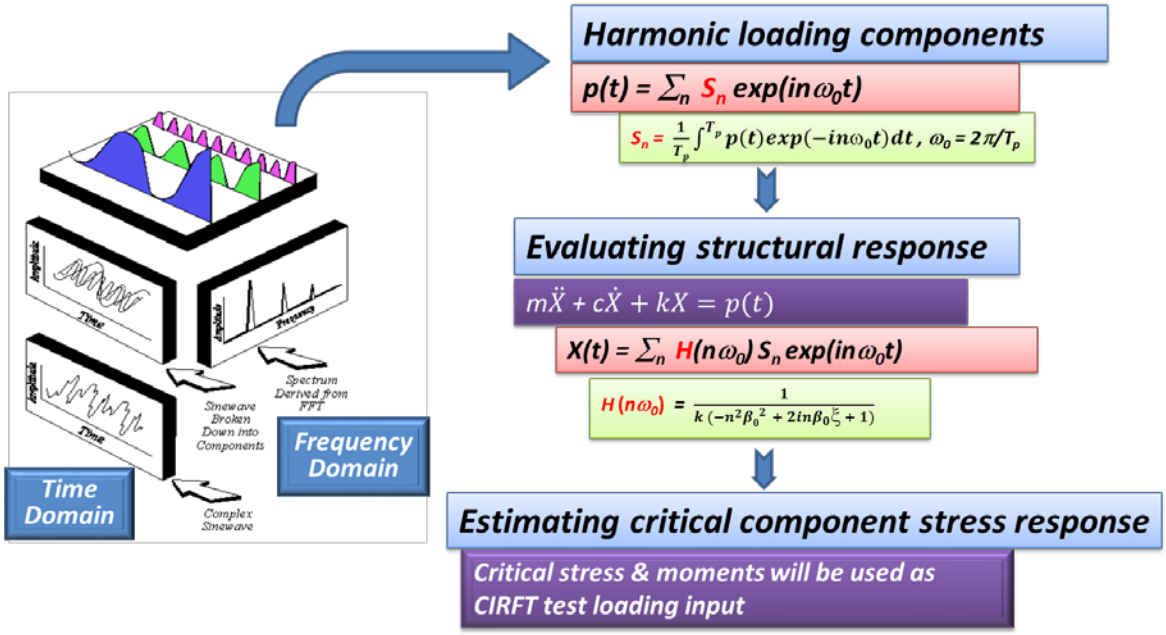

Figure 38. Estimating SNF system stress-strain based on cask external vibration data.

From FCRD-UFD-2013-000325 [27], the maximum cladding stress on the SNF system is estimated as 44.1 MPa, as shown Figure 39; and the corresponding equivalent bending moment for an HBU HBR rod is estimated at 8.4 N-m. A series of CIRFT testing was performed with the similar loading range, and the associated CIRFT testing results and the CIRFT specimens' details, including oxide thickness and specimen relative physical locations, are illustrated in Figure 40. The highest oxide thickness sample of an HBR rod located at the near top of SNF rod region has shortest fatigue life compared to the others.

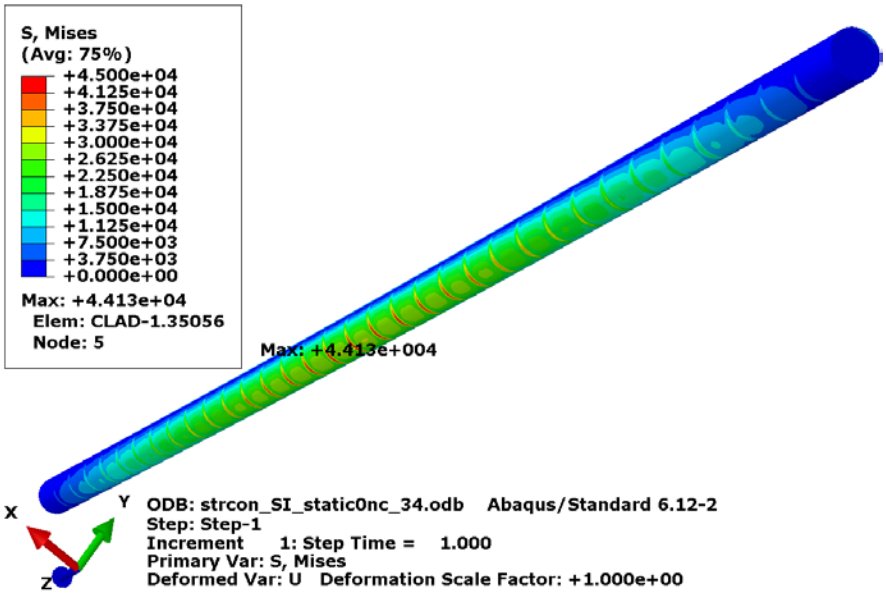

Figure 39. Full model stress results for the SNF rod under rail transport [26]; maximum stress of 44.1 MPa is equivalent to an 8.4 N-m bending loading on an HBU HBR rod under CIRFT testing.

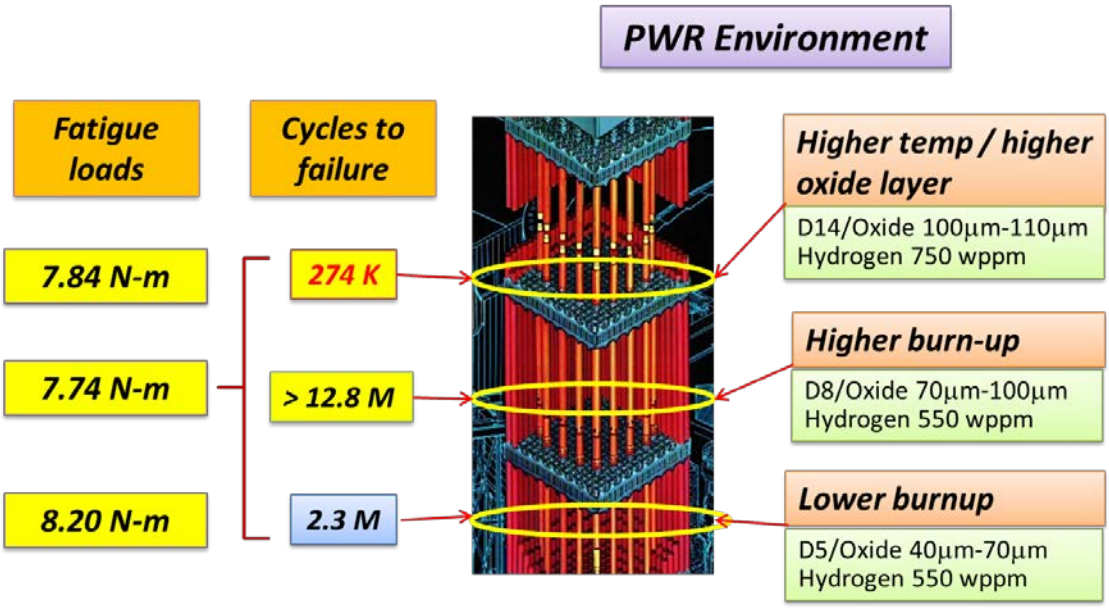

Figure 40. Weakest portion within an HBU HBR fuel assembly located at the upper region of SNF rod as indicated from CIRFT vibration test results.

4.2.2 SNF System Transport AD Evaluation

Before pursuing the AD evaluation, the major damage mechanisms of an HBU SNF assembly vibration must be understood. There are two types of loading modes involved in SNF transport under NCT: (1) harmonic vibration loading modes and (2) periodic transient shocks loading mode, including SNF system contact interactions. The associated damage mechanisms are described below.

1) Harmonic vibration loading mode:

- Crack growth is likely initiated at the outer clad wall under loading based on the maximum axial tensile stress that occurred on the outer cladding wall.
- No obvious crack growth was observed in the as-irradiated CIRFT test PIE data due to circumferential hydride rim reinforcement near the outer cladding wall.
- The HBU SNF failure under harmonic vibration appears to be due to a spontaneous brittle fracture.

2) Periodic transient shocks loading mode (including SNF system components contact interactions):

- The maximum axial/hoop tensile stress which occurred at the cladding's inner wall, the crack growth is likely initiated at the cladding's inner wall region and then propagates toward the cladding's outer wall under cyclic fatigue loading.
- The crack growth phenomenon was further confirmed based on the severe reduction in flexural rigidity observed from CIRFT real-time monitoring data.

The two failure damage mechanisms affecting SNF vibration stability under NCT are harmonic vibration mode and a transient shock mode. Apparently, the crack growth initiated at the cladding's inner wall has a higher damage potential. With one 12-inch drop (contact load intensity similar to that of a 20 g transient shock at the spacer grid region), fatigue life was reduced by 75% based on CIRFT test results. Due to the potential repeated contact transient shocks, the associated fatigue life reduction potential deserves special attention and should be included in an AD evaluation.

The effective damage index concept for evaluating SNF system fatigue life using the developed CIRFT testing protocol can be described as shown below:

$$\text{Effective Damage Index} = \Sigma_i \ \text{Weight(i)} \times \text{Harmonic vibration damage index(i)} + \Sigma_j \ \text{Transient shocks damage index (j)} \quad (22)$$

where the harmonic vibration damage index can be obtained from the harmonic vibration CIRFT test result with the associated weight function at the selected frequency and load amplitude (determined from SNF assembly vibration time-history data); and the weight function is the normalized contribution ratio among different harmonic vibration loading amplitudes obtained from FFT performed on a random vibration time-history spectrum in a frequency domain; and where the transient shock damage index can be obtained from an in-house developed combined transient shock impact, CIRFT test results at the target drop impact velocity or displacement, and the harmonic vibration loading intensity.

4.2.2.1 AD Evaluation

The AD evaluation scheme for SNF assembly transport under NCT is illustrated in Figure **41**; the associated governing equation derivation is described below.

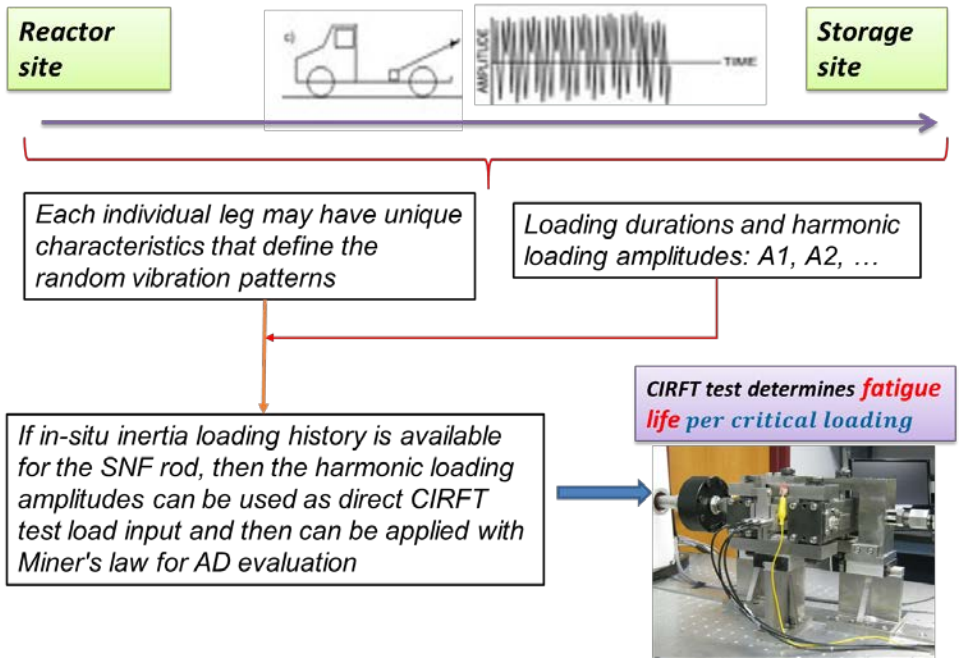

Figure 41. Methodology for evaluating AD of SNF system under NCT.

The harmonic vibration loading, $p(t) = \sum_n S_n \exp(in\omega_0 t)$, and the associated SNF assembly structure response, $X(t) = \sum_n H(n\omega_0) S_n \exp(in\omega_0 t)$, resulted from FFT and SNF assembly structural analyses shown in Figure 38, and will be used to assist in making the selections of CIRFT test loads for SNF assembly AD evaluation.

The SNF rod bending moment (M_n) associated with harmonic amplitude $\mathbf{H_nS_n}$ will be used as CIRFT test load input to estimate the associated fatigue failure cycles. Per each travel leg ***i*** as shown in

Figure 41, the associated AD_i can be written as shown below.

$$\mathbf{AD}_i = \frac{n1}{N(M1)} + \frac{n2}{N(M2)} + \frac{n3}{N(M3)} + \cdots \text{ (Miner's damage rule)} \qquad (23)$$

$N = N(M)$, where, N = cycles # to failure, M = harmonic vibration moment amplitude, $\mathbf{n_j}$ = harmonic vibration cycles at load amplitudes of M_j; and $\mathbf{n_j}$ is equal to $\mathbf{t_i}$ (travel time at leg i) × the associated loading amplitude frequency.

$$\mathbf{AD} = \Sigma_i \mathbf{AD_i}\,, \qquad (24)$$

and failure occurs when $\mathbf{AD = 1}$.

4.2.2.2 Effective Lifetime Evaluation per Specific Vibration Spectrum

If the probability density function $p(S)$ for stress amplitude S is available, then the AD can be written as.

$$\boldsymbol{AD = \int_0^n \frac{n(S)}{N(S)} dS = \frac{\omega T}{2\pi} \int_0^n \frac{p(S)}{N(S)} dS,} \quad (25)$$

where, $p(S) = \frac{S}{\sigma_S{}^2} \exp(\frac{-S^2}{2\sigma_S{}^2})$, σs^2 is variance of critical stress S(t), ***N(S)*** is the number cycles to failure, ***S*** is the harmonic stress amplitude, and ***n(S)*** is the number of cycles at harmonic stress amplitude ***S***.

Substitute $\boldsymbol{N(S) = \left(\frac{S1}{S}\right)^b N1}$ (obtained from CIRFT S-N trend curve) and ***p(s)*** into Eq. 24, then AD can be written as below,

$$\boldsymbol{AD = \frac{\omega T}{2\pi N1} \left(\frac{\sigma s}{S1}\right)^b 2^{b/2} \left(\frac{b}{2}\right)!} \quad (26)$$

By setting ***AD = 1***, the estimated SNF system failure life time, $\boldsymbol{T_{failure}}$, can be written as

$$\boldsymbol{T_{failure} = \frac{2\pi N}{\omega} 1 \left(\frac{S_1}{\sigma_S}\right)^b \frac{2^{b/2}}{(b/2)!}} \quad (27)$$

5. CONCLUSIONS

The CIRFT approach demonstrates the controllable fatigue fracture on HBU SNF in a normal vibration mode, which allows for examination of the underlying mechanism of the SNF system's dynamic performance. General observations from CIRFT evaluations include the following:

- The fuel pellet provided strength (flexural rigidity) to the fuel/cladding system and also introduced cladding stress concentrations at PPIs.
- When the fuel is fatigued to failure, the failure occurs or initiates primarily at the PPI.
- Pellet and clad dimensions/properties and their interface bounding efficiency can affect SNF fatigue characteristic and flexural strength.
- The SNF rod system has significant stress concentrations and residual stress inherited from reactor operation.
- In dynamic CIRFT evaluations, fuel pellets retain their shapes (dishing and chamfering is evident) and do not become fragmented—very little residue was released from rods upon fracture.
- Considering the complexity and nonuniformity of the HBU fuel cladding system, it was significant to find that the strain or equivalent stress-to-failure data for the SNF was characterized by a curve that would be expected in standard uniform materials.
- It was significant to find that the HBU HBR exhibited an endurance limit, if an endurance limit is defined by survival of $>10^7$ cycles.
- High oxide thickness and high hydrogen concentration did affect SNF system strength and showed significant reduction in SNF rod fatigue life.
- SNF failures depend on loading intensity and loading rates; fuel assembly contact interactions induced by transient shocks under NCT can significantly reduce SNF fatigue lifetime.
- In addition to the fatigue strength data, the SNF system's fracture toughness data are also essential for the SNF vibration reliability study, especially in a high-rate of transient shocks loading of NCT.

The more specific findings from this report are stated below.

5.1 CIRFT Data Trends

The lessons learned from studying CIRFT test data and the curvature adjustment are detailed below.

- The curvature measurement data from a CIRFT test were updated with LVDTs probe spacing adjustments and LVDTs stem dynamic stability correction factor. This resulted in a reduction of over 50% in curvature measurements compared to measurements using unadjusted curvature data.
- The equivalent stress and strain collapsed all CIRFT data points from all HBU SNFs into a single zone. At the same stress or strain level, a detailed examination based on the mean trend curves of the corresponding subgroups revealed that fatigue lives display a descending order as follows: LMK, HBR, and MOX.
- The apparent knee point in the curve of moment and curvature or equivalent quantities is more clearly defined for LMK and HBR fuels.
- Both the 12-inch drop and the RHT appear to negatively impact the fatigue life of CIRFT specimens.

- The effect of the thermal heating treatment on a MOX fuel rod was relatively small at the higher loading amplitude, and it became more significant at the low lading amplitude. Thermal heating treatment extends the fatigue life of MOX specimens; this is primary due to a significant reduction in pellet-cladding bonding efficiency as discussed earlier. However, HR4 CIRFT testing of the heat treated HBR rod showed that heat treatments have a negative impact on the fatigue life of the HBR rod. This may indicate that the effect of heat treatment on SNF rods is likely to be dependent on the material and the SNF fuel-cladding system geometry.
- The development of the MESA enables proper translation of the global CIRFT test results of moment-curvature data into a local cladding stress-strain profile.

5.2 Damage Mechanisms involved in SNF Vibration under NCT

Based on CIRFT testing results from harmonic vibration loading and prior harmonic vibration load, the test specimen underwent a 12-inch drop, and two damage mechanisms were identified, as detailed below.

- Due to maximum axial tensile stress which occurred on the cladding outer wall under harmonic vibration loads, the crack that formed was likely initiated at the cladding's outer wall. However, due to significant clad matrix reinforcement from the circumferential hydride rim near the cladding's outer wall, the PIE of CIRFT tested samples only showed complex delaminate layers of the cladding without clear indication of the fatigue crack growth profile. This indicates that the hydride rim in-turn became the crack propagation barrier in the radial direction, eventually forcing the crack propagation orientation along the hydride axial and circumferential orientations.
- Due to maximum axial and hoop tensile stress which occurred on the cladding's inner wall under transient shock loads, the crack was likely initiated at the cladding's inner wall region and then propagated toward the cladding's outer wall. Thus, the primary reason that the flexural rigidity vs. the number of cycles showed several abrupt drops of flexural rigidity was due to the crack growth from the cladding's inner wall.
- There are two failure damage mechanisms observed from a harmonic vibration mode and a transient shock mode (induced by fuel assembly contact interaction; in this case a Sandia truck test of 20 g acceleration data was used for the demonstration). Apparently, the crack propagation from cladding's inner wall has a much higher efficiency due to less resistance from the hydride composite in the cladding's inner wall region once the radial crack was initiated.
- As the result of a12-inch drop (load intensity is equivalent to a 20 g transient shock at the spacer grid region), fatigue life was observed to be reduced by 75%.
- Due to the potential repeated contact transient shocks, the potential for reduced associated fatigue life should be investigated further.

REFERENCES

1. Wang, J.-A. J, H. Wang, T. Cox, and Y. Yan (2012). *Progress Letter Report on U-Frame Test Setup and Bending Fatigue Test for Vibration Integrity Study (Out-of-Cell Fatigue Testing Development–Task 2.3)*. Oak Ridge, TN: Oak Ridge National Laboratory. Report No. ORNL/TM-2012/417.
2. Wang, J.-A. J, H. Wang, and T. Tan, inventors; Oak Ridge National Laboratory, assignee. Reversal Bending Fatigue Testing (2014). United States patent US 8,863,585 B2. Oct. 21, 2014.
3. Wang, H., J.-A. J. Wang, T. Tan, H. Jiang, T. S. Cox, R. L. Howard, B. B. Bevard, and M. E. Flanagan. (2013) "Development of U-frame Bending System for Studying the Vibration Integrity of Spent Nuclear Fuel," *Journal of Nuclear Materials*, 440, 201–13.
4. Wang, J.-A. J., H. Wang, T. Cox, and C. Baldwin (2013). *Progress Letter Report on Bending Fatigue Test System Development for Spent Nuclear Fuel Vibration Integrity Study (Out-of-Cell Fatigue Testing Development–Task 2.4).* Oak Ridge, TN: Oak Ridge National Laboratory. Report No. ORNL/TM-2013/225.
5. Wang, J.-A. J., H. Wang, B. B. Bevard, R. L. Howard, and M. E. Flanagan (2013). "Reversible Bending Fatigue Test System for Investigating Vibration Integrity of Spent Nuclear Fuel During Transportation." Paper presented at the International Symposium on the Packaging and Transportation of Radioactive Materials, San Francisco, CA, August 18–23.
6. Wang, J.-A. J. and H. Wang. (2014). *The Development of Reversible Bending Fatigue Tester and Its Application to High Burn-up Spent Nuclear Fuel Integrity Study under Normal Transportation Vibration*. Oak Ridge, TN: Oak Ridge National Laboratory. Report No. ORNL/TM-2013/573. http://info.ornl.gov/sites/publications/Files/Pub47469.pdf.
7. Wang, J.-A. J. and H. Wang (2014). *Semi-Annual Progress Letter Report on Used Nuclear Fuel Integrity Study in Transportation Environments*. Report No. ORNL/TM-2014/63. http://info.ornl.gov/sites/publications/Files/Pub48652.pdf.
8. Wang, J.-A. J., H. Wang, and H. Jiang (2014). *FY14 Status Report: CIRFT Testing Results on High Burnup UNF*. Oak Ridge, TN: Oak Ridge National Laboratory. Report No. ORNL/LTR-2014/310. http://info.ornl.gov/sites/publications/Files/Pub51054.pdf.
9. Wang, J.-A. J. and H. Wang (2015). *Mechanical Fatigue Testing of High-Burnup Fuel for Transportation Applications.* Oak Ridge, TN: Oak Ridge National Laboratory. Report Nos. ORNL/TM-2014/214 and NUREG/CR-7198.
10. Wang, J.-A. J., H. Wang, H. Jiang, Y. Yan, and B. B. Bevard (2015). *CIRFT Testing of High-Burnup Used Nuclear Fuel Rods from Pressurized Water Reactor and Boiling Water Reactor Environments*. Oak Ridge, TN: Oak Ridge National Laboratory. Report Nos. ORNL/SPR-2015/313 and M2-FCRD-UFD-2015-000101.
11. Wang, J.-A. J., H. Wang, Y. Yan, R. Howard, and B. B. Bevard (2011). *High Burn-up Spent Fuel Vibration Integrity Study Progress Letter Report (Out-of-Cell Fatigue Testing Development–Task 2.1)*. Oak Ridge, TN: Oak Ridge National Laboratory. Report No. ORNL/TM-2010/288.
12. Wang, J.-A. J., H. Wang, T. Tan, H. Jiang, T. Cox, and Y. Yan (2012). *Progress Letter Report on U Frame Test Setup and Bending Fatigue Test for Vibration Integrity Study (Out-of-Cell Fatigue Testing Development–Task 2.2).* Oak Ridge, TN: Oak Ridge National Laboratory. Report No. ORNL/TM-2011/531.
13. Wang, J.-A. J., H. Wang, and T. Tan (2011). *An Innovative Dynamic Reversal Bending Fatigue Testing System for Evaluating Spent Nuclear Fuel Rod Vibration Integrity or Other Materials Fatigue Aging Performance*. Oak Ridge, TN: Oak Ridge National Laboratory. ORNL Invention Disclosure No. 201102593. DOE Report No. DOE S 124,149.
14. Wang, J.-A. J., H. Wang, B. B. Bevard, R. L. Howard, and M. E. Flanagan (2013). "SNF Test System for Bending Stiffness and Vibration Integrity" *International High-Level Radioactive Waste Management Conference*, Albuquerque, NM, April 28–May 2, 2013.

15. Wang, J.-A. J., H. Wang, T. Cox, and C. Baldwin (2013). *Progress Letter Report on Bending Fatigue Test System Development for Spent Nuclear Fuel Vibration Integrity Study (Out-of-Cell Fatigue Testing Development–Task 2.4).* Oak Ridge, TN: Oak Ridge National Laboratory. Report No. ORNL/TM-2013/225.
16. Jiang, H., J.-A. Wang, and H Wang (2016). "The Impact of Interface Bonding Efficiency on High-Burnup Spent Nuclear Fuel Vibration Integrity," Journal of Nuclear Engineering and Design, 309 40–52.
17. Ruzauskas, E. J. and K. N. Fardell(2001). *Design, Operation, and Performance Data for High Burnup PWR Fuel from H. B. Robinson Plant for Use in the NRC Experimental Program at Argonne National Laboratory*, Electric Power Research Institute, EPRI Report 1001558.
18. Wang, J.-A. and H. Jiang (2014). *Quantification of CIRFT System Biases and Uncertainties When Testing High-Burnup Spent Nuclear Fuel*, ORNL/TM-2014/288, DOE FCRFD-2014-000604.
19. Wang, J.-A., H. Jiang, and H. Wang (2014). *Using Finite Model Analysis and Out of Hot Cell Surrogate Rod Testing to Analyze High Burnup Used Nuclear Fuel Mechanical Properties*, ORNL/TM-2014/257, DOE FCRD-UFD-2014-000603.
20. Daum, R.S., S. Majundar, and M. C. Billone (2008). "Experimental and analytical investigation of the mechanical behavior of high-burnup Zircaloy-4 fuel cladding," *J. ASTM International*, 5, Paper ID JAI101209.
21. Geelhood, K. J. et al. (2008). *PNNL Stress/Strain Correlation for Zircaloy*, PNNL-17700, Pacific Northwest National Laboratory, Richland, Washington, July 2008.
22. Morris, R.N., C. A. Baldwin, R. Battiste, J. M. Giaquinto, I. C. Gauld, J. G. Hemrick, K. J. Leonard, H. F. Longmire, W. J. McAfee, J. K. McCoy, J. Myers, S. L. Voit, J.-A. Wang, and Y. Yan (2013). *MOX PIE Fuel and Clad Examination Final Report*, ORNL/MD/LTR-352 Rev 2.
23. Wang, J.-A., Wang, H., Yan, Y., "ORNL Interim Progress Report on Hydride Reorientation CIRFT Tests," ORNL/TM-2016/660, October 2016.
24. Wang, J.-A. et al. *FY 2016 Status Report: Documentation of All CIRFT Data including Hydride Reorientation Tests.* ORNL/SR-2016/424, DOE M2FT-16OR080202031, Oak Ridge, TN: Oak Ridge National Laboratory, September 2016.
25. Jiang, H. and J.-A. Wang (2016). "Spent Nuclear Fuel System Dynamic Stability under Normal Conditions of Transport," *Journal of Nuclear Engineering and Design*, 310, 1–14.
26. Billone, M., T. A. Burtseva, M.A. Martin-Rengel, Effects of Lower Drying-Storage Temperatures on the DBTT of High Burnup PWR Cladding, ANL-15/21, FCRD-UFD-2015-000008, Argon National laboratory, August 2015.
27. Adkins, H. E. et al., *Used Nuclear Fuel Loading and Structural Performance Under Normal Conditions of Transport—Demonstration of Approach and Results of Used Fuel Performance Characterization*, FCRD-UFD-2013-000325, DOE UFDC Program, September 30, 2013.

This page intentionally left blank.